Kinetic Energy Spectra, Backscatter, and Subgrid Parameterization Analysis in Radiative-Convective Equilibrium

by

Kwan Tsaan Lai

A thesis
presented to the University of Waterloo
in fulfillment of the
thesis requirement for the degree of
Doctor of Philosophy
in
Applied Mathematics

Waterloo, Ontario, Canada, 2025

© Kwan Tsaan Lai 2025

Examining Committee Membership

The following served on the Examining Committee for this thesis. The decision of the Examining Committee is by majority vote.

External Examiner: Daniel Kirshbaum
Associate Professor
Dept. of Atmospheric and Oceanic Sciences
McGill University

Supervisor: Michael L. Waite
Professor
Dept. of Applied Mathematics
University of Waterloo

Internal Member: Marek Stastna
Professor
Dept. of Applied Mathematics
University of Waterloo

Francis J. Poulin
Professor
Dept. of Applied Mathematics
University of Waterloo

Internal-External Member: Christopher G. Fletcher
Associate Professor
Dept. of Geography and Environmental Management
University of Waterloo

Author's Declaration

This thesis consists of material all of which I authored or co-authored: see Statement of Contributions included in the thesis. This is a true copy of the thesis, including any required final revisions, as accepted by my examiners.

I understand that my thesis may be made electronically available to the public.

Statement of Contributions

Chapter 2 consists of a paper published for publication in the Journal of the Atmospheric Sciences. This paper presents research work that I have performed in my PhD program. Chapters 3 and 4 are written as manuscripts that will be submitted for publication. The published paper is co-authored by my supervisor, Michael L. Waite, who played a normal supervisory role in the research and made some editing work on the manuscript text.

Abstract

This thesis explores how energy is distributed and transferred across scales in convective-permitting radiative-convective equilibrium (RCE) simulations and how these processes can be more accurately represented in numerical models through improved subgrid parameterizations. Aggregation steepens the horizontal kinetic energy spectra by enhancing the large-scale energy, which results in horizontal kinetic energy spectra in both the upper troposphere and lower stratosphere that are close to the mesoscale -5/3 spectrum. In the upper troposphere, spectral energy budget analysis indicates that this is the result of the balance between buoyancy flux and vertical energy flux, rather than a classic direct energy cascade. In the lower stratosphere, there is inverse energy transfer, which may be explained by wave-mean-flow-interaction. Subfilter energy transfer analysis is performed on an idealized RCE simulation by filtering 1-km high-resolution simulation to a horizontal scale of 4 km. The net subfilter energy transfer rate is dissipative in the upper troposphere and backscattering in the lower stratosphere, which are consistent with the direction of energy transfer in the nonlinear transfer energy flux. The stochastic backscatter TKE scheme, a stochastic backscatter-allowing subgrid turbulence scheme created by adding a zero-mean stochastic forcing to the eddy viscosity of the TKE scheme, is proposed and tested on idealized RCE simulations. The stochastic backscatter TKE scheme improves the subgrid local energy transfer when compared to a common stochastic backscatter scheme and the standard TKE scheme without backscatter. Despite the fact that backscatter is still weaker than dissipation in the lower stratosphere in the stochastic backscatter TKE simulations, the kinetic energy spectra are closer to the -5/3 spectrum when compared to the standard TKE simulation. This study advances our understanding of the interscale distribution and transfer of energy in RCE, and the introduction of the stochastic backscatter TKE scheme provides a more realistic representation of dissipation and backscatter by matching the distribution of subfilter energy transfer rate from a high-resolution simulation.

Acknowledgements

"The struggle of man against power is the struggle of memory against forgetting."

– Milan Kundera, *The Book of Laughter and Forgetting*

I would like to thank my supervisor, Dr. Michael L. Waite. I am lucky to have you as my supervisor. For anyone who is reading this acknowledgement now, you can not imagine how many struggles I had throughout my time. The toughest time was the summer of 2019. I felt extremely lost and desperate during that time. Thank you for being there for me. Just listening to you talk about your experience, daily life, family, and what Waterloo was like in the past helped me a lot emotionally at that time.

I am always grateful to be a member of the fluid group and the applied math department. I am not a very outgoing person. Thank you for accepting me as a family. In the future, I will certainly miss the days when I could just randomly drop by the lab and hear about some spicy takes that Dr. Marek Stastna have on things. I was lucky to be a student of Dr. Sivabal Sivaloganathan, Dr. Kevin Lamb, Dr. Francis Poulin, Dr. Joe West, Dr. Sean Speziale, and Dr. Conrad Hewitt. Thank you for the love, guidance and support. I would like to thank my external examiner, Dr. Daniel Kirshbaum. I would also like to take this opportunity to thank again Dr. Francis Poulin, Dr. Marek Stastna and Dr. Christopher Fletcher for serving on my examining committee. I appreciate all the valuable feedback, and they have improved this thesis to a great extent.

The CMOS in Halifax is one of my most unforgettable memories, and it is in large part because of Laura Chandler and David Deepwell. I am glad to share an office with Owen Wang, Nathan Braniff. Thank you Owen for bringing me into the Linux world. It is my pleasure to be friends with Dinesh Siewnarine, Amir Atoufi, Mohammad Mohammadifar, William Sepahi and Nico Castro-Folker—special thanks to all of you. Just one quick message, and I can get the immediate help that I need. I can't imagine how much trouble I would get into without the help. Thank you to my neighbours Karl and Tea's family. Thank you for inviting me over for dinner when you know that I am not eating healthily without my wife.

My childhood dream was to become a scientist. Thank you to my family for their unconditional support of my decision to make my dream come true.

This thesis was made possible by the facilities of the Shared Hierarchical Academic Research Computing Network (SHARCNET:www.sharcnet.ca) and Digital Research Alliance of Canada (https://alliancecan.ca/en).

Dedication

This is dedicated to everyone who has helped and supported me.

Table of Contents

Examining Committee ii

Author's Declaration iii

Statement of Contributions iv

Abstract v

Acknowledgements vi

Dedication vii

List of Figures xii

List of Tables xix

1 Introduction 1

1.1 Overview 1

1.2 Governing Equations 2

1.2.1 The Continuity Equation 2

1.2.2 The Momentum Equations 3

1.2.3 Energy Equation for Dry Air 3

1.2.4 Anelastic Approximation 4

1.3 What is Radiative-Convective Equilibrium? . . . 6
1.3.1 Moist Static Energy Budget . . . 6
1.4 Turbulence and Energy Cascade . . . 8
1.4.1 Kolmogorov's 1941 Theory . . . 9
1.4.2 Kinetic Energy Spectrum in the Atmosphere . . . 10
1.5 LES and the TKE Subgrid Turbulence Scheme . . . 11
1.6 Weather Research and Forecasting Model . . . 13
1.7 Eliassen-Palm Flux-Like Analysis . . . 15
1.8 Thesis Objectives . . . 16
1.8.1 Kinetic Energy Spectrum and the Spectral Energy Budget Analysis in RCE . . . 17
1.8.2 Subfilter Energy Transfer Rate Analysis . . . 17
1.8.3 Proposed Backscatter-Allowing Stochastic Subgrid Turbulence Mixing Scheme . . . 18

2 Kinetic Energy Spectra and Spectral Budget of Radiative-Convective Equilibrium 19

2.1 Introduction . . . 20
2.1.1 RCE and Self-Aggregation . . . 20
2.1.2 Energy Spectrum . . . 23
2.1.3 Energy Spectral Budget . . . 24
2.2 Methodology . . . 26
2.2.1 Model . . . 26
2.2.2 Kinetic Energy Spectrum and Spectral Budget . . . 27
2.3 Results and Discussion . . . 32
2.3.1 Overview of the Simulations . . . 32
2.3.2 Kinetic Energy Spectra and Budget . . . 34
2.3.3 Nonlinear Spectral Energy Flux . . . 42
2.3.4 Compensated Kinetic Energy Spectra . . . 48

2.3.5 Rotation . . . 48
2.4 Conclusions . . . 51
2.5 Acknowledgments . . . 54
2.6 Appendix: Modified Equation . . . 54

3 Backscatter in Radiative-Convective Equilibrium 56
3.1 Introduction . . . 56
3.2 Methodology . . . 58
3.2.1 Model . . . 58
3.2.2 Diagnostics . . . 60
3.3 Results and Discussion . . . 62
3.3.1 Overview of the Simulations . . . 62
3.3.2 Subfilter Energy Transfer Rate . . . 65
3.3.3 Components of Subfilter Energy Transfer Rate . . . 72
3.3.4 Effect of Filters . . . 78
3.3.5 Spectral Energy Budget . . . 82
3.4 Conclusions . . . 85

4 A Backscatter-Allowing Stochastic Subgrid Turbulence Scheme 88
4.1 Introduction . . . 88
4.2 Methodology . . . 90
4.2.1 Stochastic Differential Equation - Wiener Process . . . 90
4.2.2 Stochastic Differential Equation - Ornstein–Uhlenbeck Process . . . 91
4.2.3 Technical Details for SKEBS . . . 92
4.2.4 Stochastic Backscatter TKE scheme . . . 95
4.2.5 Model . . . 96
4.2.6 Diagnostics . . . 97
4.3 Result . . . 98

4.3.1 Overview 98
4.3.2 Subgrid Energy Transfer and Subfilter Energy Transfer at 4 km Scale 110
4.3.3 Distribution of Local Energy Transfer 115
4.3.4 Spectral Energy Budget 119
4.4 Conclusions 126

5 Conclusion and Future Work **128**
5.1 Concluding Remarks 128
5.2 Future Work 130

References **132**

List of Figures

1.1 Observed zonal and meridional wind atmospheric kinetic energy spectra (Nastrom and Gage, 1985) © American Meteorological Society. Used with permission. 10

2.1 The outgoing longwave radiation (W/m^2) at top of the atmosphere (TOA OLR) for the non-aggregated simulation at t = (a) 160 hours, (b) 320 hours, (c) 480 hours, (d) 640 hours, (e) 800 hours, (f) 1120 hours, (g) 1440 hours, and (h) 1760 hours, and for the aggregated simulation at t = (i) 160 hours, (j) 320 hours, (k) 480 hours, (l) 640 hours, (m) 800 hours, (n) 1120 hours, (o) 1440 hours, and (p) 1760 hours. 35

2.2 Vertical profiles of (a) water vapor mixing ratio, (b) cloud water plus cloud ice mixing ratio, and (c) temperature at t = 160 hours (black), 320 hours (blue), 480 hours (green), 640 hours (red), 800 hours (orange), 1120 hours (purple), 1440 hours (light pink), and 1760 hours (dark pink), and (d) the time series of the variance of vertically-integrated frozen moist static energy (FMSE) for the non-aggregated simulation. The variance of vertically-integrated FMSE is smoothed with a 24-hour moving average. 36

2.3 As in Fig. 2.2, but for the aggregated simulation. 37

2.4 The horizontal kinetic energy spectrum (blue), rotational kinetic energy spectrum (yellow), and divergent kinetic energy spectrum (purple) in the upper troposphere (6-10 km) for (a) the non-aggregated simulation and (b) the aggregated simulation; and the spectral budget, including horizontal nonlinear energy transfer (blue), buoyancy flux (yellow), vertical energy flux divergence (red), dissipation from the subgrid mixing scheme (purple), and numerical dissipation (green), in the upper troposphere for (c) the non-aggregated simulation and (d) aggregated simulation. All spectra are averaged in the vertical and in time from 841 to 1848 hours. Budget spectra are multiplied by k_h, for all k_h except for $k_h = 0$, to preserve area on semi-log plots. Note that $k_h = 0$ is shown in Figs. c-d. 40

2.5 As in Fig. 2.4, but in the lower stratosphere (15.5-17 km). 42

2.6 The rate of change of kinetic energy spectrum (dE/dt) is compared to the sum of the budget for the non-aggregated simulation (a) in the upper troposphere and (b) in the lower stratosphere, and for the aggregated simulation (c) in the upper troposphere and (d) in the lower stratosphere. The error is the ratio between the absolute value of the difference between the sum of the budget and dE/dt and the maximum of the absolute value of all the terms in the budget. 43

2.7 The nonlinear transfer spectral energy flux $\Pi(k, z)$ ($\mathrm{m^2 s^{-3} kg m^{-3}}$), which is averaged in time from 841 hours to 1848 hours, from height 6 km to 17 km for non-aggregated simulation. 46

2.8 As in Fig. 2.7, but for the aggregated simulation. 47

2.9 The compensated kinetic energy spectrum for the non-aggregated simulation (a) in the upper troposphere and (b) in the lower stratosphere, and for the aggregated simulation (c) in the upper troposphere and (d) in the lower stratosphere. All spectra are averaged in the vertical and in time from 841 to 1848 hours 49

2.10 The horizontal kinetic energy spectrum (blue), rotational kinetic energy spectrum (purple), and divergent kinetic energy spectrum (green) for (a) the upper troposphere (6-10 km) of the rotation simulation and (b) the lower stratosphere (15.5-17 km) of the rotation simulation; and the spectral budget, including horizontal nonlinear energy transfer (blue), buoyancy flux (yellow), vertical flux divergence (red), dissipation from the subgrid mixing scheme (purple), and numerical dissipation (green), in the upper troposphere for (c) the upper troposphere (6-10 km) of the rotation simulation and (d) the lower stratosphere (15.5-17 km) of the rotation simulation. All spectra are averaged in the vertical and in time from 841 to 1008 hours. Budget spectra are multiplied by k_h, for all k_h except for $k_h = 0$, to preserve area on semi-log plots. Note that $k_h = 0$ is shown in Figs. c-d. 52

3.1 The time series of the domain-averaged variance of TOA OLR (blue) and the negative of the domain-mean TOA OLR (red). The negative is added to the domain-mean TOA OLR to show that the variance of the TOA OLR aligns with the negative of the domain-mean TOA OLR. A 6-hour moving average is used to improve readability. 62

3.2 The outgoing longwave radiation (W/m^2) at the top of the atmosphere (TOA OLR) from hours 59 to 94 to show the typical evolution of a non-aggregated simulation in RCE. Note that the presented plots show the full 600 km (x) $\times$ 600 km (y) domain. 63

3.3 Time series of domain total subfilter energy transfer rate $\iiint_V P dx_1 dx_2 dx_3$ with box-filter (Box) (a) in the upper troposphere and (b) in the lower stratosphere. A 6-hour moving average is used to improve the readability. Backscatter (BS) is the integral of the positive value ($\iiint_V P_+ dx_1 dx_2 dx_3$) of the subfilter energy transfer rate to represent the energy added to the resolved flow, dissipation (Diss) is the negative value ($\iiint_V P_- dx_1 dx_2 dx_3$) of the subfilter energy transfer rate to represent the energy removed from the resolved flow, and the net dissipation $\iiint_V P_+ dx_1 dx_2 dx_3$ is the sum of dissipation and backscatter. The dissipation given by the eddy viscosity from the 4-km non-aggregated simulation is also included for comparison. 66

3.4 Time series of vertically-averaged dissipation (Diss) and backscatter (BS) with box-filter in region with high OLR (OLR$< 215K$) and low OLR (OLR$\leq 215K$) in the upper troposphere. A 6-hour moving average is used to improve the readability. 68

3.5 As in Fig. 3.4, but in the lower stratosphere. 69

3.6 Normalized histogram of the subfilter energy transfer rate in the upper troposphere (blue) and the lower stratosphere (orange). The normalized histograms are computed with 5000 bins over -10^5 to 10^5 Js^{-1}. 99.76 % and 99.91% of points are between -10^5 to 10^5 Js^{-1} in the upper troposphere and lower stratosphere, respectively. A zoom-in plot is also provided in the top right corner of each plot. The average subfilter energy transfer rates in the upper troposphere and lower stratosphere are represented with the green and light blue vertical lines in the zoom-in plot, respectively. 71

3.7 Time series of the integral of the components of subfilter energy transfer rate (P_{ij}) = (a) P_{11}, (b) P_{12}, (c) P_{13}, (d) P_{22}, (e) P_{23}, (f) P_{33} in the upper troposphere. A 6-hour moving average is used to improve readability. . . . 73

3.8 As in Fig. 3.7, but in the lower stratosphere. 74

3.9 The vertically-averaged subfilter energy transfer rate with the box filter at 77 hours in the upper troposphere. The subfilter energy transfer rate P (panel g) is decomposed into component P_{ij} = (a) P_{11}, (b) P_{12}, (c) P_{13}, (d) P_{22}, (e) P_{23}, (f) P_{33}. The zoom-in plot of the total subfilter energy transfer rate (g) uses the point with the highest absolute value of subfilter transfer rate as the center to give a closer look (300 km $\times$ 300 km) to the total subfilter energy transfer rate. The TOA OLR (h) uses the same colourmap as Fig.3.2. Other than the zoom-in plot (Fig. g), all other plots show the full 600 km (x) $\times$ 600 km (y) domain. 75

3.10 As in Fig. 3.9, but in the lower stratosphere. 76

3.11 As in Fig. 3.3, but with the box filter (Box), Gaussian filter (Gaus), the spectral cutoff filter (cutoff) in the (a) upper troposphere and (b) lower stratosphere. Note that the dissipation from the 4-km non-aggregated simulation is not included in this figure. 79

3.12 As in Fig. 3.6, but with the box filter (Box), Gaussian filter (Gaus), the spectral cutoff filter (cutoff) in (a) the upper troposphere and (b) the lower stratosphere. The average subfilter energy transfer rate of the box filter, the Gaussian filter and the spectral cutoff filter are represented with the red, light blue and purple vertical lines in the zoom-in plot, respectively. When the spectral cutoff filter is used, 99.86 % and 99.69% of points are between -10^5 to 10^5 Js^{-1} in the upper troposphere and lower stratosphere, respectively. 80

3.13 The horizontal kinetic energy spectra (a) in the upper troposphere (6-10 km) and (b) in the lower stratosphere (15.5-17 km). The horizontal kinetic energy spectra (blue) can be decomposed into rotational kinetic energy spectrum (yellow) and divergent kinetic energy spectrum (purple). The spectral energy budget (c) in the upper troposphere (6-10 km) and (d) in the lower stratosphere (15.5-17 km). The spectral budget is composed of the horizontal nonlinear energy transfer (blue), buoyancy flux (yellow), vertical energy flux divergence (red) and dissipation (not shown). All the spectra are averaged in time over the full 14-day simulation and in the vertical. 83

3.14 The nonlinear transfer spectral energy flux $\Pi(k)$ ($m^2s^{-3}kgm^{-3}$) for (a) the upper troposphere and (b) lower stratosphere, which are averaged in time over the full 14 days of the simulation and in the vertical. 84

4.1 The time series of the negative of the domain-mean outgoing longwave radiation (W/m^2) at the top of the atmosphere (TOA OLR) for the a1tau50 (blue), a1tau500 (orange), a1pt5tau50 (green), a2tau50 (red), SKEBS (purple), standard (brown), $dx = 1$ km (pink) simulation. A 6-hour moving average is used to improve the readability. 99

4.2 The time series of the negative of the domain-mean TOA OLR for the standard and the $dx = 1$ km simulations when compared with the (a) a1tau50, (b) a1tau500, (c) a1pt5tau50, (d) a2tau50, and (e) SKEBS simulations. A 6-hour moving average is used to improve the readability. 100

4.3 The TOA OLR (W/m^2) 12 hours before and 12 hours after the most aggregated state for the a1tau50 simulation. The full 600 km (x) $\times$ 600 km (y) domain is shown. 101

4.4 As in Fig. 4.3, but for the a1tau500 simulation. 102

4.5 As in Fig. 4.3, but for the a1pt5tau50 simulation. 103

4.6 As in Fig. 4.3, but for the a2tau50 simulation. 104

4.7 As in Fig. 4.3, but for the standard simulation. 105

4.8 As in Fig. 4.3, but for the SKEBS simulation. 106

4.9 As in Fig. 4.3, but for the $dx = 1$ km simulation. 107

4.10 Time series of domain total net dissipation $-\iiint_V P_K dx_1 dx_2 dx_3/(5.0 \times 10^7 J/s)$ for the a1tau50 (blue), a1tau500 (orange), a1pt5tau50 (green), a2tau50 (red), SKEBS (purple), standard (brown) simulations and the subfilter energy transfer rate -$\iiint_V P dx_1 dx_2 dx_3/(5.0 \times 10^7 J/s)$ for $dx = 1$ km simulation with box-filter (pink) and cutoff filter. Positive values of net dissipation are dissipation, and negative values of net dissipation are backscatter. 109

4.11 As in Fig. 4.10, but in the lower stratosphere. 110

4.12 Time series of domain total dissipation (orange) and backscatter (blue) (5.0×10^7 J/s) for the (a) a1tau50, (b) a1tau500, (c) a1pt5tau50, (d) a2tau50, (e) SKEBS, (f) standard, and (g) $dx = 1$ km simulation with the box-filter and the cutoff filter in the upper troposphere. A 6-hour moving average is used to improve the readability. The net subgrid (subfilter) energy transfer rate ($\iiint_V P dx_1 dx_2 dx_3/(5.0 \times 10^7 J/s)$) are the sum of backscatter ($\iiint_V P_+ dx_1 dx_2 dx_3/(5.0\times10^7 J/s)$) and dissipation ($\iiint_V P_- dx_1 dx_2 dx_3/(5.0\times 10^7 J/s)$), where $P = P_+ + P_-$ following (3.2.2) and (3.2.2). 111

4.13 As in Fig. 4.12, but in the lower stratosphere. 112

4.14 Probability density function (pdf) of the subfilter energy transfer rate per volume for $dx = 1$ km box (orange) and $dx = 1$ km cutoff (green) compared to the subgrid energy transfer rate per volume (blue) for (a) a1tau50, (b) a1tau500, (c) a1pt5tau50, (d) a2tau50, (e) SKEBS, and (f) standard simulation in the upper troposphere. The pdf are computed with 200 bins over -0.4 to 0.4 $\mathrm{Js^{-1}m^{-3}}$ except for the SKEBS simulation. The pdf for SKEBS is computed with 200 bins over -0.003 to 0.003 $\mathrm{Js^{-1}m^{-3}}$. Positive and negative values of subgrid (subfilter) transfer rate represent backscatter and dissipation, respectively. 116

4.15 As in Fig. 4.14, but in the lower stratosphere 117

4.16 The horizontal kinetic energy spectrum can be decomposed into rotational kinetic energy spectra and divergent kinetic energy spectrum. This figure shows the (a) horizontal kinetic energy spectra, (b) rotational kinetic energy spectra and (c) divergent kinetic energy spectra for the a1tau50 (blue), a1tau500 (red), a1pt5tau50 (yellow), a2tau50 (purple), SKEBS (green) and standard (light blue) simulations in the upper troposphere. The -5/3 spectrum is given by the dark red line. 120

4.17 The spectral kinetic energy budget is composed of the horizontal nonlinear energy transfer, buoyancy flux, vertical energy flux divergence and dissipation. This figure shows the (a) horizontal nonlinear energy transfer, (b) vertical energy flux divergence, (c) buoyancy flux and (d) dissipation which stochastic subgrid forcings for the a1tau50 (blue), a1tau500 (red), a1pt5tau50 (yellow), a2tau50 (purple), SKEBS (green) and standard (light blue) simulations in the upper troposphere. All spectra are averaged in time over the full 14-day simulation and in the vertical. 121

4.18 As in Fig. 4.16, but in the lower stratosphere. 122

4.19 As in Fig. 4.17, but in the lower stratosphere. 123

List of Tables

2.1 The Eliassen-Palm flux contribution ($m^2 s^{-3} kg m^{-3}$), mean flow contribution ($m^2 s^{-3} kg m^{-3}$), transfer at $k_h = 0$ ($m^2 s^{-3} kg m^{-3}$), and vertical flux from the advection at $k_h = 0$ ($m^2 s^{-3} kg m^{-3}$) for (a) the upper troposphere (UT) and (b) the lower stratosphere (LS). 46

3.1 The correlation between the time series of the subfilter energy transfer with the box filter and the time series of mean OLR and variance of OLR in the upper troposphere (UT) and the lower stratosphere (LS) 67

4.1 The list of all simulations for this chapter. The four stochastic backscatter simulations and the SKEBS are modified and initialized from the non-aggregated simulation from Chapter 2. The parameters for stochastic backscatter TKE scheme are referring to a and τ from 4.30. The SKEBS simulation uses the default parameter values from WRF. The standard simulation is the non-aggregated simulation from Chapter 2 continued over the same time period as the other simulations in this chapter. The $dx = 1$ km simulation is the simulation presented in Chapter 3 also continued over the same time period as the other simulations in this chapter. 97

1

Introduction

1.1 Overview

The origin of the mesoscale -5/3 spectrum and the effect of subgrid energy transfer are two unsolved problems in atmospheric modelling research. Understanding the mechanisms responsible for the mesoscale -5/3 spectrum and the effect of subgrid energy transfer can help us to more accurately understand and model the atmosphere. In this thesis, the kinetic energy spectra and subgrid energy transfers of convective systems are investigated in radiative-convective equilibrium (RCE). RCE is an idealized climate system. RCE is a simple idealized model for research because it is only driven by sensible and latent heat fluxes at the surface and balanced by the radiative cooling of the atmosphere (e.g. Nolan et al., 2007; Wing et al., 2018). The fact that RCE generates flows with many different scales makes RCE a suitable model for tackling the mystery of the mesoscale -5/3 spectrum and subgrid modelling in convectively driven atmospheric flows. The -5/3 kinetic energy spectrum has been identified from wavelengths of around 400 km to small scales (e.g. Nastrom and Gage, 1985). Although the -5/3 mesoscale kinetic energy spectrum has been found in idealized cloud-resolving simulations (e.g. Bryan et al., 2003; Sun et al., 2017; Lai and Waite, 2020), it is still unclear what mechanisms are responsible for the -5/3 spectrum.

The modelling of turbulence in fluid flow is fundamentally important for numerical model predictions. Atmospheric flows, such as a mesoscale convective system, have length scales that range from the order of 1000 km in the largest eddies to the order of millimetres in dissipative eddies (e.g. Bryan et al., 2003). Even in the foreseeable future, the best supercomputer will still not be capable of performing a direct numerical simulation (DNS), which resolves eddies at all scales, in an atmospheric simulation. Because of that, large eddy

simulation (LES) was introduced (Smagorinsky, 1963; Lilly, 1967). LES resolves the large-scale energy-containing eddies and parameterizes the effects of subgrid scale turbulence. However, there is still room for improvement in parameterizing subgrid turbulence. A subfilter energy transfer analysis based on high-resolution simulations can help to identify the weakness of current, commonly-used subgrid turbulence schemes and propose a new scheme for improvement.

RCE is an ideal platform to perform a kinetic energy spectra analysis and a subfilter energy transfer analysis because many interacting convective systems of different scales are created in RCE. RCE is a statistically equilibrium state in which surface latent and sensible heat fluxes are balanced by radiative cooling. Because of that, it can run for a long time. The fact that RCE can run to statistical equilibrium, allows for the calculation of time averages of various turbulent quantities over many turnover times. Time and spatial averages can be used to improve the quality of the results. Atmospheric kinetic energy spectra and subfilter energy transfer analysis have not been done on RCE and they can improve our understanding of the dynamics of RCE, and the role of convection in maintaining the KE spectrum in the atmosphere.

In this thesis, we will perform an analysis of the kinetic energy spectra and spectral energy budget in RCE. There are three major research chapters in my thesis: analysis of kinetic energy spectra and spectral energy budget of RCE, analysis of subfilter energy transfer, and investigation into backscatter-allowing subgrid turbulence schemes. In this introduction section, we will introduce the governing equations, some background on RCE, the atmospheric energy spectrum, large eddy simulation, the Weather Research and Forecasting Model and an Eliassen-Palm inspired wave-mean flow interaction analysis.

1.2 Governing Equations

The set of governing equations consists of the continuity equation, the momentum equations, the energy equation for air and the governing equations for the moist variables.

1.2.1 The Continuity Equation

The continuity equation is a fundamental equation that is derived from conservation of mass. Since mass should be conserved in a material volume, the time derivative of the volume integral of the density should be zero. Hence, the integral form of the continuity

equation is given by

$$\frac{d}{dt}\int_{V(t)} \rho dV = \int_{V(t)} \frac{\partial \rho}{\partial t} + \boldsymbol{\nabla}\cdot(\rho \boldsymbol{u})\, dV = 0. \tag{1.1}$$

Since the choice of the material volume is arbitrary and the integral form of the continuity equation (1.1) is zero, the integrand must also be zero. As a result, the continuity equation is

$$\frac{\partial \rho}{\partial t} + \boldsymbol{\nabla}\cdot(\rho \boldsymbol{u}) = 0. \tag{1.2}$$

1.2.2 The Momentum Equations

Similarly, one can also derive the momentum equations from the conservation of momentum. With the consideration of the gravitational force and stress acting on the fluid, the momentum equation is given by (e.g. Kundu and Cohen, 2001)

$$\rho \frac{Du_i}{Dt} = \rho g_i + \frac{\partial \tau_{ij}}{\partial x_j}, \tag{1.3}$$

where ρg_i is the gravitational force and τ_{ij} is the stress tensor, which gives the i-th component of the stress on the fluid with outward normal in the j-th direction (Kundu and Cohen, 2001). The stress tensor can represent molecular viscosity or subgrid stress tensor when filtered variables are used (see section 1.5). Einstein notation, in which repeated indices represent summation, is used here. For Newtonian fluids, the constitutive equation is

$$\tau_{ij} = -p\delta_{ij} + 2\mu s_{ij} + \lambda \boldsymbol{\nabla}\cdot\boldsymbol{u}\delta_{ij}, \tag{1.4}$$

where

$$s_{ij} = \frac{1}{2}\left(\frac{\partial u_i}{\partial x_j} + \frac{\partial u_j}{\partial x_i}\right)$$

is the strain rate tensor, δ_{ij} is the Kronecker delta, μ is the dynamic viscosity and λ is the bulk viscosity. The viscosity will not be considered in this thesis because the Reynolds number is very large.

1.2.3 Energy Equation for Dry Air

To obtain the energy equation for the dry air, we need to consider the thermodynamic effect of the dry air. The dry air obeys the ideal gas law, which is given by (e.g. Rogers

and Yau, 1996)

$$p\alpha = R^{'}T, \tag{1.5}$$

where $\alpha = 1/\rho$ is the specific volume, $R^{'} = 287$ J kg^{-1}K^{-1} is the individual gas constant, p is the pressure and T is the temperature.

The first law of thermodynamics states that energy is conserved. Therefore, the internal energy of the system is equal to the sum of the heat added to the system and the work done by the system. The first law of thermodynamics for a unit of mass of gas is given by (e.g. Rogers and Yau, 1996),

$$du = dq - pd\alpha, \tag{1.6}$$

where du is the change in internal energy of the system per unit mass, dq is the heat added to the system per unit mass, and $pd\alpha$ is the work done by the gas. It can also be expressed in the following form:

$$dq = c_v dT + pd\alpha, \tag{1.7}$$

$$= c_p dT - \alpha dp, \tag{1.8}$$

where $c_v = 718$ J kg^{-1}K^{-1} is the specific heat at constant volume and $c_p = 1005$ J kg^{-1}K^{-1} is the specific heat at constant pressure.

Combining the first law of thermodynamics and the equation of state for dry air, we obtain the energy equation for dry air (e.g. Vallis, 2006)

$$\frac{Dln(\theta)}{Dt} = \frac{\dot{Q}}{Tc_p},$$

where θ is the potential temperature, $\dot{Q}$ is the rate of change of heat added to the dry air. The following is another form of the energy equation for dry air:

$$c_p \frac{DT}{Dt} - \alpha \frac{Dp}{Dt} = \dot{Q}.$$

which is used in the next section for the derivation of the moist static energy budget.

1.2.4 Anelastic Approximation

The anelastic approximation is often used to simplify the governing equations in the atmosphere, due to the fact that density changes with height are more significant than the changes in the horizontal (Vallis, 2006). The anelastic approximation assumes that the

density (ρ), pressure (p) and potential temperature (θ) can be written as the sum of a hydrostatically balanced state which is a function of height $\overline{(\cdot)}$ and a small perturbed state $(\cdot)'$:

$$\rho = \overline{\rho}(z) + \rho'(x, y, z, t), \tag{1.9}$$
$$p = \overline{p}(z) + p'(x, y, z, t), \tag{1.10}$$
$$\theta = \overline{\theta}(z) + \theta'(x, y, z, t). \tag{1.11}$$

With the anelastic approximation, the set of governing equations with a simple microphysics scheme that considers only water vapour, cloud water and precipitation is written as (e.g. Vallis, 2006)

$$\frac{D\boldsymbol{v}}{Dt} + f\hat{\mathbf{z}} \times \boldsymbol{v} = \hat{\boldsymbol{k}} g \frac{\theta'_m}{\overline{\theta}} - \boldsymbol{\nabla}\left(\frac{p'}{\overline{\rho}}\right) + \frac{\partial \tau_{ij}}{\partial x_j}, \tag{1.12}$$
$$\theta_m = \theta(1 + \frac{R_v}{R'} q_v) = \theta(1 + 1.608 q_v) \tag{1.13}$$
$$\nabla \cdot (\overline{\rho}\, \boldsymbol{v}) = 0, \tag{1.14}$$
$$\frac{D\theta}{Dt} = \frac{L\theta_e}{c_p T_e}(C_d + E_p), \tag{1.15}$$
$$\frac{Dq_v}{Dt} = -C_d - E_p, \tag{1.16}$$
$$\frac{Dq_c}{Dt} = C_d - A_p - C_p, \tag{1.17}$$
$$\frac{Dq_p}{Dt} = \frac{1}{\overline{\rho}} \frac{\partial(\overline{\rho} V_T q_p)}{\partial z} + A_p + C_p + E_p, \tag{1.18}$$

where $\boldsymbol{v}$=(u,v,w)=(u_1,u_2,u_3) is the velocity vector in three dimensions, ∇ is the three-dimensional gradient operator, T is the temperature, f is the Coriolis parameter, θ_e is the ambient potential temperature, T_e is the ambient temperature, τ_{ij} is the subgrid-scale stress tensor, which represents subgrid turbulence mixing modelling, q_v is the water vapour mixing ratio, q_c is the cloud water mixing ratio, q_p is the precipitation mixing ratio, the E are the evaporation terms, the C are the condensation terms, the A are the autoconversion terms, and V_T is the terminal velocity for the precipitation (Grabowski and Smolarkiewicz, 2002). $\theta'_m = \theta_m - \overline{\theta}$ is the perturbation of θ from the steady, dry, hydrostatically balanced $\overline{\theta}$ (Peng et al., 2015a). These equations include the schematic of a simple microphysics model with three water species: q_v, q_c, and q_p. In more sophisticated microphysics schemes, additional species are included. $\dot{Q}$ is the diabatic heating (Vallis, 2006), which includes subgrid mixing, radiation, latent heating, and sensible heating.

1.3 What is Radiative-Convective Equilibrium?

Radiative-convective equilibrium is a state of a climate system in which surface latent and sensible heat fluxes are balanced by radiative cooling. In recent years, RCE simulations have been used to understand the parameterization of clouds and convection (Becker et al., 2017) and problems associated with tropical cyclones, such as identifying what environmental parameters are favourable for tropical cyclones (Nolan et al., 2007).

Since the tropical areas are often close to RCE, RCE is often used to study convective systems. A phenomenon called self-aggregation in RCE has attracted a lot of attention in the weather forecasting and cloud-resolving model communities. Self-aggregation is the phenomenon in which some random clusters of cloud organize into one or a small number of large, persistent convective systems. Some factors, such as subgrid parameterization and even domain size (e.g. Bretherton et al., 2005; Wing and Emanuel, 2014; Tompkins and Semie, 2017) are known to affect self-aggregation. In an aggregated simulation, once aggregation is formed, it is very hard to disaggregate. Unlike in a non-aggregated simulation, although large-scale structures can form, those large-scale structures do not stay attached for a long period of time. The moist static energy is often used to quantify whether the climate system is at an equilibrium state or not. Investigation of self-aggregation has also been performed with moist static energy (Wing et al., 2017). In the next subsection, we will derive the moist static energy budget.

1.3.1 Moist Static Energy Budget

To derive the moist static energy budget, we start by considering the energy equation for dry air:

$$c_p \frac{DT}{Dt} - \alpha \frac{Dp}{Dt} = \dot{Q}, \tag{1.19}$$

where $\alpha = 1/\rho$ is the specific volume and p is the full, not perturbation, pressure. Combine (1.19) with hydrostatic balance (Vallis, 2006), we obtain

$$c_p \frac{DT}{Dt} + g \frac{Dz}{Dt} = \dot{Q}. \tag{1.20}$$

The dry static energy is $s = c_p T + gz$ (Holton and Hakim, 2012). From (1.20),

$$\frac{Ds}{Dt} = \dot{Q} = \partial_z F_S + \partial_z F_R + \dot{Q}_{LH}. \tag{1.21}$$

Here $\dot{Q}$ is decomposed into contributions from the divergence of the upward vertical flux from radiation (F_R), diffusion of sensible heat (F_S), and latent heat ($\dot{Q}_{LH}$) (Neelin and Held, 1987). Note that the dry static energy is conserved when there is no diabatic heating, but it is not conserved in the presence of phase changes.

When liquid water is present, the effect of phase changes, which motivates the introduction of moist static energy, has to be considered. Note that when the rate of change of q_v is multiplied by the specific latent heat L, the latent heat due to phase changes can be written as the sum of $-\dot{Q}_{LH}$ and $\partial_z F_L$, where F_L is the latent heat flux due to diffusion of moisture (Neelin and Held, 1987),

$$\frac{DLq_v}{Dt} = L(-C_d - E_p) = -\dot{Q}_{LH} + \partial_z F_L. \tag{1.22}$$

Let $h = s + Lq_v$ be the moist static energy (Holton and Hakim, 2012). Combining the contribution from phase change and the dry static energy, the moist static energy equation is given by

$$\frac{Dh}{Dt} = \partial_z F_S + \partial_z F_R + \partial_z F_L. \tag{1.23}$$

There are three contributing factors to the moist static energy budget, namely sensible heat flux, latent heat flux and radiation. They can be written as $\partial_z F_S$, $\partial_z F_L$ (due to diffusion of moisture), and $\partial_z F_R$, respectively.

Using the notation

$$\langle A \rangle_z = \int_{surface}^{top} \rho A dz,$$

we can derive the vertically-integrated moist static energy budget. Since $w = 0$ at the top and bottom boundaries, vertically integrating (1.23) yields

$$\frac{\partial \langle h \rangle_z}{\partial t} + \nabla_h \cdot \langle h\mathbf{u} \rangle_z = SH + \dot{Q}_{rad} + LH, \tag{1.24}$$

where ∇_h is the horizontal gradient operator, and $\boldsymbol{u}$ is the horizontal velocity. SH, $\dot{Q}_{rad}$, and LH are the differences of the sensible heat, radiative, and latent heat fluxes between the top and bottom.

RCE is a state of a climate system in which surface latent heat, surface sensible heat flux, and radiative cooling are balanced. Those three contributions are all present in the moist static energy budget. As a result, the moist static energy budget is useful for

determining whether the climate system is at RCE or not. Note that the effect of ice can also be taken into consideration when the frozen moist static energy (FMSE) is used. The frozen moist static energy h_f is given by

$$h_f = c_p T + gz + L_v q_v - L_f q_{ice}. \tag{1.25}$$

When we replace h with h_f in (1.23), we obtain the frozen moist static energy budget. The effects of ice are considered in the sensible heat and latent heat terms.

1.4 Turbulence and Energy Cascade

Turbulent flow is unpredictable and chaotic. Turbulent flow is characterized by the Reynolds number, which is a dimensionless quantity that compares the effect of inertial force and viscosity. The Reynolds number is defined as

$$Re = \frac{UL}{\nu},$$

where U and L are the characteristic velocity and length of the turbulent flow, respectively, and ν is the kinematic viscosity. A turbulent flow has a high Reynolds number.

Turbulent eddies exhibit a wide range of length scales. In three-dimensional unstratified turbulence, energy is found to be cascading downscale (e.g. Wyngaard, 2010). To show that there is a downward energy cascade in isotropic turbulence, we first consider the equation for turbulence kinetic energy (TKE). The TKE is defined as

$$e = \frac{\overline{u_i u_i}^R}{2},$$

where u_i is the velocity fluctuations from the Reynolds average velocity U_i (e.g. the ensemble average over many realizations of the flow) and $\overline{M}^R$ represents the mean (Reynolds average) of quantity M. One can obtain the TKE equation by multiplying the equation for velocity fluctuation by u_i (Wyngaard, 2010):

$$\frac{\partial}{\partial t}\left(\frac{\overline{u_i u_i}^R}{2}\right) = -U_j \frac{\partial}{\partial x_j}\left(\frac{\overline{u_i u_i}^R}{2}\right) - \overline{u_i u_j}^R \frac{\partial U_i}{\partial x_j} + \frac{\partial}{\partial x_j}\left(\frac{\overline{u_i u_i u_j}^R}{2}\right) - \frac{1}{\rho}\frac{\partial}{\partial x_i}\overline{p u_i}^R + \overline{\nu u_i \frac{\partial^2 u_i}{\partial x_j \partial x_j}}^R \tag{1.26}$$

$$= -\frac{\partial}{\partial x_j}\left[U_j \frac{\overline{u_i u_i}^R}{2} + \frac{\overline{u_i u_i u_j}^R}{2} + \frac{\overline{p u_j}^R}{\rho} + 2\nu(\overline{u_i s_{ij}}^R)\right] - \overline{u_i u_j}^R \bar{s}_{ij}^R - 2\nu \overline{s_{ij} s_{ij}}^R, \tag{1.27}$$

where $s_{ij} = \frac{1}{2}\left(\frac{\partial u_i}{\partial x_j} + \frac{\partial u_j}{\partial x_i}\right)$, $G = -\overline{u_i u_j}^R \bar{s_{ij}}^R$ is the mean gradient production and $\epsilon = 2\nu\overline{s_{ij}s_{ij}}^R$ is the viscous dissipation. One can see that in stationary turbulence, assuming no flux through the boundary, the volume integral of (1.27) is

$$\int_V G dV = \int_V \epsilon dV. \tag{1.28}$$

Note that the mean gradient production G happens at the energy-containing scale l, and the viscous dissipation ϵ happens at the dissipative scale η in three-dimensional turbulence. The result from (1.28) indicates that there is a balance between energy injection and dissipation. If energy injection happens at large scales and dissipation happens at small scales, there must be a downscale cascade.

While it is informative to know that energy transfers from large scales to small scales before the energy is dissipated by viscous effects, we still have not shown how the energy is transferred downscale in the discussion above. Is the energy from large scales directly transferred to the small scales? Or is the energy transferred from the large energy-containing eddies to smaller and smaller eddies until it is transferred to the dissipative scale eddies? To tackle this problem, Richardson (1922) suggested the idea of the turbulence energy cascade. The idea of the energy cascade is that large eddies transfer energy to slightly smaller eddies. The process goes on until the energy reaches the scale of dissipative eddies, and the energy will be removed by dissipation. The idea of energy cascade is captured by the beautiful poem by Richardson (1922): "Big whirls have little whirls that feed on their velocity; and little whirls have lesser whirls and so on to viscosity." It is found that the physical mechanism of the cascade is vortex stretching. Energy transfer between eddies of similar sizes is found to be most efficient(Tennekes and Lumley, 1972) and hence energy is dominated by the transfer from slightly larger eddies to slightly smaller eddies.

1.4.1 Kolmogorov's 1941 Theory

Richarson's energy cascade hypothesis suggests that for $k \gg k_i$, where k_i is the wavenumber of the large-scale forcing, the information of the large-scale forcing will be forgotten after many steps of the energy cascade process. The concept of universal equilibrium range at $k \gg k_i$ is then suggested by Kolmogorov (1941). In the universal equilibrium range of isotropic turbulence, the kinetic energy spectrum $E(k)$ only depends on the wavenumber k, dissipation ϵ, and dissipation wavenumber k_d. Using dimensional analysis, one finds that (e.g. Wyngaard, 2010)

$$E(k) = \epsilon^{2/3} k^{-5/3} f(k/k_d). \tag{1.29}$$

If we further restrict our wavenumber k to be $k_i \ll k \ll k_d$, which is also known as the inertial subrange, then $E(k)$ is independent of k_d. This will further simplify the energy spectrum to (e.g. Wyngaard, 2010)

$$E(k) = c\epsilon^{2/3}k^{-5/3}, \tag{1.30}$$

where c is a constant. This is also known as the -5/3 spectrum in isotropic turbulence.

1.4.2 Kinetic Energy Spectrum in the Atmosphere

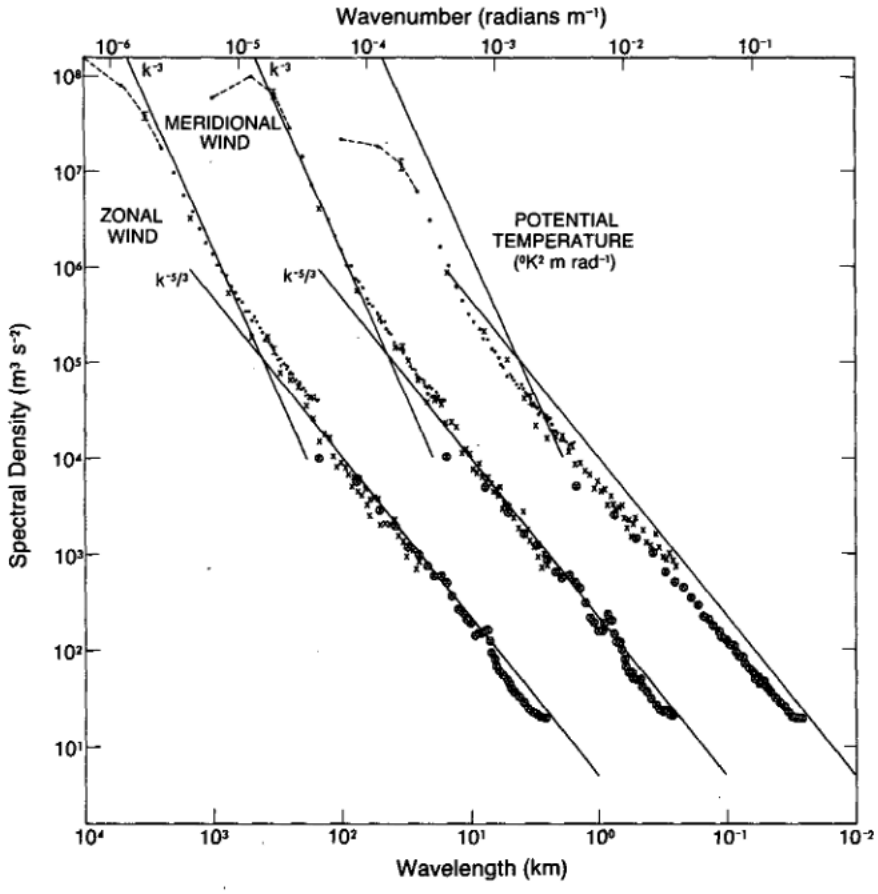


Figure 1.1: Observed zonal and meridional wind atmospheric kinetic energy spectra (Nastrom and Gage, 1985) © American Meteorological Society. Used with permission.

Atmospheric measurements (Fig. 1.1) show a k^{-3} energy spectrum for synoptic scales in midlatitudes and a shallower $k_h^{-5/3}$ energy spectrum at mesoscales (Nastrom and Gage, 1985), where k_h is the horizontal wavenumber. Kolmogorov's theory suggests that there is a -5/3 kinetic energy spectrum in the inertial subrange for isotropic turbulence. However, the scale of isotropic turbulence is often down to scales of centimetres or even millimetres, which are a lot smaller than the atmospheric mesoscales. The issue is that the troposphere is only 10-15 km thick, and horizontal scales are on the order of 100-1000 km. Since the vertical scales are on the order of just 10 km, the turbulence in the troposphere cannot be isotropic at mesoscale length scales. Hence, the mesoscale -5/3 spectrum is not isotropic 3D turbulence. As a result, the dimensional analysis above for isotropic turbulence is not relevant in the mesoscales in the atmosphere. While there is a general agreement on the explanation of the k^{-3} spectrum based on the quasigeostrophic turbulence theory by Charney (1971), there is no agreement on the mechanics responsible for the $k^{-5/3}$ energy spectrum. The idea of upscale energy cascade was proposed in early works (Gage, 1979; Lilly, 1983), but there is more recent evidence that suggests that the energy transfer is downscale (e.g. Cho and Lindborg, 2001). Some other theories are based on stratified turbulence (e.g. Lindborg, 2006) and inertia-gravity waves (e.g. Dewan, 1979; VanZandt, 1982; Bartello, 1995; Callies et al., 2016). However, the mesoscale has other physics, such as moist physics, surface physics, and radiative cooling. It has been shown that moist processes can inject energy in the mesoscale in a baroclinic wave (Waite and Snyder, 2013), which shows that physics may play a role in the mesoscale spectrum. In Chapter 2 of this thesis, we will examine the energy spectrum and energy budget in RCE.

1.5 LES and the TKE Subgrid Turbulence Scheme

In an ideal world where computational power is unlimited, every atmospheric turbulent flow, from the large energy-containing scales to the small dissipative scales, would be resolved by direct numerical simulations (DNS). DNS solves the set of governing equations (Navier-Stokes equations) numerically without any parameterizations for turbulence. However, computational resources to this day are still not capable of performing a DNS at atmospheric scales (e.g. Bryan et al., 2003; Wyngaard, 2010). As a result, large eddy simulation (LES) is proposed (Smagorinsky, 1963). Since it is expensive to resolve the small-scale eddies, the idea of LES is to reduce the computational cost by resolving the large energy-containing eddies and parameterizing the small-scale eddies (e.g. Lesieur and Metais, 1996; Pope, 2000; Wyngaard, 2010; Piomelli, 2014).

To illustrate the idea of parameterizing small-scale eddies, we can consider a simple

example of the inviscid Burgers' equation

$$\frac{\partial u}{\partial t} + u\frac{\partial u}{\partial x} = 0.$$

We can apply a low-pass spatial filter $\overline{(\cdot)}$ to get

$$\frac{\partial \overline{u}}{\partial t} + \overline{u\frac{\partial u}{\partial x}} = 0.$$

To obtain the Burgers equation with the filtered velocity, we have to manipulate the non-linear term to get

$$\frac{\partial \overline{u}}{\partial t} + \frac{1}{2}\overline{\frac{\partial uu}{\partial x}} = 0$$

$$\frac{\partial \overline{u}}{\partial t} + \frac{1}{2}\frac{\partial \bar{u}\bar{u}}{\partial x} = -\frac{1}{2}\left(\frac{\partial \overline{uu}}{\partial x} - \frac{\partial \bar{u}\bar{u}}{\partial x}\right).$$

The right side of the filtered Burgers' equation represents the subfilter scale effect. The same logic applies to the three-dimensional momentum equations.

To parameterize the effect of small-scale eddies in LES, the equations are filtered with a low-pass filter to remove small spatial scales (e.g. Bryan et al., 2003; Wyngaard, 2010). The modified filtered momentum equations are

$$\frac{\partial \overline{u_i}}{\partial t} + \frac{\partial(\bar{u}_i\bar{u}_j)}{\partial x_j} = -\frac{\partial(\overline{p}/\rho + (\overline{u_iu_i} - \bar{u}_i\bar{u}_i)/3)}{\partial x_i} - \frac{\partial \tau^d_{ij}}{\partial x_j}, \tag{1.31}$$

where

$$\tau^d_{ij} = \overline{u_iu_j} - \bar{u}_i\bar{u}_j - \frac{1}{3}(\overline{u_iu_i} - \bar{u}_i\bar{u}_i)\delta_{ij}.$$

The filter is denoted by an overbar on a variable:

$$\overline{u_i} = \iiint u_i(\boldsymbol{x}')G(\boldsymbol{x} - \boldsymbol{x}')dx_1'dx_2'dx_3',$$

where G is a filter function.

To model the unresolved subfilter scales, a subgrid scale model is used. Without the use of a subgrid scale model, the energy transfer between the resolved scale and the subgrid scale will be inaccurate. A well-designed model can simulate an atmospheric turbulent flow in the best possible way by accurately representing τ^d_{ij}. A commonly used subgrid scale model is the eddy viscosity model. The eddy viscoity model was introduced by Lilly and

Smagorinsky (e.g. Smagorinsky, 1963; Lilly, 1967). The eddy viscosity model is built on the energy cascade hypothesis from Richardson (1922). The eddy viscosity model (or LES in general) requires the resolution of the simulation to adequately resolve the large energy-containing eddies, but not in the Kolmogorov dissipative range (e.g. Pope, 2000; Wyngaard, 2010). The energy from the large energy-containing eddies will eventually transfer to the small, unresolved scales, and this energy will be dissipated by the eddy viscosity model. The size of the dissipative eddies in this thesis is in the order of millimetres. The eddy viscosity model parameterizes τ_{ij}^d using a viscosity-like term called eddy viscosity, which is denoted by K in the following.

$$\tau_{ij}^d = -2K\overline{S_{ij}}, \tag{1.32}$$

where

$$\overline{S_{ij}} = \frac{1}{2}\left(\frac{\partial \overline{u_i}}{\partial x_j} + \frac{\partial \overline{u_j}}{\partial x_i}\right)$$

is the filtered strain rate tensor.

In this thesis, the turbulence kinetic energy (TKE) closure model will be used (e.g. Pope, 2000; Wyngaard, 2010). The TKE scheme is considered to be an improvement from the original Smagorinsky scheme (e.g. Smagorinsky, 1963; Wyngaard, 2010) from Lilly and Smagorinsky. The Smagorinsky scheme calculates the eddy viscosity only with the filtered strain rate, whereas the TKE scheme takes the TKE into consideration when calculating the eddy viscosity. The TKE closure model is given by

$$K = C_u e^{1/2} \Delta, \tag{1.33}$$

where $C_u = 0.15$ (Skamarock et al., 2008) and $e = (\overline{u_i u_i} - \bar{u}_i \bar{u}_i)/2$ is the subgrid TKE. e is the subgrid turbulence kinetic energy, and its evolution is predicted with a model equation (Wyngaard, 2010).

The TKE scheme plays an important role throughout this thesis. In Chapter 2, the aggregated simulation has an increased eddy viscosity. In Chapter 4, the TKE scheme is modified to propose a backscatter-allowing stochastic subgrid turbulence scheme. The exact details of the TKE scheme will be provided in the methodology section of each chapter.

1.6 Weather Research and Forecasting Model

In this thesis, simulations are performed with the Weather Research and Forecasting model (WRF) (Skamarock et al., 2008). WRF, a mesoscale numerical weather prediction and

forecasting model, is widely used in both research and operational forecasting activities. WRF is well-supported by a user forum, and details of WRF are also well-documented in the WRF technical manual (Skamarock et al., 2008). WRF can work with both real data simulations, which are initialized and forced by reanalysis, and idealized simulations, which use simplified initial and boundary conditions. The goal of an idealized model is to focus on a certain aspect of the atmosphere that one may want to study, and not to worry about the real world complexities. The governing equations that WRF works with are the fully compressible, non-hydrostatic Euler equations (Skamarock et al., 2008). WRF uses time-splitting to damp the acoustic modes. So, even though it solves the compressible equations, the dynamics are closer to anelastic. To solve the equations, WRF uses a third-order Runge-Kutta scheme in time, a third-order upwind-bias finite-difference advection scheme in the vertical direction and a fifth-order upwind-bias finite-difference advection scheme in the horizontal directions (Skamarock et al., 2008). To discretize the grid, WRF uses the Arakawa C-grid discretization. The Arakawa C-grid system staggers velocities at the edge of the cell and other variables, such as the potential temperature at the mass point.

In WRF, a terrain-following vertical coordinate called the eta coordinate is used. A terrain-following vertical coordinate system adjusts according to the bottom topography of the domain. Since terrain-following vertical coordinates adjust based on the topography, it is convenient for simulations with uneven terrain. Since model surfaces are not flat, terrain-following vertical coordinates require extra care when computing the vertical and horizontal derivatives of a quantity. The eta vertical coordinates define the vertical coordinate using the hydrostatic pressure. In WRF, the eta coordinate is defined as (Skamarock et al., 2008):

$$\eta = (p_{dh} - p_{dht})/\mu_d,$$

where $\mu_d = p_{hs} - p_{ht}$, p_{hs} is the surface dry hydrostatic pressure, p_{dh} is the dry hydrostatic pressure, and p_{dht} is the top of the domain dry hydrostatic pressure. The set of governing

equations rewritten using the eta coordinate is (Skamarock et al., 2008)

$$\frac{\partial U}{\partial t} + \nabla \cdot (\mathbf{V}u) + \mu_d \alpha \frac{\partial p}{\partial x} + (\alpha/\alpha_d)\frac{\partial \phi}{\partial x}\frac{\partial p}{\partial \eta} = F_U, \tag{1.34a}$$

$$\frac{\partial V}{\partial t} + \nabla \cdot (\mathbf{V}v) + \mu_d \alpha \frac{\partial p}{\partial y} + (\alpha/\alpha_d)\frac{\partial \phi}{\partial y}\frac{\partial p}{\partial \eta} = F_V, \tag{1.34b}$$

$$\frac{\partial W}{\partial t} + \nabla \cdot (\mathbf{V}w) - g\left((\alpha/\alpha_d)\frac{\partial p}{\partial \eta} - \mu_d\right) = F_W, \tag{1.34c}$$

$$\frac{\partial \Theta}{\partial t} + \nabla \cdot (\mathbf{V}\theta) = F_\theta, \tag{1.34d}$$

$$\frac{\partial \mu_d}{\partial t} + (\nabla \cdot \mathbf{V}) = 0, \tag{1.34e}$$

$$\frac{\partial \phi}{\partial t} + \mu_d^{-1}[(\mathbf{V} \cdot \nabla\phi) - gW] = 0, \tag{1.34f}$$

$$\frac{\partial Q_m}{\partial t} + \nabla \cdot (\mathbf{V}q_m) = F_{Q_m}, \tag{1.34g}$$

$$\frac{\partial \phi}{\partial \eta} = -\alpha_d/\mu_d, \tag{1.34h}$$

$$p = p_0(R_d\theta_m/p_0\alpha_d)^\gamma, \tag{1.34i}$$

where $\mathbf{V} = (U, V, W) = \mu_d(u, v, w)$ is the adjusted velocity, $\Theta = \mu_d\theta$ is the adjusted potential temperature, $\phi = gz$ is the geopotential, and p is the pressure. The divergence term is given by

$$\nabla \cdot \mathbf{V}a = \frac{\partial(\mu_d u a)}{\partial x} + \frac{\partial(\mu_d v a)}{\partial y} + \frac{\partial\left(\mu_d \frac{d\eta}{dt} a\right)}{\partial \eta},$$

where F_U, F_V, F_W, F_θ and F_{Q_m} are the forcing by various parameterization for U, V, W, θ and the mixing ratios, respectively. The details of the forcings, which are listed in Skamarock et al. (2008), depend on the parameterizations used in WRF and can include parameterizations for subgrid turbulence, boundary layer turbulence, microphysics, and radiative transfer. $\theta_m = \theta(1 + (R_v/R_d)q_v)$, $Q_m = \mu_d q_m$ is the adjusted mixing ratio and mixing ratio of various content of water (q_m), such as the water vapour, cloud, rain and ice are represented by q_v, q_c and q_i, respectively.

1.7 Eliassen-Palm Flux-Like Analysis

To better understand the interaction between the horizontally averaged flow and waves, we consider an analysis that is inspired by the Eliassen-Palm flux discussion from Menchaca

and Durran (2019). The idea of the analysis is that we will apply a horizontal mean operator, denoted by $\overline{(\cdot)}^h$, to the momentum equation. Because of the use of periodic boundary conditions in this thesis, all the horizontal derivatives (cf. 1.12) will vanish when the horizontal mean is applied. The only terms left will be the terms with vertical derivative. Without the loss of generality, we apply the horizontal mean to the momentum equation in x direction (1.12)

$$\overline{\rho}^h \frac{\partial \overline{u}}{\partial t} = -\frac{\partial \overline{\overline{\rho}^h uw}^h}{\partial z}. \tag{1.35}$$

Note that the term on the right is the horizontally averaged nonlinear advection. We continue to separate the full velocity u and w into the horizontal-averaged velocity $\overline{u}^h$ and $\overline{w}^h$ and the perturbation of the velocity from the mean u' and w', respectively (ie. $u = \overline{u}^h + u'$ and $w = \overline{w}^h + w'$). Since $\overline{u'}^h = 0$ and $\overline{w'}^h = 0$,

$$\frac{\partial \overline{\overline{\rho}^h(\overline{u}^h + u')}^h}{\partial t} = -\frac{\partial \overline{\overline{\rho}^h(\overline{u}^h + u')(\overline{w}^h + w')}^h}{\partial z}, \tag{1.36}$$

$$\overline{\rho}^h \frac{\partial \overline{u}^h}{\partial t} = -\frac{\partial \overline{\rho}^h \, \overline{u'w'}^h}{\partial z} - \frac{\partial \overline{\rho}^h \overline{u}^h \, \overline{w}^h}{\partial z}. \tag{1.37}$$

Similarly,

$$\overline{\rho} \frac{\partial \overline{v}^h}{\partial t} = -\frac{\partial \overline{\rho}^h \, \overline{v'w'}^h}{\partial z} - \frac{\partial \overline{\rho}^h \overline{v}^h \, \overline{w}^h}{\partial z}. \tag{1.38}$$

We can multiply both equations by the mean quantity and sum up the two equations to obtain the horizontal kinetic energy of the mean flow. The horizontal mean operator $\overline{(\cdot)}^h$ is replaced by $\overline{(\cdot)}$ for clarity

$$\frac{\overline{\rho}}{2}\frac{\partial \overline{u}^2}{\partial t} + \frac{\overline{\rho}}{2}\frac{\partial \overline{v}^2}{\partial t} = \left(-\overline{u}\frac{\partial \overline{\rho}\,\overline{u'w'}}{\partial z} - \overline{v}\frac{\partial \overline{\rho}\,\overline{v'w'}}{\partial z}\right) + \left(-\overline{u}\frac{\partial \overline{\rho}\,\overline{u}\,\overline{w}}{\partial z} - \overline{v}\frac{\partial \overline{\rho}\,\overline{v}\,\overline{w}}{\partial z}\right). \tag{1.39}$$

The first bracket on the right-hand side of the equation is the contribution from the wave, which is also called the EP flux contribution in Chapter 2. The second bracket on the right-hand side of the equation is the contribution from the mean flow. To improve readability, the superscript h will be dropped in the EP flux discussion in Chapter 2.

1.8 Thesis Objectives

The goal of this thesis is to understand the dynamics of the kinetic energy spectrum and inter-scale energy transfers and use this to develop a new subgrid turbulence scheme. The

three main objectives in this thesis are listed in this paragraph. The detailed introductions of each topic are given in the corresponding chapters. The first objective of this thesis is to explore the mechanism responsible for self-aggregation by using the kinetic energy spectrum and the spectral energy budget analysis, and to determine if self-aggregation can be understood as a turbulent inverse cascade. The second objective is to investigate the subgrid energy transfer rate by measuring the actual cross-filter energy transfer in filtered LES. The third objective is to use the result from the analysis of subfilter energy transfer to propose a modified subgrid turbulence mixing scheme. More details on the three objectives are provided below.

1.8.1 Kinetic Energy Spectrum and the Spectral Energy Budget Analysis in RCE

In Chapter 2, we perform an analysis of the kinetic energy spectrum and the spectral energy budget analysis in RCE. One of the unsolved problems in the field of atmospheric turbulence research is the origin of the mesoscale $-5/3$ spectrum. The scales of isotropic turbulence are not relevant to the scales of the flow of atmospheric structures, and yet the $-5/3$ spectrum exists in atmospheric observations and numerous numerical weather forecasting experiments. Would the $-5/3$ spectrum exist in RCE simulations? If so, what are the mechanisms responsible for that? Is an energy cascade important in explaining the energy spectrum? In addition, the mechanisms that are responsible for self-aggregation are still unclear. Performing a kinetic energy spectrum and the spectral energy budget analysis in RCE will improve our understanding of how subgrid parameterizations contribute to the atmospheric energy cascade. The spectral energy budget analysis will also help us to better understand self-aggregation.

1.8.2 Subfilter Energy Transfer Rate Analysis

In Chapter 3, in order to understand the energy transfer between the resolved and the subgrid, we will perform a subfilter energy transfer rate analysis by measuring the actual cross-filter energy transfer in a filtered convective-permitting simulation. In particular, high-resolution simulations will be filtered to a lower resolution to perform a priori analysis. The subgrid energy transfer at the filtered scale can be computed with the filtered data field. By identifying the important mechanism in the energy spectral budget, improvements of the corresponding subgrid process parameterization will be possible.

1.8.3 Proposed Backscatter-Allowing Stochastic Subgrid Turbulence Mixing Scheme

In Chapter 4, based on the analysis of the backscatter and backscatter-allowing mixing schemes, a backscatter-allowing stochastic subgrid turbulence mixing scheme is proposed. Kirkil et al. (2012) performed a large eddy simulation with a range of subgrid mixing schemes in WRF, from a relatively simple Smagorinsky scheme to some subgrid mixing schemes that were more complex, such as the Lagrangian-averaged scale-dependent dynamic (LASD) model and dynamic reconstruction models (DRM). While the simulation time with LASD and DRM was 25-28% longer than the Smagorinsky scheme, they were found to be more accurate than the Smagorinsky scheme. Berner et al. (2009) evaluated the spectral stochastic kinetic energy backscatter scheme with a numerical weather prediction model. This stochastic backscatter scheme created kinetic energy spectra that were more realistic, and it also predicted rainfall more accurately. As a result, simulations with backscatter parameterizations such as the stochastic kinetic-energy backscatter scheme (e.g. Berner et al., 2009, 2011) and the proposed backscatter-allowing stochastic subgrid turbulence mixing scheme can be used to compare to higher-resolution simulations with eddy viscosity models.

Chapter 2 is based on a published paper. Chapters 3-4 will be submitted to journals for peer review. Chapter 5 is the conclusion to the thesis, and future works are also suggested.

2

Kinetic Energy Spectra and Spectral Budget of Radiative-Convective Equilibrium

This chapter is based on the published paper, K. T. Lai and M. L. Waite. Kinetic Energy Spectra and Spectral Budget of Radiative–Convective Equilibrium. Journal of the Atmospheric Sciences 80.8 (2023): 1953-1970 DOI: https://doi.org/10.1175/JAS-D-22-0173.1
© American Meteorological Society. Used with permission.

2.1 Introduction

Radiative-convective equilibrium (RCE) is an idealized climate system driven by sensible and latent heat fluxes at the surface (Nolan et al., 2007; Wing et al., 2018). It is often considered as one of the simplest climate model configurations (Wing et al., 2018). We study the kinetic energy spectrum and spectral budget in simulations of RCE. A -5/3 kinetic energy spectrum has been identified from wavelengths of a few hundred km to small scales in both mid-latitudes (Nastrom and Gage, 1985) and the tropics (Cho et al., 1999). This spectrum is significant because -5/3 is the theoretical slope of a kinetic energy cascade, which suggests that an energy cascade may be occurring through the mesoscale. While the -5/3 kinetic energy spectrum has also been found in mesoscale simulations (e.g. Skamarock, 2004; Peng et al., 2014; Sun et al., 2017) and global simulations (e.g. Hamilton et al., 2008; Skamarock et al., 2014; Malardel and Wedi, 2016), the responsible physical mechanisms are still unclear.

Whether RCE will generate the -5/3 mesoscale spectrum is uncertain. RCE is at a statistical equilibrium and is driven by surface fluxes rather than baroclinic instability, which is different from most other idealized simulations of the mesoscale spectrum. Unlike mid-latitude simulations, in which kinetic energy is forced at the large scales by baroclinic instability, kinetic energy in RCE is forced by surface fluxes and radiative cooling, and the characteristic length scales of this forcing is not clear. One interesting aspect of RCE is the phenomenon of self-aggregation (Bretherton et al., 2005; Wing and Emanuel, 2014). Self-aggregation is the organization of some small random cloud clusters into one or several larger clusters. Self-aggregation is known to be sensitive to subgrid paramterisation and domain size (Bretherton et al., 2005; Wing and Emanuel, 2014; Tompkins and Semie, 2017). The effect of self-aggregation on the kinetic energy spectrum and energy cascade is still unknown. The fact that self-aggregation organizes small cloud clusters into large cloud clusters may affect how kinetic energy transfers from small scale to large scale in an inverse energy cascade. This connection between aggregation and the spectral budget is explored in this work.

2.1.1 RCE and Self-Aggregation

RCE is often used in model development and model comparison due to its simple configuration. In particular, it is used as a framework for understanding subgrid representations such as convective parameterizations (Becker et al., 2017) and cloud microphysics parameterizations (Satoh and Matsuda, 2009). Since RCE generates a flow with many interacting

convective systems at different scales, it has been employed in models with different horizontal resolutions such as atmospheric general circulation models (Reed and Medeiros, 2016) and cloud-resolving models (Muller and Held, 2012; Wing et al., 2017). The fact that RCE has been widely used in various models makes it a great framework for model comparisons. Reed and Medeiros (2016) used idealized RCE simulations to compare convection simulated in an atmospheric general circulation model at high resolution to convection simulated in cloud-resolving models. They concluded that high-resolution atmospheric general circulation model can produce convective systems found in cloud-resolving models. In particular, organized convective clusters which are often found in RCE simulations with cloud-resolving models are also found in their simulations with the high-resolution atmospheric general circulation model.

Self-aggregation is a phenomenon in which many small and random moist convective cores organize into a small number of large and isolated clusters (Wing et al., 2017). Self-aggregation in simulations is known to be sensitive to details of clouds parameterization (Satoh and Matsuda, 2009), microphysics (Colin et al., 2019), circulations (Muller and Bony, 2015), cold pool (Jeevanjee and Romps, 2013), SST (Bretherton et al., 2005; Wing et al., 2017), background wind (Robe and Emanuel, 2001; Nolan et al., 2007), horizontal resolution (Bretherton et al., 2005; Muller and Held, 2012) and domain size (Bretherton et al., 2005; Wing et al., 2017). Here, we review the literature to help us to understand the mechanisms and the importance of self-aggregation.

Bretherton et al. (2005) performed a moist static energy budget analysis and sensitivity tests of self-aggregation to domain sizes and physical parameterizations on a non-rotating radiative-convective equilibrium simulation. They found that self-aggregation did not happen in a small domain. They also found that both homogeneous surface fluxes or radiative cooling subdued self-aggregation. They suggested that the strong radiative cooling, due to the lack of high cloud, in the dry region created a low-level circulation that transported moist static energy from dry to moist region, which further dried the dry region and moistened the moist region. They also pointed out that ocean interactions slowed down the aggregation process.

Muller and Held (2012) found that self-aggregation was sensitive to domain size and horizontal resolution. Simulations with domain size larger than 200 km $\times$ 200 km and grid spacing larger than 2 km were found to be favourable for self-aggregation because of the effects of domain size and horizontal resolution on low clouds. Low clouds changed the response of longwave radiative cooling, which was found to be crucial to the formation of a circulation that transports moist static energy up-gradient from dry to moist regions. They also found that the interactive longwave radiative cooling was one of the keys to self-aggregation. When homogenous longwave radiative cooling was used, self-aggregation did

not occur even for simulations with large domain size and low resolution. While horizontal resolution affects the simulation results, increasing or decreasing the turbulence mixing by multiplying the eddy viscosity in the TKE closure subgrid turbulence scheme by a constant did not change the result in their study. Low resolution lowers the near-surface temperature and increases the near-surface water vapour mixing ratio. Hence, there was an increase in the low cloud in the dry regions and the cooling associated with it. Note that low clouds consist of only liquid condensates. They found that the contribution of surface fluxes to self-aggregation was positive, which was different from what was found in Bretherton et al. (2005). Bretherton et al. (2005) found no self-aggregation when the surface fluxes were homogeneous. Muller and Held (2012) suggested that if the surface fluxes were stronger, Bretherton et al. (2005) would be able to create self-aggregation. This hypothesis was confirmed by Holloway and Woolnough (2016), which found that the strength of the surface fluxes was crucial to self-aggregation.

The resolution dependence of self-aggregation in RCE in Muller and Held (2012) was found to be related to the strength of the subgrid turbulence mixing by Tompkins and Semie (2017). They performed an investigation of the role of updraft entrainment on self-aggregation. In particular, they performed idealized RCE simulations with 2D Smagorinsky, 3D Smagorinsky, and TKE subgrid turbulence mixing scheme. They found that when the 3D Smagorinsky scheme was used, self-aggregation occurred. When a less dissipative subgrid turbulence mixing scheme such as the TKE scheme was used, there was no aggregation. However, by increasing the strength of the eddy viscosity of the TKE scheme, they recovered aggregation. This finding suggested that the strength of the eddy viscosity played a crucial role in self-aggregation in RCE. They further investigated the role of momentum and moisture subgrid mixing and found that when moisture subgrid mixing was neglected, there was no aggregation. They pointed out that representation of horizontal entrainment of dry air, including relative contributions of explicit and parameterized mixing was one of the main factors to whether the convective plumes aggregated or not.

Wing and Emanuel (2014) performed a budget analysis of the variance of the density-weighted, vertically-integrated frozen moist static energy (FMSE) to identify the physical mechanisms associated with self-aggregation. When there is aggregation, the domain is separated into a dry and several moist regions. Since the moisture profile of the dry and moist regions are both significantly different from the mean moisture profile when there is aggregation, increased variance of FMSE can identify self-aggregation. Horizontal convergence feedback was found to be positive at the intermediate stage of the self-aggregation process, which was consistent with the circulation theory suggested by Bretherton et al. (2005) and Muller and Held (2012). Wing and Emanuel (2014) also found that air-sea disequilibrium feedback was strongly negative, and it was competing with strong positive

feedback from the surface wind. They found that while longwave radiative cooling created positive feedback for self-aggregation at the early stage, it also created slightly weaker negative feedback for self-aggregation at the intermediate and late stages.

Observations of Self-Aggregation

Since self-aggregation in RCE has become a popular topic, many researchers have been wondering if this is a "real" thing happening in nature or an artifact of models. Observational studies on aggregation in RCE have been summarized in Holloway et al. (2017). Some details on the observational studies are provided here. Tobin et al. (2012) performed an observational study of convective aggregation in RCE using geostationary satellite data. They found that in a more aggregated state, the free troposphere and, hence, the whole domain is drier. The outgoing longwave radiation (OLR) at the top of the atmosphere also increased in a more aggregated state likely because there are less high cloud in the domain. These are consistent with the findings from idealized RCE simulations in Bretherton et al. (2005). However, there were also some results from observational studies that were inconsistent with the results from idealized RCE simulations (Tobin et al., 2012, 2013). While both observation data and idealized simulations both agreed that the top of the atmosphere OLR increased in a more aggregated state, the net radiation between observational studies and idealized simulations were not consistent. The net radiation in observational studies was not sensitive to the state of aggregation. This was because there was also a decrease in reflected shortwave radiation in a more aggregated state in observational studies (Tobin et al., 2012, 2013). In idealized RCE simulations, there was a net loss in the top of the atmosphere radiation. The increase of low-level clouds in idealized RCE simulation did not change the amount of reflected shortwave radiation (Holloway and Woolnough, 2016).

2.1.2 Energy Spectrum

In this work, we investigate whether the -5/3 mesoscale kinetic energy spectrum develops in RCE and analyze the mechanisms that govern the energy at different length scales. The -5/3 kinetic energy spectrum has been reproduced in several idealized mesoscale simulations (Peng et al., 2014; Skamarock, 2004; Sun et al., 2017). Unlike other mesoscale systems, where baroclinic instability controls large scales, mesoscale energy in RCE is generated entirely by the heating from surface fluxes and radiative cooling. These processes are not necessarily restricted to large scales, and so the resulting spectral budget may be more complicated than a cascade from large to small scales.

In a turbulent inertial range, energy is transferred conservatively between scales with a constant spectral flux. In this framework, dimensional arguments yield the Kolmogorov spectrum with a -5/3 slope (Kolmogorov, 1941). Atmospheric measurements show a k_h^{-3} energy spectrum for synoptic scales in mid-latitudes and a shallower $k_h^{-5/3}$ energy spectrum in the mesoscale (Nastrom and Gage, 1985; Callies et al., 2014; Cho and Lindborg, 2001) in tropics and mid-latitudes, where k_h is the horizontal wavenumber. While there is a general agreement that the k_h^{-3} spectrum is due to quasi-geostrophic turbulence (Charney, 1971), there is no agreement on the mechanisms responsible for the $k_h^{-5/3}$ spectrum in the mesoscale. Proposed theories that attempted to explain the $k_h^{-5/3}$ spectrum fall into two categories: the direct energy cascade theory and inverse energy cascade theory (Lilly, 1983). The inverse cascade hypothesis is found to be unlikely at scales smaller than 100 km (Cho and Lindborg, 2001). Possible mechanisms for a downscale cascade include inertial-gravity waves (IGW) (VanZandt, 1982; Callies et al., 2016), quasigeostrophic turbulence (e.g. Tung and Orlando, 2003; Tulloch and Smith, 2009) and strongly stratified turbulence (Lindborg, 2006).

2.1.3 Energy Spectral Budget

Classical turbulence theories assume that there is no significant source or sink of kinetic energy in the inertial subrange between the forcing and dissipation scales. As a result, cascade theories of the mesoscale energy spectrum implicitly make this assumption. However, moist processes can energize the mesoscale by directly injecting energy at the mesoscale according to (Waite and Snyder, 2013). They investigated the effect of moisture on the mesoscale KE spectrum in a baroclinic wave. The buoyancy flux spectrum suggested that the energy generated by latent heat injected kinetic energy at the mesoscale.

Augier and Lindborg (2013) developed a formulation for spectral energy budget analysis to compare two hydrostatic global numerical weather forecasting models: the Atmospheric GCM for the Earth Simulator (AFES) and European Centre for Medium-Range Weather Forecasts (ECMWF) Integrated Forecast System (IFS). In their formulation, spherical harmonics functions are employed. The nonlinear transfer term was separated into horizontal and vertical contributions. The horizontal nonlinear transfer is conservative. As a result, the direction of the energy cascade can also be identified by this formulation. They found a strong downscale energy cascade in the mesoscale for the AFES model. However, AFES has low vertical resolution (Hamilton et al., 2008), which can affect the mesoscale spectrum (Waite, 2016).

Malardel and Wedi (2016) conducted a kinetic and available potential energy spectral analysis of the IFS model. In particular, the spectral analysis techniques developed by Augier and Lindborg (2013) were used to examine the role of physical parameterizations in the k^{-3} spectrum at the synoptic scale and $k^{-5/3}$ spectrum at the mesoscale. Malardel and Wedi (2016) found that KE and APE spectra and their spectral energy fluxes were significantly affected by physical parameterizations. For example, KE and APE spectra were smaller in adiabatic simulations than in the full physics simulations at all scales except at very large scales. The energy flux for the conversion from APE to KE was also significantly affected at different scales when the deep convection parameterization or vertical diffusion parameterization was disabled. The choice of physical parameterization could affect the energy cascade. As suggested by Malardel and Wedi (2016), if physical processes were not represented properly due to resolution and subgrid-scale parameterizations, the parameterized energy transfer would not be realistic.

Sun et al. (2017) conducted an energy spectral budget analysis of an idealized non-hydrostatic mesoscale convective system simulation. The $k^{-5/3}$ spectrum was found from the lower troposphere to the lower stratosphere. At small scales, buoyancy flux injected kinetic energy in the upper troposphere and the vertical flux divergence distributed energy in the vertical directions through convection and inertia gravity waves. Such results suggested that the mechanisms responsible for the spectrum could be three-dimensional. In other words, an inverse cascade was unlikely to be the main responsible mechanism in mesoscale convective systems. However, the simulations were short and far from equilibrium, and there were no surface fluxes. As a result, it is not clear how relevant this is to RCE over longer time scales.

We investigate the mechanisms and energy cascade in RCE simulations with and without self-aggregation by performing an analysis of the atmospheric energy spectrum and the spectral energy budget. By analyzing the spectral budget and comparing non-aggregated and aggregated simulations, we can understand the role of convection on the development of the kinetic energy spectrum and the spectral energy budget. The rest of this chapter is organized as follows. In section 2.2, we present the methodology and the details of the spectral budget. Results and discussion are presented in section 2.3. In section 2.3.1, an overview of the simulation is presented. In section 2.3.2, we discuss kinetic energy spectra and spectral budget. In section 2.3.3, we discuss nonlinear spectral energy flux. In section 2.3.4, we discuss compensated kinetic energy spectra. In section 2.3.5, we discuss the effect of rotation on kinetic energy spectra and spectral budget. Conclusions are given in section 2.4. The details on numerical dissipation are given in the appendix.

2.2 Methodology

2.2.1 Model

We use the Advanced Research Weather Research and Forecasting (WRF) model to perform all simulations (Skamarock et al., 2008). The fully compressible non-hydrostatic Euler equations are solved in WRF (Skamarock et al., 2008) with a third-order Runge-Kutta time-stepping scheme, a third-order advection scheme in the vertical, and a fifth-order advection scheme in the horizontal. Terrain following hydrostatic pressure is used as the vertical coordinate.

The setup of our simulations is modified from the radiative-convective equilibrium test case from WRF. The initial temperature and moisture profiles are from Rotunno and Emanuel (1987). The domain size is $L\ (x) \times L\ (y) \times H\ (z)$, where $L = 600$ km and $H = 25$ km. The horizontal grid spacing is $\Delta x = 4$ km, with 199 grid levels in the vertical. Horizontal resolution of O(km) is suitable to conduct a convective-permitting simulations (Tompkins and Semie, 2017, e.g.). The vertical level spacing is about 100 m from the ground to 15 km, above which the vertical resolution stretches to a level spacing of about 400 m at the top of the domain. Simulations are run for 77 days. Boundary conditions are periodic in x and y. In the top 5 km of the domain, Rayleigh damping with a damping coefficient of 0.003 s^{-1} is applied. There is no rotation, except for in one rotation test case, or imposed background wind.

A brief overview of parameterizations used will be given here. No planetary boundary layer (PBL) scheme for sub-grid boundary layer mixing is used, due to the grid resolution being in the grey zone between parameterized and fully resolved boundary layer turbulence. The sea surface temperature (SST) is set to 302 K, which is reasonable for a tropical area. Other RCE studies have performed simulations with similar SST (e.g. Colin et al., 2019; Tompkins and Semie, 2017). Revised MM5 Monin-Obukhov surface layer scheme (Jiménez et al., 2012) is used and it calculates the latent heat flux, sensible heat flux and momentum flux at the surface. RRTMG radiation scheme for longwave and shortwave radiative transfer is used and it is a radiative scheme that interactive with clouds. There is no diurnal cycle and the incoming solar radiation is set to 434.12 W/m^2, which corresponds to an effective zenith angle of 50.5 degrees (e.g. Holloway and Woolnough, 2016). We use the Thompson microphysics scheme (Thompson et al., 2008) and it represents the microphysics processes for cloud, water vapour, rain, ice, snow and graupel. The subgrid turbulence mixing scheme used in simulations presented is the 1.5 order turbulence kinetic energy (TKE) closure model (e.g. Skamarock et al., 2008).

2.2.2 Kinetic Energy Spectrum and Spectral Budget

The horizontal kinetic energy (HKE) per unit volume contributed by horizontal wave vector $\boldsymbol{k} = (k_x, k_y)$ at height z is

$$E_h(\boldsymbol{k}, z) = \frac{1}{2}\overline{\rho}(z)(\hat{u}(\boldsymbol{k}, z)^* \hat{u}(\boldsymbol{k}, z) + \hat{v}(\boldsymbol{k}, z)^* \hat{v}(\boldsymbol{k}, z)), \tag{2.1}$$

where hat represents Fourier coefficient and $*$ denotes complex conjugate. In order to investigate the role of vortices and gravity waves in the atmospheric kinetic energy spectrum, it is common to decompose the HKE into the horizontal rotational (RKE) and divergent kinetic energy (DKE) (e.g. Augier and Lindborg, 2013; Waite and Snyder, 2013). The horizontal kinetic energy is decomposed by Helmholtz decomposition:

$$E_h(\boldsymbol{k}, z) = RKE(\boldsymbol{k}, z) + DKE(\boldsymbol{k}, z), \tag{2.2}$$

$$RKE(\boldsymbol{k}, z) = \frac{1}{2}\overline{\rho}(z)\frac{\hat{\delta}^*\hat{\delta}}{k_h^2}, \tag{2.3}$$

$$DKE(\boldsymbol{k}, z) = \frac{1}{2}\overline{\rho}(z)\frac{\hat{\xi}^*\hat{\xi}}{k_h^2}, \tag{2.4}$$

where $\hat{(\cdot)}$ represents the Fourier coefficient of $(\cdot)$, $k_h = |\boldsymbol{k}|$ and

$$\xi = \frac{\partial u}{\partial x} + \frac{\partial v}{\partial y},$$

$$\delta = \frac{\partial v}{\partial x} - \frac{\partial u}{\partial y},$$

are the horizontal divergence and vertical vorticity of the horizontal velocity. RKE is often used to diagnose horizontal vortices, while DKE can identify energy from IGWs. DKE is significantly larger than RKE in the lower stratosphere, suggesting IGWs are important. In addition, RKE $\gtrsim$ DKE in the upper troposphere in many studies (e.g. Waite and Snyder, 2013; Peng et al., 2015b).

While WRF is a compressible model, acoustic modes are damped by the semi-implicit time stepping, and so the anelastic approximation is used in the spectral budget analysis as in Sun et al. (2017). The anelastic approximation is often employed to simplify the governing equations in the atmosphere due to the fact that density changes with height are more significant than the changes in the horizontal (e.g. Vallis, 2006). The anelastic approximation assumes that the density (ρ), pressure (p) and potential temperature (θ)

can be written as the sum of a hydrostatically balanced state, which is a function of height $\widetilde{(\cdot)}$, and a small perturbed state $(\cdot)'$:

$$\rho = \widetilde{\rho}(z) + \rho'(x, y, z, t), \tag{2.5}$$

$$p = \widetilde{p}(z) + p'(x, y, z, t), \tag{2.6}$$

$$\theta = \widetilde{\theta}(z) + \theta'(x, y, z, t). \tag{2.7}$$

In the atmosphere, the variation of density, pressure and potential temperature at a certain height is often small compared to the balanced state (e.g. Vallis, 2006), which is given by $|\rho'| \ll \widetilde{\rho}(z)$. In this approximation, the continuity equation (Vallis, 2006) takes the simpler form

$$\nabla \cdot (\widetilde{\rho}\, \boldsymbol{v}) = 0. \tag{2.8}$$

With the anelastic approximation, the momentum equations are written as

$$\frac{D\boldsymbol{v}}{Dt} = \hat{\boldsymbol{k}} g \frac{\theta'_v}{\widetilde{\theta}} - c_p \theta_v \boldsymbol{\nabla} \pi' + \frac{\partial \tau_{ij}}{\partial x_j}, \tag{2.9}$$

where $\boldsymbol{v} = (u, v, w) = (u_1, u_2, u_3)$ is the velocity vector in three dimension, ∇ is the three-dimensional gradient operator, θ is the potential temperature, θ_v is the virtual potential temperature, π is the Exner function (e.g. Sun et al., 2017), and τ_{ij} is the subgrid-scale stress tensor, which is a viscosity-like term for subgrid turbulence mixing modeling.

To understand the evolution of $E_h(\boldsymbol{k}, z)$, it is useful to consider its budget. This budget was developed by Augier and Lindborg (2013) on a spherical hydrostatic model, and modified by Peng et al. (2015a) and Sun et al. (2017) to a non-hydrostatic model with rectangular coordinates. The budget is derived by taking the Fourier transform of the momentum equations and dotting with the conjugate of the horizontal velocity vectors:

$$\frac{\partial E_h}{\partial t}(\boldsymbol{k}, z) = Re(A(\boldsymbol{k}, z) + P(\boldsymbol{k}, z) + D(\boldsymbol{k}, z)), \tag{2.10}$$

where

$$A(\boldsymbol{k}, z) = -\overline{\rho}(z) \hat{u_i}^* \mathcal{F}\left(u_j \frac{\partial}{\partial x_j} u_i\right), \tag{2.11}$$

$$P(\boldsymbol{k}, z) = -\overline{\rho}(z) \hat{u_i}^* \mathcal{F}\left(c_p \theta_v \frac{\partial}{\partial x_i} \pi'\right), \tag{2.12}$$

$$D(\boldsymbol{k}, z) = \overline{\rho}(z) \hat{u_i}^* \mathcal{F}\left(\frac{\partial}{\partial x_j}(\tau_{ij})\right), \tag{2.13}$$

where $\mathcal{F}(\cdot)$ represents the two-dimensional horizontal Fourier coefficient of $(\cdot)$ which is dependent on z, $A(\boldsymbol{k}, z)$ is the energy tendency from the nonlinear advection, $P(\boldsymbol{k}, z)$ is the energy tendency from the pressure term, and $D(\boldsymbol{k}, z)$ is the energy dissipation from subgrid turbulence mixing. Note that in some other studies, the dissipation is often ignored or calculated as a residual (e.g. Peng et al., 2015a). We calculate the effect of the dissipation explicitly in our study. In the analysis of the model energy spectrum, wavelengths less than $6\Delta x$ are often ignored due to the effect of the dissipation (e.g. Bryan et al., 2003). In global or regional climate simulations, $6\Delta x$ can be the length of a convective plume or even a convective system (e.g. Bryan et al., 2003; Bryan and Morrison, 2012). Dissipation is Δx-dependent and purely dissipative in eddy viscosity models. Because of the importance of dissipation, we calculate the dissipative term in the spectral budget explicitly.

The advective contribution to the spectral budget $A(\boldsymbol{k}, z)$ can be further broken down into the contribution from the conservative horizontal nonlinear transfer $T(\boldsymbol{k}, z)$, which corresponds to conservative transfers of energy between different scales at the same height, the sum over $\boldsymbol{k}$ of which at each height is zero; and a contribution to the divergence of vertical energy flux (e.g. Augier and Lindborg, 2013; Peng et al., 2015a; Sun et al., 2017):

$$A(\boldsymbol{k}, z) = -\overline{\rho}\hat{\boldsymbol{u}}^* \cdot \mathcal{F}\left(\boldsymbol{u} \cdot \nabla_h \boldsymbol{u} + \boldsymbol{u}\frac{\nabla_h \cdot \boldsymbol{u}}{2}\right) \tag{2.14}$$

$$- \frac{1}{2}\overline{\rho}\hat{\boldsymbol{u}}^* \cdot \mathcal{F}\left(w\frac{\partial \boldsymbol{u}}{\partial z}\right) + \frac{1}{2}\overline{\rho}\widehat{\frac{\partial \boldsymbol{u}}{\partial z}}^* \cdot \mathcal{F}(w\boldsymbol{u}) \tag{2.15}$$

$$- \frac{1}{2}\frac{\partial(\overline{\rho}\hat{\boldsymbol{u}}^* \cdot \mathcal{F}(w\boldsymbol{u}))}{\partial z}, \tag{2.16}$$

$$= T(\boldsymbol{k}, z) - \frac{1}{2}\frac{\partial(\overline{\rho}\hat{\boldsymbol{u}}^* \cdot \mathcal{F}(w\boldsymbol{u}))}{\partial z}, \tag{2.17}$$

where the sum of (2.14) and (2.15) can be defined as the horizontal nonlinear transfer $T(\boldsymbol{k}, z)$ and (2.16) is a part of the divergence of vertical energy flux and it is defined as

$$V_{adv}(\boldsymbol{k}, z) = -\frac{1}{2}\frac{\partial(\overline{\rho}\hat{\boldsymbol{u}}^* \cdot \mathcal{F}(w\boldsymbol{u}))}{\partial z}.$$

The pressure term $P(\boldsymbol{k}, z)$ can be decomposed into a contribution from the buoyancy flux and another contribution to the divergence of vertical energy flux (e.g. Augier and

Lindborg, 2013; Peng et al., 2015b; Sun et al., 2017).

$$P(\boldsymbol{k}, z) \approx -c_p \frac{\partial}{\partial z}(\overline{\rho}\overline{\theta}\hat{w}^*\hat{\pi}^{'}) \tag{2.18}$$

$$+ c_p \overline{\rho}\overline{\theta}\hat{w}^* \mathcal{F}\left(\frac{\partial \pi^{'}}{\partial z}\right), \tag{2.19}$$

$$= -c_p \frac{\partial}{\partial z}(\overline{\rho}\overline{\theta}\hat{w}^*\hat{\pi}^{'}) + B(\boldsymbol{k}, z), \tag{2.20}$$

where (2.19) is the buoyancy flux $B(\boldsymbol{k}, z)$. The vertical flux from (2.16) and (2.18) are collected to form the divergence of vertical energy flux $V(\boldsymbol{k}, z)$, which is given below.

In summary,

$$\frac{\partial E}{\partial t}(\boldsymbol{k}, z) = Re(T(\boldsymbol{k}, z) + B(\boldsymbol{k}, z) + V(\boldsymbol{k}, z) + D(\boldsymbol{k}, z)), \tag{2.21}$$

where

$$T(\boldsymbol{k}, z) = -\overline{\rho}\hat{\boldsymbol{u}}^* \cdot \mathcal{F}\left(\boldsymbol{u} \cdot \nabla_h \boldsymbol{u} + \boldsymbol{u}\frac{\nabla_h \cdot \boldsymbol{u}}{2}\right) \tag{2.22}$$

$$- \frac{1}{2}\overline{\rho}\hat{\boldsymbol{u}}^* \cdot \mathcal{F}\left(w\frac{\partial \boldsymbol{u}}{\partial z}\right) + \frac{1}{2}\overline{\rho}\widehat{\frac{\partial \boldsymbol{u}}{\partial z}}^* \cdot \mathcal{F}(w\boldsymbol{u}), \tag{2.23}$$

$$B(\boldsymbol{k}, z) = c_p \overline{\rho}\overline{\theta}\hat{w}^* \mathcal{F}\left(\frac{\partial \pi^{'}}{\partial z}\right), \tag{2.24}$$

$$V(\boldsymbol{k}, z) = -\frac{1}{2}\frac{\partial(\overline{\rho}\hat{\boldsymbol{u}}^* \cdot \mathcal{F}(w\boldsymbol{u}))}{\partial z} - c_p \frac{\partial}{\partial z}(\overline{\rho}\overline{\theta}\hat{w}^*\hat{\pi}^{'}), \tag{2.25}$$

$$D(\boldsymbol{k}, z) = -\overline{\rho}\hat{u_i}^* \mathcal{F}\left(\frac{\partial}{\partial x_j}\tau_{ij}\right). \tag{2.26}$$

Due to computational limitations, it is not possible to resolve the smallest eddies directly. As a result, Smagorinsky (1963) suggested the eddy viscosity model which parameterizes the subgrid eddies with a viscosity-like term. The subgrid stress tensor τ_{ij} is defined as

$$\tau_{ij} = K_{h,v} D_{ij}, \tag{2.27}$$

where D_{ij} is the deformation tensor, where $i,j = 1, 2, 3$ and K_h is the eddy viscosity for $i, j = 1, 2$ and K_v is the eddy viscosity for i or $j = 3$. In the TKE closure model, K is computed using the evolution of the subgrid turbulence kinetic energy:

$$K_{h,v} = C_k e^{1/2} \Delta_{h,v}, \tag{2.28}$$

where C_k is a constant and Δ_h is the horizontal grid spacing and Δ_v is the vertical grid spacing. e is the subgrid turbulence kinetic energy and its evolution is predicted with a model equation (e.g. Wyngaard, 2010).

In this study, we will also consider the effect of numerical dissipation. WRF uses a third-order upwind advection scheme in the vertical, and a fifth-order upwind advection scheme in the horizontal (Skamarock et al., 2008), both of which have weak dissipation. The calculation of the numerical dissipation is described in the appendix.

All two-dimensional energy and budget spectra on the $k_x - k_y$ plane are transformed to one-dimensional spectra on k_h as in Waite and Snyder (2009):

$$E(k_h)\Delta k = \sum_{k_h - 0.5\Delta k \leq |\boldsymbol{k}| \leq k_h + 0.5\Delta k} E(\boldsymbol{k}), \tag{2.29}$$

where k_h is the horizontal wavenumber, $\Delta k = 2\pi/L$ is the wavenumber spacing, and similarly for spectra of $T(k_h, z)$, $B(k_h, z)$, $V(k_h, z)$, and $D(k_h, z)$. Unless otherwise specified, $D(k_h, z)$ includes both eddy dissipation and numerical dissipation.

The nonlinear spectral energy flux $\Pi(k_h, z)$ is defined as (e.g. Peng et al., 2015b)

$$\Pi(k_h, z) = \Delta k \sum_{k \geq k_h} Re(T(k, z)), \tag{2.30}$$

where $\Delta k = 2\pi/L$. $\Pi(k_h, z)$ is the rate at which kinetic energy is transferred downscale past wavenumber k_h at height z. Positive Π implies forward energy transfer and negative Π suggests inverse energy transfer. A downscale cascade is characterized by a wide range of constant positive $\Pi(k_h, z)$.

When computing energy spectra and the energy spectral budget terms, fields are interpolated from WRF model levels to a constant height at every 50 m, which is about half of the vertical resolution of the simulation from the lower troposphere to the lower stratosphere, as in Sun et al. (2017). Nonlinear terms are computed after interpolating to higher horizontal resolution to eliminate aliasing (e.g. Durran, 2010). This approach ensures that $T(\boldsymbol{k}, z)$ is indeed conservative. Horizontal derivatives are computed with Fourier transform, and the vertical derivatives are computed with the second-order central finite difference scheme. All energy spectra presented are averaged in both time (final 42 days of simulation) and height. In the following discussion, the upper troposphere is defined as the region between 6-10 km in height and the lower stratosphere is defined as the region between 15.5-17 km in height.

Two main simulations will be discussed: one with and one without aggregation. Unless otherwise specified, we will focus our following discussion on the two simulations without

rotation. Note that whether or not aggregation occurs is strongly affected by the subgrid turbulence scheme. It is very hard to get aggregation if the standard TKE subgrid turbulence scheme is used. This can be understood by the fact that the subgrid turbulence parameterization may have an effect on other parameterizations, which creates a feedback process to favour the creation of self-aggregation (Tompkins and Semie, 2017). The increase in eddy viscosity may result in less resolved entrainment and more in parameterized turbulence mixing, which may lead to stronger convection due to the interaction between microphysics, radiative transfer and dynam ics (Tompkins and Semie, 2017). Inspired by Tompkins and Semie (2017), we have multiplied the TKE coefficient (C_k) by two in the aggregated simulation. In the following discussions, we will call the simulation with the default TKE coefficient ($C_k = 0.15$) the non-aggregated simulation and the simulation the larger TKE coefficient ($C_k = 0.3$) the aggregated simulation. While the fact that aggregation requires strong dissipation may be a numerical artifact, given the importance of aggregation in the literature, these two simulations allow us to compare aggregated and non-aggregated simulations. The configuration of the non-aggregated and aggregated simulations are otherwise identical. We will discuss the evolution, horizontal kinetic energy spectra and the spectral budgets of the aggregated and non-aggregated simulations in this section. Note that features with length scale of less than $6\Delta x$ ($k_h/\Delta k > 25$) are often considered as not well-resolved (e.g. Sun et al., 2017; Menchaca and Durran, 2019). As a result, findings from scales smaller than $6\Delta x$ (24 km) will be interpreted with care. Not surprisingly, we find that the energy budget at these marginally resolved scales is dominated by dissipation. An additional shorter simulation with rotation added will be presented to briefly demonstrate the effect of rotation on the kinetic energy spectrum and the spectral energy budget. The detail of the rotation simulation will be given in the corresponding subsection.

2.3 Results and Discussion

2.3.1 Overview of the Simulations

To identify and quantify aggregation, we visualize the evolution of the outgoing longwave radiation at top of the atmosphere (TOA OLR) in Fig. 2.1. In the non-aggregated simulation (Figs. 2.1a-h), the system reaches approximate equilibrium at about 320 hours. After the simulation reaches equilibrium, the convective cores are randomly distributed over the whole domain and remain so throughout the remaining time of the non-aggregated simulation (Figs. 2.1a-h). Note that the convective system develops some large-scale struc-

ture at late times (e.g. Figs. 2.1e-h), but they are very different from the large isolated convective structure that develops in the aggregated case. In the aggregated simulation (Figs. 2.1i-p), the convective cores are randomly distributed in the domain at early times. The convective cores aggregate significantly after 160 hours, and the simulation reaches an aggregated state, with one large cloud region surrounded by a dry region, after about 480 hours (Figs. 2.1k-p).

We find that aggregation changes mean profiles, which agrees with findings from other studies (e.g. Wing et al., 2017). In the non-aggregated simulation, there are no significant changes to the water vapour mixing ratio profile throughout the simulation (Fig. 2.2a). In contrast, the lower troposphere in the aggregated simulation dries as the convective system reaches an aggregated state (Fig. 2.3a). The drying in the troposphere in the aggregated simulation has also been reported in other studies (e.g. Bretherton et al., 2005; Wing and Cronin, 2016), and is likely due to precipitation (Tompkins and Semie, 2017, e.g.). The vertical profile of the cloud water plus cloud ice mixing ratio changes throughout the simulation for non-aggregated simulation (Fig. 2.2b). On the other hand, there is a significant increase in cloud condensate (cloud water plus cloud ice) over time in the lower troposphere of the aggregated simulation (Fig. 2.3b), which is consistent with the findings from other studies such as Wing and Cronin (2016). Note that while Wing and Cronin (2016) found that there was a reduction in cloud condensate in the mid-troposphere with aggregation, there is no obvious trend of increase or decrease in mid-troposphere liquid condensate in our study. The cloud top height of the aggregated simulation is slightly lower than the cloud top height of the non-aggregated simulation (Fig. 2.2b and 2.3b).

The variance of frozen moist static energy (e.g. Wing and Emanuel, 2014; Wing et al., 2017) or OLR (e.g. Muller and Held, 2012) can be employed to quantify aggregation. We will use the variance of frozen moist static energy to quantify aggregation. As we can see in Fig. 2.2(d) and 2.3(d), the variance of FMSE in the aggregated simulation is significantly larger than the variance in the non-aggregated simulation. A larger variance of FMSE suggests the convective system is more aggregated in line with the findings above. According to the variance of FMSE time series, the non-aggregated simulation reaches a stable state at about 300 hours (Fig. 2.2d) as found above. After that, we can see that the variance of FMSE oscillates around the same level throughout the remaining simulation time and increases slightly at around 800 hours. After it reaches the peak at about 950 hours, it drops significantly from 950 hours to 1600 hours. The fact that the variance of FMSE oscillates from 300 to 800 hours suggests that the convective system aggregates and disaggregates slightly even after it reaches its equilibrium state. Similarly, the convective system in the aggregated simulation reaches its most aggregated state at about 450 hours, then it disaggregates slightly. After the drop at 450 hours, the variance of the FMSE

oscillates. The oscillation in variance of FMSE suggests that the convective system in the aggregated also aggregates and disaggregates throughout the simulation. Overall, while there are some significant variations in the FMSE time series in Fig. 2.2(d), the overall magnitude of the FMSE variance is still much smaller than in the aggregated case in Fig. 2.3(d). The different OLR structures in Fig. 2.1, and the different FMSE variance magnitudes in Figs. 2.2 and 2.3, support the identification of these cases as non-aggregated and aggregated.

2.3.2 Kinetic Energy Spectra and Budget

In this section, we will discuss the difference in the horizontal kinetic energy spectrum and spectral budget of the aggregated and non-aggregated simulation in the upper troposphere. After that, we will discuss the difference in the lower stratosphere.

Upper Troposphere

The horizontal kinetic energy spectrum for the non-aggregated simulation in the upper troposphere is much shallower than the -5/3 spectrum (Fig. 2.4a). By contrast, the horizontal kinetic energy spectrum for the aggregated simulation in the upper troposphere is steeper than the non-aggregated case and closer to -5/3 (Fig. 2.4b). The fact that the horizontal kinetic energy spectrum is more energetic at scales of O(100 km) in the aggregated simulation is consistent with the size of the aggregated convective cores (Fig. 2.1). The convective core in the aggregated simulation aggregates and forms a large convective system of a few hundred km in size, which is not seen in the non-aggregated simulation.

Horizontal kinetic energy equals the sum of divergent kinetic energy and rotational kinetic energy. In the non-aggregated simulation, RKE is similar to DKE over most scales in the upper troposphere, with the DKE spectrum marginally larger than the RKE spectrum for $k_h/\Delta k < 40$ (Fig. 2.4a). In the aggregated simulation, the DKE $\gtrsim$ RKE for $k_h/\Delta k < 30$ (Fig. 2.4b). In other studies such as Waite and Snyder (2013) and Peng et al. (2015b), it was found that RKE $\gtrsim$ DKE in the upper troposphere, while DKE dominates in our simulations. The difference is likely due to the fact that their simulations were driven by large-scale vortices and rotation, while our non-aggregated and aggregated simulations are driven by surface fluxes and convection in a non-rotating environment. This conclusion is confirmed by the rotation simulation presented in section 2.3.5.

The tendency of the horizontal kinetic energy spectrum can be decomposed into the nonlinear transfer $T(k_h)$, the vertical energy flux $V(k_h)$, the buoyancy flux $B(k_h)$, and

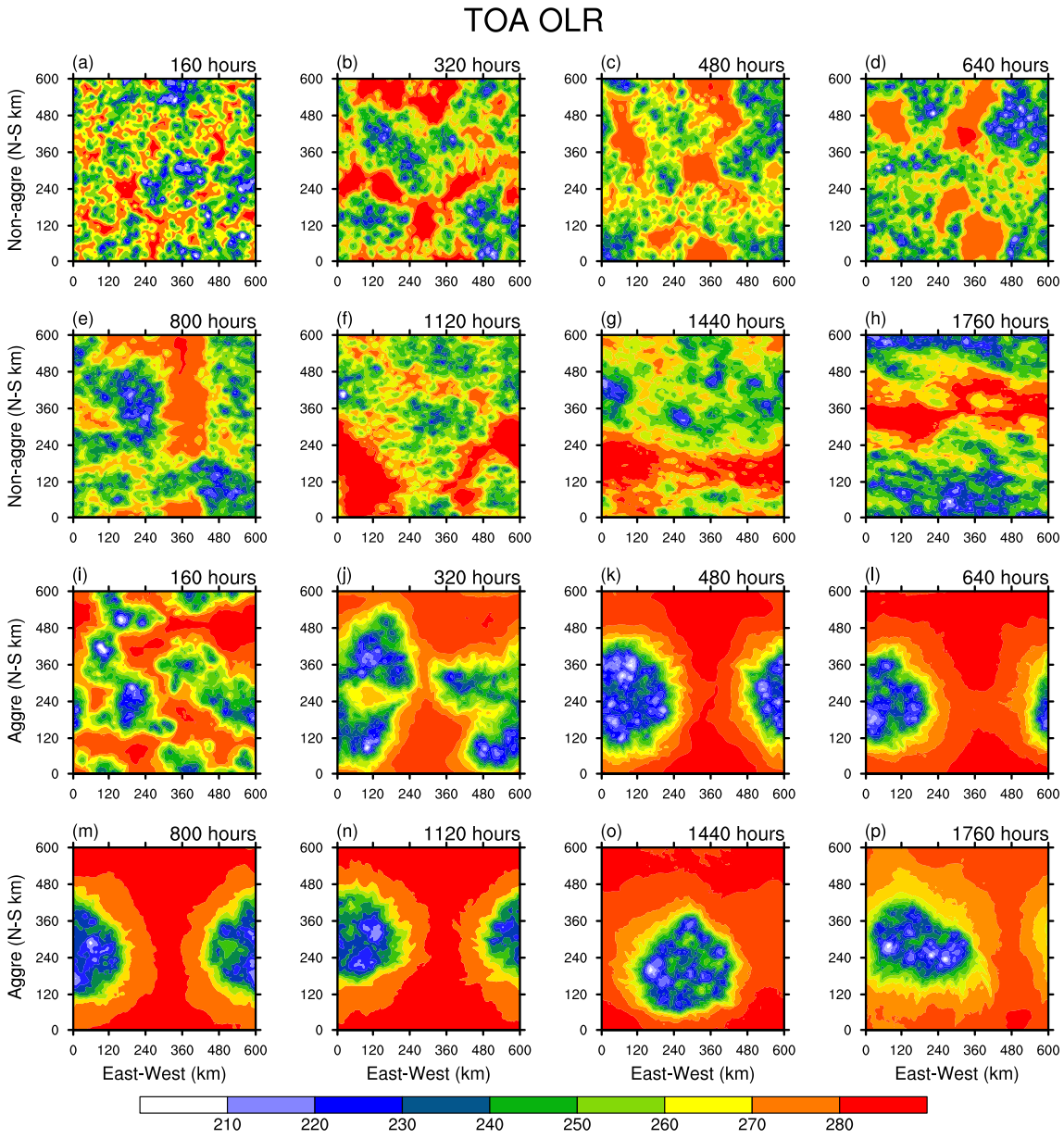


Figure 2.1: The outgoing longwave radiation (W/m^2) at top of the atmosphere (TOA OLR) for the non-aggregated simulation at $t =$ (a) 160 hours, (b) 320 hours, (c) 480 hours, (d) 640 hours, (e) 800 hours, (f) 1120 hours, (g) 1440 hours, and (h) 1760 hours, and for the aggregated simulation at $t =$ (i) 160 hours, (j) 320 hours, (k) 480 hours, (l) 640 hours, (m) 800 hours, (n) 1120 hours, (o) 1440 hours, and (p) 1760 hours.

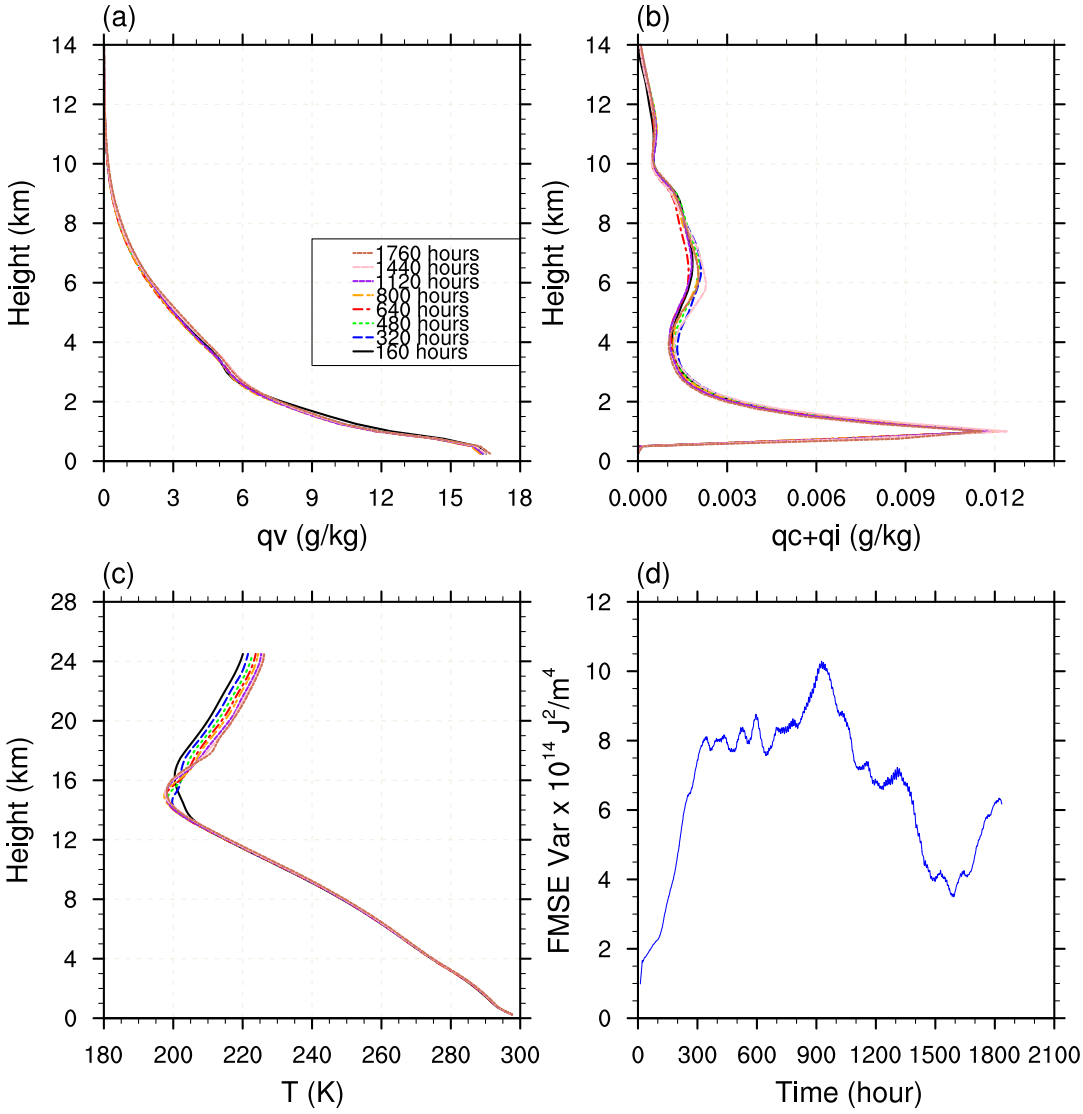


Figure 2.2: Vertical profiles of (a) water vapor mixing ratio, (b) cloud water plus cloud ice mixing ratio, and (c) temperature at $t = 160$ hours (black), 320 hours (blue), 480 hours (green), 640 hours (red), 800 hours (orange), 1120 hours (purple), 1440 hours (light pink), and 1760 hours (dark pink), and (d) the time series of the variance of vertically-integrated frozen moist static energy (FMSE) for the non-aggregated simulation. The variance of vertically-integrated FMSE is smoothed with a 24-hour moving average.

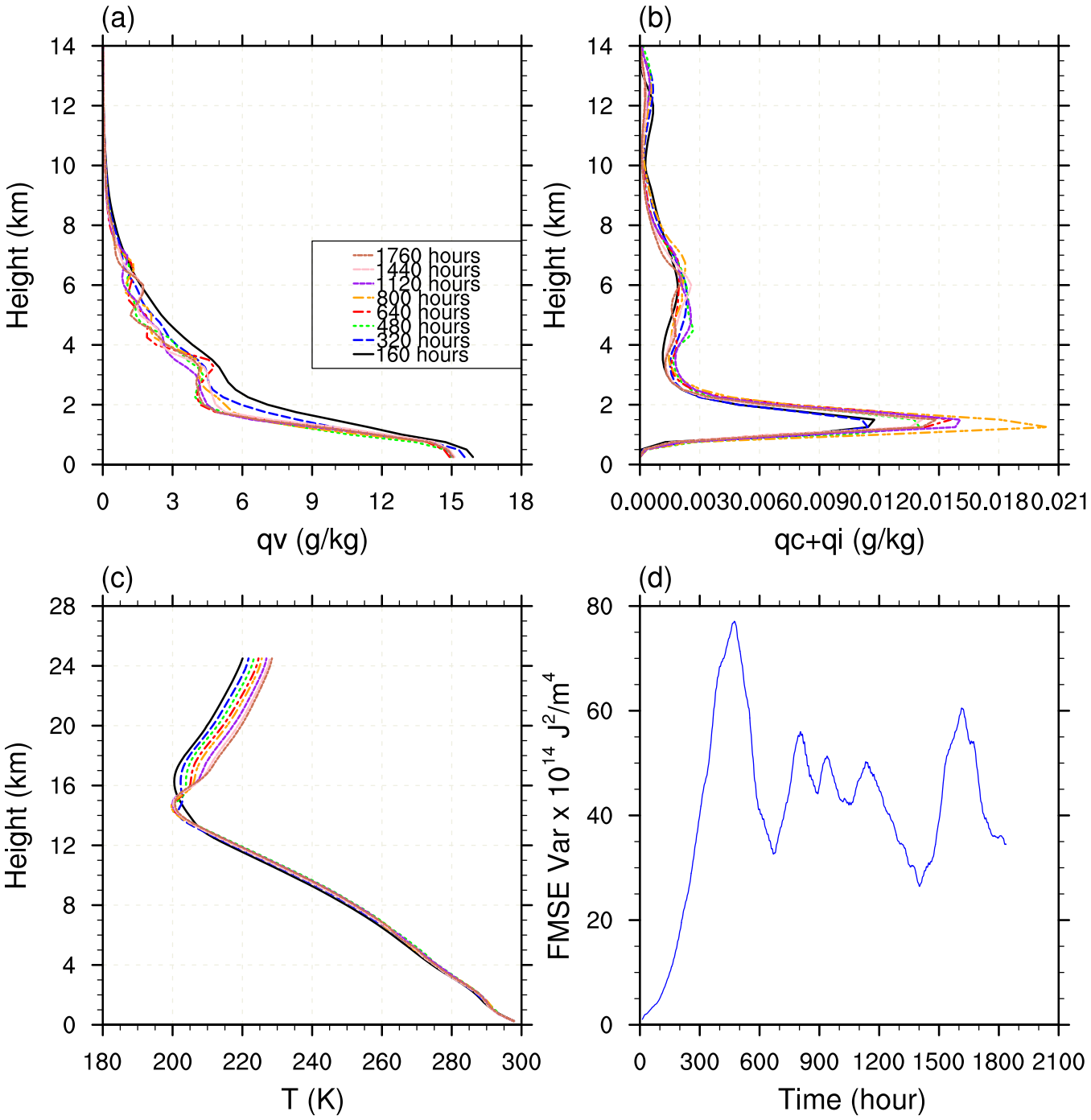


Figure 2.3: As in Fig. 2.2, but for the aggregated simulation.

the dissipation $D(k_h)$. In the upper troposphere, the non-aggregated simulation gains kinetic energy from the buoyancy flux term and loses energy from vertical energy flux and dissipation (Fig. 2.4c). The energy gain from the buoyancy flux and energy loss from the vertical energy flux is approximately balanced for $k_h/\Delta k < 30$ (wavelengths larger than 20 km). Moist processes energize the mesoscale by directly injecting energy at the mesoscale as in Waite and Snyder (2013). Convection adds latent heating and potential energy, some of which is converted to KE by the buoyancy flux. Hence, the buoyancy flux injects kinetic energy to the flow. Most of this kinetic energy is removed from the upper troposphere by vertical energy fluxes. The energy loss from the vertical energy flux is likely associated with the upward-propagating gravity waves. At smaller scales, the energy gain from buoyancy flux is mainly balanced by the loss of energy from dissipation at $k_h/\Delta k > 30$, which corresponds to wavelength of 20 km or less. The energy gain from buoyancy flux and the energy loss from dissipation both peak at about $k_h/\Delta k = 75$, which corresponds to a wavelength of $2\Delta x$. Recall that scales smaller than $6\Delta x$, or $k_h/\Delta k > 25$, are only marginally resolved. Kinetic energy from buoyancy flux is mainly generated at the smallest scales in the non-aggregated simulation. At all scales, the nonlinear transfer term is weak compared to the other terms in the budget. Note that the transfer term is conservative, so the sum of the transfer term should be zero. We can see that there is a positive contribution for the transfer term for $k_h/\Delta k > 20$, which suggests that there is a negative contribution from $k_h/\Delta k < 20$. This means energy transfer from large scale to small scales, which corresponds to downscale energy transfer.

The terms in the spectral budget for the aggregated simulation in the upper troposphere are weaker than the terms for the non-aggregated simulation (Fig. 2.4d). Unlike the non-aggregated simulation, the energy gain from the buoyancy flux is not mainly balanced by the loss of energy from the vertical energy flux for $k_h/\Delta k < 3$ in the aggregated simulation; rather, it is balanced by the loss of energy from the transfer term and the vertical energy flux. Note that $k_h/\Delta k < 3$ corresponds to length scales larger than 200 km, which is approximately the size of the convective core in the aggregated simulation. The energy gain from the buoyancy flux is balanced by the energy loss in the vertical energy flux at smaller scales in the aggregated simulation for $3 < k_h/\Delta k < 30$. For $k_h/\Delta k > 30$, there is energy gain from the vertical energy flux for the aggregated simulation, which is different from the non-aggregated simulation; while there is still a positive contribution from the buoyancy flux at these scales, it is not the dominant term. Note that scales smaller than $6\Delta x$ ($k_h/\Delta k > 25$) are not well-resolved. The positive contributions from the vertical energy flux, transfer and buoyancy flux are balanced by the dissipation. Similar to the non-aggregated simulation, there is a positive contribution for the transfer term at large k_h, which again implies that there is downscale energy transfer. Nevertheless,

since the transfer term contributes a relatively small part to the overall spectral budget, the spectrum does not appear to result from a turbulent cascade; rather, it is due to a balance between forcing by buoyancy flux and removal by vertical energy flux. The fact that the kinetic energy spectrum of the aggregated simulation is steeper than that in the non-aggregated case, and closer to the -5/3 spectrum, may be due to the fact that B, which adds kinetic energy, has a much broader spectrum in the aggregated simulation than in the non-aggregated simulation, where is it more dominated by small scales. Notice that the buoyancy flux and vertical energy flux divergence terms peak at a smaller wavelength in the non-aggregated simulation than in the aggregated simulation. This is reasonable because of convective core in the aggregated simulation corresponds to a larger wavelength than the convective core in the non-aggregated simulation. The fact that there is a change in sign in the vertical energy flux term at small scales in the upper troposphere for the aggregated simulation (Fig. 2.4d) is different from what was found in Sun et al. (2017), in which buoyancy flux was positive and vertical energy flux was negative in the upper troposphere at all wavelength. Note that the peak of all the terms in the spectral budget in the upper troposphere are at $k_h/\Delta k = 75$ for both simulations, which suggests that, as expected, $\Delta x = 4$ km may not be sufficient to fully resolve small-scale convection. Overall, energy is generated in the upper troposphere by buoyancy flux from moist convection and this energy is transferred away from the upper troposphere by vertical flux, e.g. of vertically propagating gravity waves.

Fig. 2.6(a) and Fig. 2.6(c) show the sum of the computed budget terms along with the tendency of the horizontal kinetic energy spectrum. The budget is approximately balanced for the well-resolved wavenumbers $k_h/\Delta k < 25$ in both the aggregated and non-aggregated. Note that features with length scale of less than $6\Delta x$ ($k_h/\Delta k > 25$) are often considered as not well-resolved and we should treat the result in the under-resolved range with care. Even at large k_h, the residual is less than 13% of the maximum terms in the budget, and is likely due to additional model damping terms and error.

Lower Stratosphere

In the lower stratosphere, the non-aggregated horizontal kinetic energy spectrum is again shallower than -5/3 (Fig. 2.5a). The horizontal kinetic energy spectrum for the non-aggregated simulation is less energetic than the spectrum from the aggregated simulation (Fig. 2.5b), which resembles the -5/3 spectrum for $4 < k_h/\Delta k < 20$ (wavelength between 30 km to 150 km). The divergent kinetic energy dominates the horizontal kinetic energy at all wavenumbers in both the non-aggregated and aggregated simulations, as reported in other studies (e.g. Menchaca and Durran, 2019). In Menchaca and Durran (2019) Fig. 6(b), we

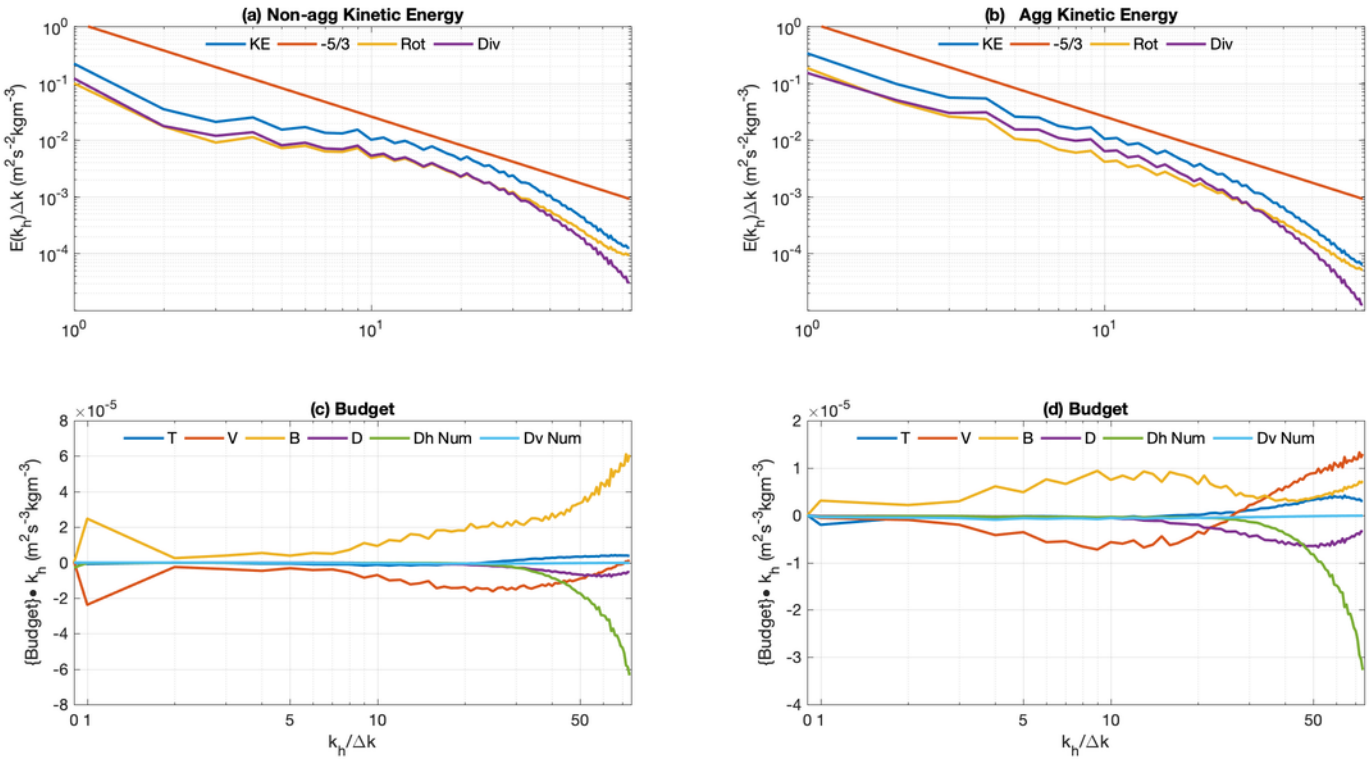


Figure 2.4: The horizontal kinetic energy spectrum (blue), rotational kinetic energy spectrum (yellow), and divergent kinetic energy spectrum (purple) in the upper troposphere (6-10 km) for (a) the non-aggregated simulation and (b) the aggregated simulation; and the spectral budget, including horizontal nonlinear energy transfer (blue), buoyancy flux (yellow), vertical energy flux divergence (red), dissipation from the subgrid mixing scheme (purple), and numerical dissipation (green), in the upper troposphere for (c) the non-aggregated simulation and (d) aggregated simulation. All spectra are averaged in the vertical and in time from 841 to 1848 hours. Budget spectra are multiplied by k_h, for all k_h except for $k_h = 0$, to preserve area on semi-log plots. Note that $k_h = 0$ is shown in Figs. c-d.

can see that the DKE dominated the horizontal kinetic energy spectrum from wavelength of 60 km to 180 km and the RKE dominated the horizontal kinetic energy spectrum in the larger scales. The domination of the DKE in all wavelength in our study is likely due to the fact that there is no rotation in our non-aggregated and aggregated simulations, which is confirmed by the simulation with rotation (see section 2.3.5). Both the horizontal kinetic energy spectra from the aggregated and non-aggregated steepen for $k_h/\Delta k > 30$. The steepening of the spectrum at wavelengths smaller than $6\Delta x$ has also been found in other studies (e.g. Peng et al., 2015a; Sun et al., 2017; Menchaca and Durran, 2019) and is due to numerical dissipation and the subgrid turbulence scheme.

The spectral budgets for both the aggregated and non-aggregated simulations in the lower stratosphere are similar in overall shape, but different in magnitude (Fig. 2.5c and d). The terms of the spectral budget from the aggregated simulation are about an order of magnitude smaller than those from the non-aggregated simulation. For both the aggregated and the non-aggregated simulation, the vertical energy flux is the main source of energy gain. The transfer and buoyancy flux removes kinetic energy at most length scales, except for the horizontal mean flow at $k_h = 0$. Similarly to what was found in the upper troposphere, the aggregated simulation produces a steeper KE spectrum closer to -5/3 at larger scales because V, which adds kinetic energy, has a much broader than in the non-aggregated simulation, which are more dominated by smaller scales. The dissipation removes energy at a rate that is about half of the transfer term for both simulations. The energy gain from the vertical energy flux is removed by the transfer term, the buoyancy flux, and the dissipation, similar to what was found in Sun et al. (2017). Sun et al. (2017) found that a significant amount of kinetic energy was injected by the vertical energy flux in the lower stratosphere and that energy was removed by the transfer term, the buoyancy flux and the dissipation. Also note that in Menchaca and Durran (2019), while the vertical energy flux injected energy at wavelengths from 50 to 180 km, it also removed energy at large scales of 900 km.

While the transfer term is not significant in the upper troposphere, it is more important in the lower stratosphere. Since the transfer term is conservative, the loss of energy from $k_h/\Delta k > 1$ means that there is an energy gain at $k_h/\Delta k \leq 1$. In other words, there is an upscale energy transfer in the lower stratosphere for both the aggregated and non-aggregated simulations. In particular, most of the upscale transfer goes into the mean flow ($k_h = 0$). The dissipation is removing energy at small scales in both simulations, which is consistent with other studies such as Sun et al. (2017). Overall in the lower stratosphere, the kinetic energy is obtained by gravity waves from the upper troposphere, and this energy input is balanced by the upscale transfer of energy and loss of energy to potential energy.

The sum of all the terms in the spectral budget matches relatively well with the tendency

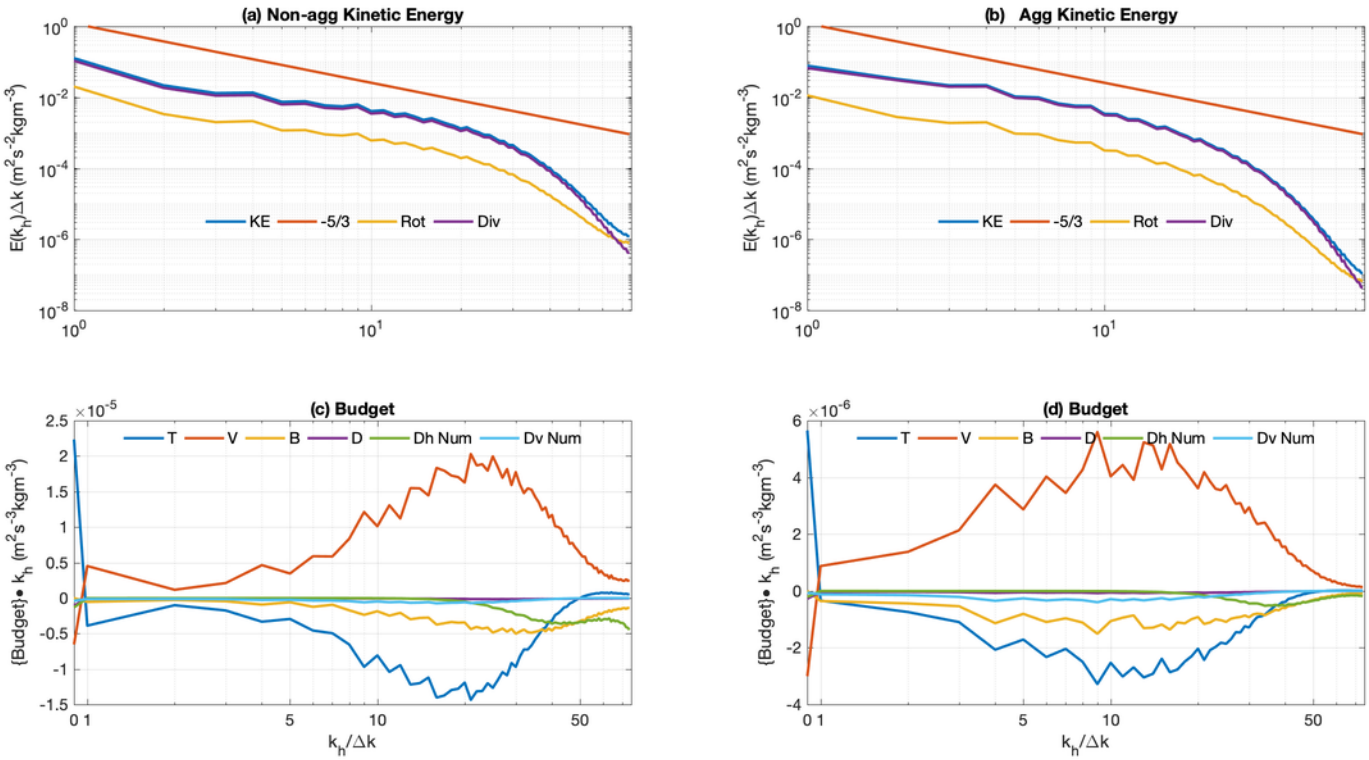


Figure 2.5: As in Fig. 2.4, but in the lower stratosphere (15.5-17 km).

of the horizontal kinetic energy. The difference between the sum of all the terms and the tendency is less than 9% of the maximum of all the terms for both the aggregated simulation and the non-aggregated simulation (Fig. 2.6b and Fig. 2.6d). Be mindful that features with $k_h/\Delta k > 25$ are often considered not well-resolved.

2.3.3 Nonlinear Spectral Energy Flux

In the above discussion of the nonlinear transfer, we see that the direction of energy transfer can be determined by the shape of the transfer term. A more systematic way of determining the direction of energy transfer is to look at the nonlinear spectral energy flux. The nonlinear spectral energy flux is defined in (2.30). If the nonlinear spectral energy flux is positive (negative), it means that there is direct, downscale (inverse, upscale) energy transfer.

For the non-aggregated simulation, direct energy transfer or weakly inverse energy

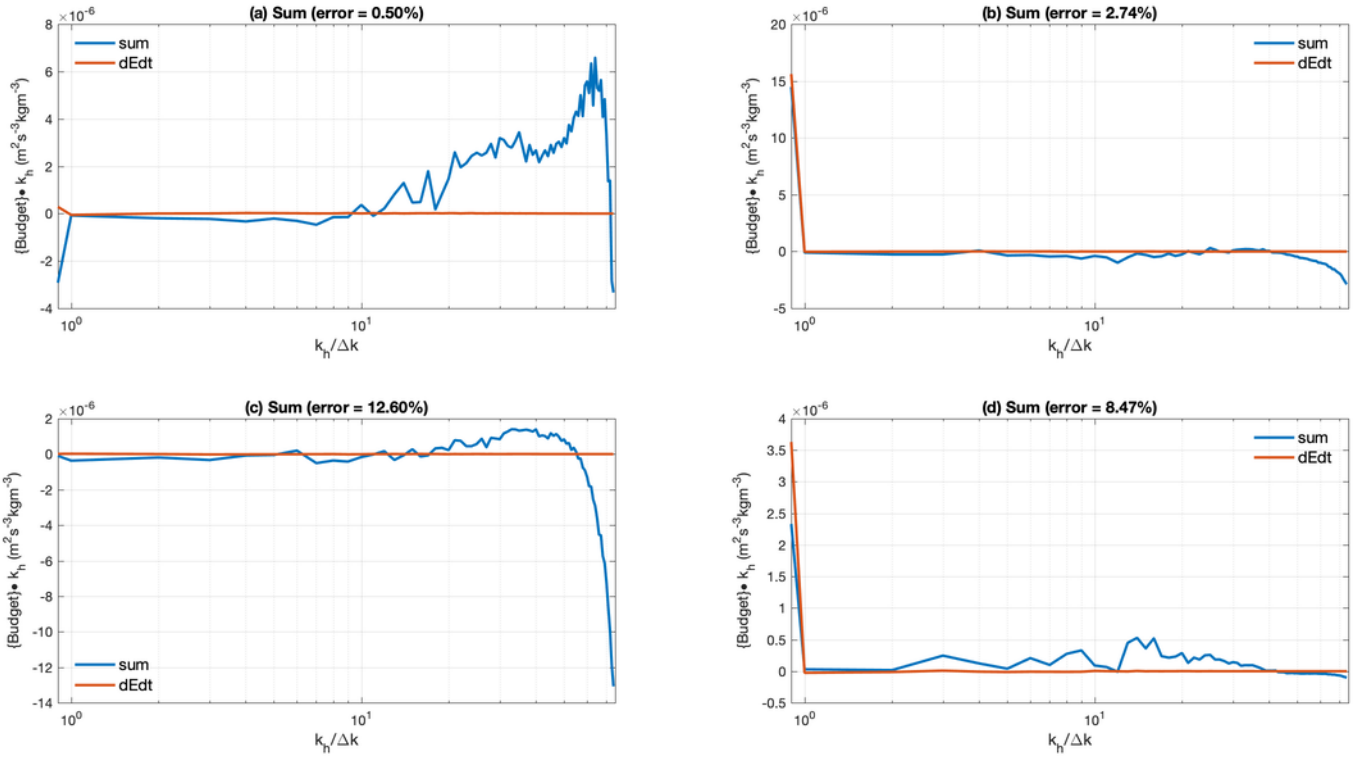


Figure 2.6: The rate of change of kinetic energy spectrum (dE/dt) is compared to the sum of the budget for the non-aggregated simulation (a) in the upper troposphere and (b) in the lower stratosphere, and for the aggregated simulation (c) in the upper troposphere and (d) in the lower stratosphere. The error is the ratio between the absolute value of the difference between the sum of the budget and dE/dt and the maximum of the absolute value of all the terms in the budget.

transfer can be found in the upper troposphere at all scales (Fig. 2.7). By contrast, at heights above 11 km, inverse energy transfer happens at almost all scales (Fig. 2.7) for the non-aggregated simulation, except for some direct energy transfer at heights from 14 to 15 km.

Similarly, for the aggregated simulation, we can see that at heights from 6 to 10 km (upper troposphere), there is direct energy transfer at $k_h/\Delta k > 2$ (Fig. 2.8). At a height above 12.5 km, inverse energy transfer dominates at $k_h/\Delta k = 2 - 30$ (Fig. 2.8). A direct energy cascade has also been reported in Augier and Lindborg (2013) and Peng et al. (2015b). Peng et al. (2015b) found that there was a direct energy cascade for scale less than 2000 km in a baroclinic wave in the upper troposphere.

Note that the sum of $T(k_h)$ has to be zero. The fact that we see $T(k_h > 0) < 0$ at most scales in the lower stratosphere for both simulations suggests that $T(0)$ has to be larger than zero, which is also confirmed by the budgets in Fig. 2.5. In fact, $k_h = 0$ is the only wavenumber at which $T(k_h)$ is significantly larger than zero. As a result, the upscale transfer in the lower stratosphere corresponds to transfer directly into the horizontal mean flow with $k_h = 0$, rather than a turbulent inverse cascade into eddies of large but finite scales, as in two-dimensional and quasi-geostrophic turbulence.

An inverse cascade in the lower stratosphere has also been reported by Peng et al. (2015a), Sun et al. (2017) and Menchaca and Durran (2019). Sun et al. (2017) found energy transferred out of small convective scales to larger scales, but it is not clear whether it is going into their mean flow or not. Unlike our transfer, transfers in Peng et al. (2015a) and Menchaca and Durran (2019) are mainly into small non-zero k_h. Notably, both of these simulations had rotation. Peng et al. (2015a) found inverse transfer from 200 km to 3000 km and Menchaca and Durran (2019) found that inverse cascade can exist from 90 km to 1500 km in their two mountain simulations. The inverse cascade in Menchaca and Durran (2019) occurred with flow over mountains, in which a significant amount of gravity waves were generated in the mesoscale. The fact that the inverse cascade was associated to gravity waves in their finding is similar to ours. As suggested by the vertical energy flux in our budgets (Fig. 2.5c-d) from the lower stratosphere, our lower stratospheres are dominated by waves as well. Note that in their simulation with no mountains, there was forward cascade instead of inverse cascade.

Inspired by the Eliassen-Palm (EP) flux discussion in Menchaca and Durran (2019), we would like to relate the transfer term at $k_h = 0$ to the rate of change of the mean-flow

kinetic energy, which is given by the sum of the following two equations:

$$\frac{\overline{\rho}}{2}\frac{\partial \overline{u}^2}{\partial t} = -\overline{u}\frac{\partial \overline{\rho}\,\overline{u'w'}}{\partial z} - \overline{u}\frac{\partial \overline{\rho}\,\overline{u}\,\overline{w}}{\partial z}, \tag{2.31}$$

$$\frac{\overline{\rho}}{2}\frac{\partial \overline{v}^2}{\partial t} = -\overline{v}\frac{\partial \overline{\rho}\,\overline{v'w'}}{\partial z} - \overline{v}\frac{\partial \overline{\rho}\,\overline{v}\,\overline{w}}{\partial z}, \tag{2.32}$$

where $\overline{(\cdot)}$ represents the horizontal average and $(\cdot)'$ represents the perturbed state from the horizontal average. The first term on the right is the contribution from eddies or the EP flux and the second term on the right is the contribution from the mean flow. Note that the equations above are neglecting dissipation because we are interested in the wave-mean-flow interaction and the mean flow interaction here.

The horizontal mean-flow kinetic energy also can be expressed using the advection terms in the spectral budget at $k_h = 0$, which can be further decomposed into the contribution from the transfer term and from part of the vertical flux term:

$$\frac{\overline{\rho}}{2}\frac{\partial \overline{u}^2}{\partial t} + \frac{\overline{\rho}}{2}\frac{\partial \overline{v}^2}{\partial t} = T(0) + V_{adv}(0) = \left(-\overline{u}\frac{\partial \overline{\rho}\,\overline{u'w'}}{\partial z} - \overline{v}\frac{\partial \overline{\rho}\,\overline{v'w'}}{\partial z}\right) + \left(-\overline{u}\frac{\partial \overline{\rho}\,\overline{u}\,\overline{w}}{\partial z} - \overline{v}\frac{\partial \overline{\rho}\,\overline{v}\,\overline{w}}{\partial z}\right). \tag{2.33}$$

The first bracket on the right is the contribution from the EP flux and the second bracket on the right is the contribution from the mean flow.

Table 2.1 shows the contribution of EP flux, mean flow interaction, $T(0)$ and $V_{adv}(0)$ in the upper troposphere and the lower stratosphere for both simulations. EP fluxes are significantly larger than the mean flow interaction in all cases. We can further our understanding of the EP flux when we consider $T(0)$ and $V_{adv}(0)$ as well. In the upper troposphere, the EP flux is dominated by $V_{adv}(0)$ in both simulations and the contribution from the mean flow is smaller. This suggests that the mean flow gains energy by vertical energy flux from the advection and the nonlinear transfer term $T(0)$ is not as important as the vertical energy flux in the upper troposphere. In other words, the direct energy cascade found in the upper troposphere does not relate to the wave-mean-flow interaction. In the lower stratosphere, we can see that the EP flux is dominated by $T(0)$ in both simulations. As a result, the fact that $T(0)$ is positive and significant (inverse energy transfer) in the lower stratosphere in both simulations can be explained by the EP flux contribution. Such inflow of energy to the mean flow from the transfer term $T(0)$ in the lower stratosphere is a result of interactions with small scale waves. Note that while $T(0)$ is stronger, the energy loss of vertical energy flux from the advection for the aggregation is also significant.

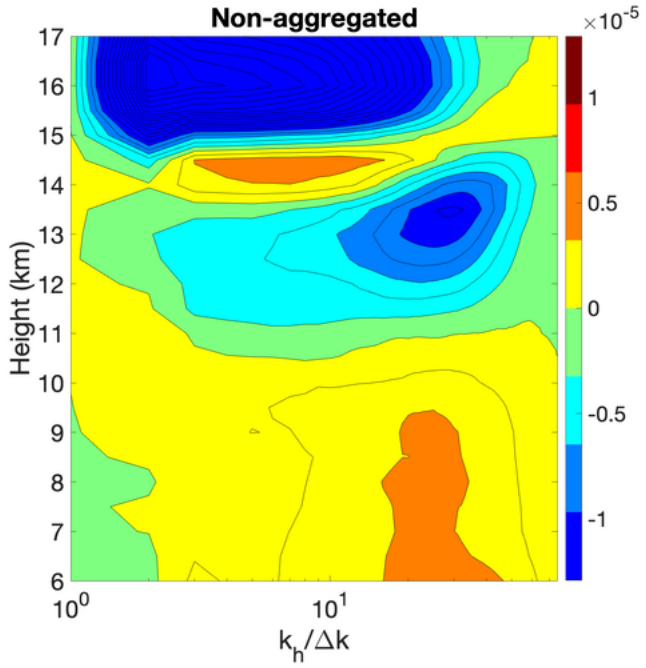


Figure 2.7: The nonlinear transfer spectral energy flux $\Pi(k, z)$ ($\mathrm{m^2 s^{-3} kgm^{-3}}$), which is averaged in time from 841 hours to 1848 hours, from height 6 km to 17 km for non-aggregated simulation.

Simulation	EP-flux	mean flow interaction	T(0)	V(0) from advection
(a) UT				
Non-agg	1.99x10^{-6}	-2.60x10^{-8}	-2.68x10^{-7}	5.17x10^{-7}
Agg	2.92x10^{-7}	5.08x10^{-10}	-1.02x10^{-8}	7.31x10^{-8}
(b) LS				
Non-agg	2.59x10^{-5}	4.99x10^{-9}	2.48x10^{-5}	-7.26x10^{-6}
Agg	5.41x10^{-6}	9.42x10^{-9}	6.28x10^{-6}	-3.34x10^{-6}

Table 2.1: The Eliassen-Palm flux contribution ($m^2 s^{-3} kgm^{-3}$), mean flow contribution ($m^2 s^{-3} kgm^{-3}$), transfer at $k_h = 0$ ($m^2 s^{-3} kgm^{-3}$), and vertical flux from the advection at $k_h = 0$ ($m^2 s^{-3} kgm^{-3}$) for (a) the upper troposphere (UT) and (b) the lower stratosphere (LS).

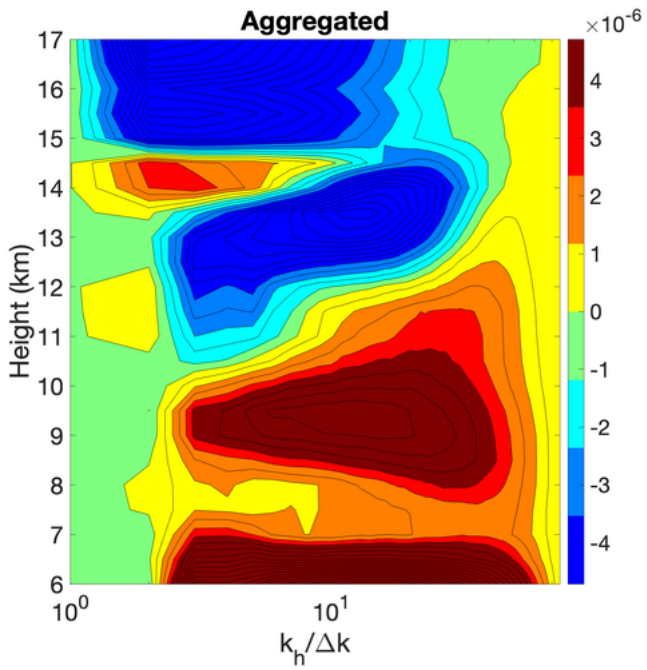


Figure 2.8: As in Fig. 2.7, but for the aggregated simulation.

2.3.4 Compensated Kinetic Energy Spectra

To compare the kinetic energy spectra to observational studies such as Li and Lindborg (2018), one-dimensional (zonal) compensated wavenumber kinetic energy spectra for the non-aggregated and aggregated simulations are computed. Density dependence is removed to compute k_x-spectra of KE per unit mass. One-dimensional compensated spectra are plotted in Fig. 2.9. The compensated kinetic energy spectra are multiplied by $k_x^{5/3}$ and plotted on log-linear axes to more carefully compare with a -5/3 spectrum. The kinetic energy spectrum from the aggregated simulation is closer to the -5/3 spectrum when compared to the non-aggregated simulation in both the upper troposphere and lower stratosphere. The kinetic energy spectrum for the non-aggregated simulation is shallower than -5/3 out to $k_x/\Delta k \approx 15$. Even though the slope of the compensated spectrum from the aggregated simulation in the upper troposphere is positive from $k_x/\Delta k = 1 - 10$, it only increases by a factor of 1.5; by contrast, the compensated kinetic energy spectrum for the non-aggregated simulation increases by a factor of approximately 4 to 5 for $k_x/\Delta k = 1-10$. The compensated kinetic energy spectrum confirms that DKE is similar to RKE in the upper troposphere and DKE dominates the lower stratosphere for both simulations.

Note that even though there is no baroclinic instability and rotation in our non-aggregated and aggregated idealized simulations, the magnitudes of our compensated kinetic energy spectra are similar to spectra calculated from aircraft data in Li and Lindborg (2018) Fig. 4. They also showed that all of their compensated kinetic energy spectra are flat in the mesoscale, which suggested that the spectra were close to the -5/3 spectrum.

2.3.5 Rotation

The effect of rotation is briefly examined in this subsection. An additional simulation with rotation is run for 42 days and results are averaged for the last 7 days. The setup of the simulation is the same as the non-aggregated simulation, except for the inclusion of mid-latitude rotation ($f = 10^{-4}$ s^{-1}). With the addition of rotation, aggregation is identified in the simulation at about 640 hours. The convective system looks similar to the aggregated simulation and remains aggregated in the remaining simulation time. In the upper troposphere, the kinetic energy spectrum resembles the -3 spectrum from $k_h/\Delta k = 6$ to $k_h/\Delta k = 20$ (Fig. 2.10a) in the rotation simulation. This is different from other studies such as the rotation simulation from Sun et al. (2017) and observation from Callies et al. (2014), which found that kinetic energy has a -5/3 spectrum at the mesoscale in the upper troposphere. In Sun et al. (2017), the simulation time was significantly shorter and there was low-level wind shear. The fact that our simulations are much longer allows time for

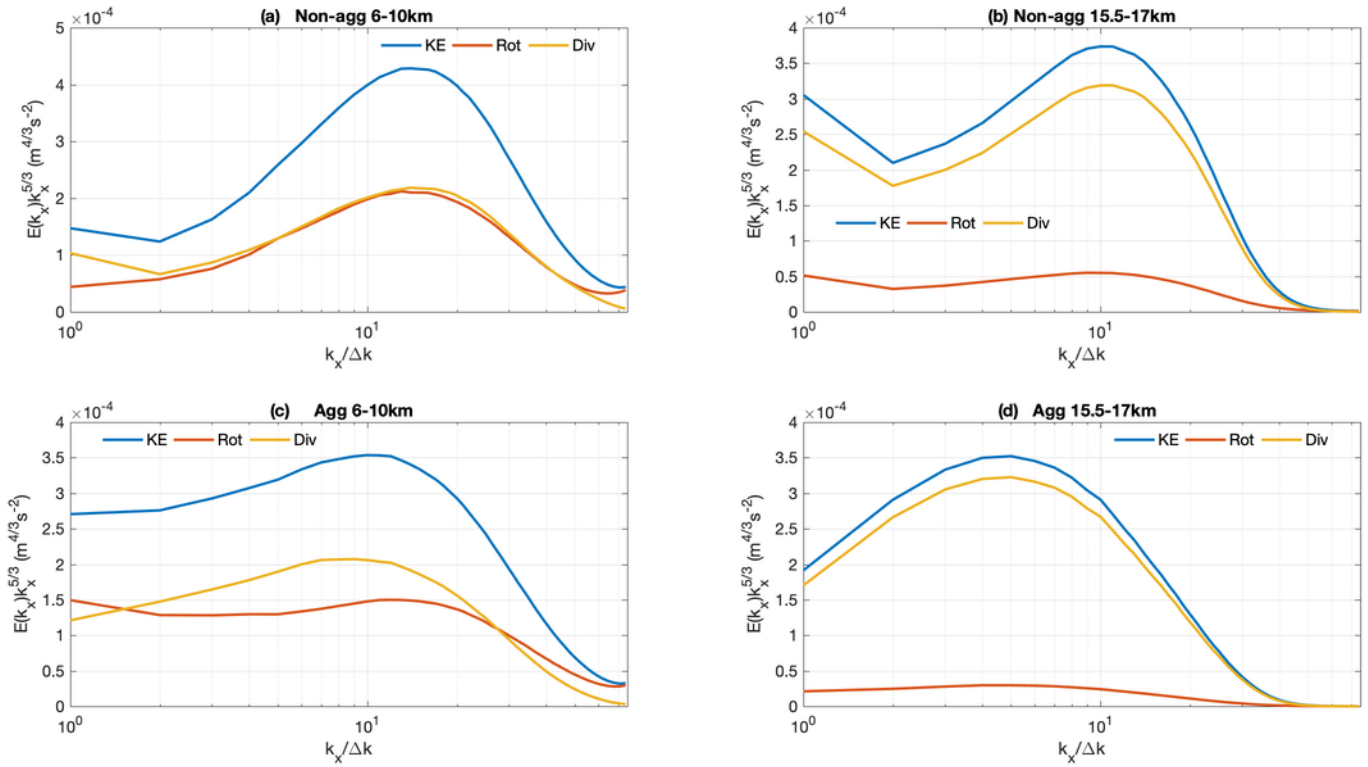


Figure 2.9: The compensated kinetic energy spectrum for the non-aggregated simulation (a) in the upper troposphere and (b) in the lower stratosphere, and for the aggregated simulation (c) in the upper troposphere and (d) in the lower stratosphere. All spectra are averaged in the vertical and in time from 841 to 1848 hours

energetic large-scale vortices to develop. In addition, the absence of imposed low-level shear in our simulations may result in different vertical structures. These two factors may explain the steeper spectrum in our study. With the addition of rotation, RKE dominates the kinetic energy spectrum for $k_h/\Delta k < 10$. DKE is marginally stronger than RKE from $k_h/\Delta k = 10$ to $k_h/\Delta k = 50$. The DKE spectrum is shallower, similar to -5/3, and so it eventually crosses the RKE spectrum, leading to marginally stronger DKE at $k_h/\Delta k > 10$, which is similar to other studies (e.g. Waite and Snyder, 2013). In the aggregated and non-aggregated simulations without rotation, RKE and DKE are similar in magnitude for most k_h. The kinetic energy spectrum from the simulation with rotation is also more energetic than the simulations without rotation. The fact that RKE $\gtrsim$ DKE in the upper troposphere in the rotation simulation is similar to the findings from other studies such as Waite and Snyder (2013) and Peng et al. (2015b).

In the upper troposphere, the energy gain from the buoyancy flux is mainly balanced by the loss of energy from the vertical energy flux for $k_h/\Delta k \lesssim 10$ in the rotation simulation. For $k_h/\Delta k \approx 10$ to $k_h/\Delta k \approx 20$, there is energy gain from the vertical energy flux that is balanced by the energy loss from the buoyancy flux. The transfer term plays a more significant role in the rotation simulation in the upper troposphere. In the simulations without rotation, the transfer term is weak in the upper troposphere. The transfer term in the rotation simulation transfer energy from large scales to small scales. Energy is dissipated by the dissipation terms at small scales.

In the lower stratosphere, the kinetic energy spectrum is steeper than -5/3 but shallower than -3. The kinetic energy spectrum for the rotation simulation in the lower stratosphere is dominated by RKE for $k_h/\Delta k \lesssim 2$ and dominated by DKE for $k_h/\Delta k > 2$. Note that this is very different from the simulations without rotation. In the simulation without rotation, the kinetic energy spectra for both simulations are dominated by DKE.

In the lower stratosphere, there is a strong energy gain from the vertical energy flux for all k_h in the rotation simulation. It is balanced by energy loss from buoyancy and dissipation. The transfer term is transferring energy out of intermediate scales into larger and smaller scales. Note that the dissipation from the subgrid turbulence scheme is significant even at large scales. The vertical resolution stretches significantly as height increases above 12 km. In our simulations, the vertical resolution at height below 10 km is fairly close to 100 m. The vertical resolution at 15.5 km is approximately 120 m and the vertical resolution at 17 km is approximately 140 m. Low vertical resolution might be leading to significant dissipation at large horizontal scales from vertical gradients (however, this large-scale dissipation was not observed in the simulations without rotation). We decided to keep the same vertical resolution in the rotating case to facilitate comparisons with the non-rotating simulations. It is worth noting that the non-negligible dissipation at large

scales in the lower stratosphere has also been reported in Fig. 9 of Menchaca and Durran (2019).

2.4 Conclusions

Aggregation in RCE has an impact on the kinetic energy spectrum. In the upper troposphere, the horizontal kinetic energy spectrum is much shallower than the $-5/3$ spectrum for the non-aggregated simulation. The spectrum for the aggregated simulation is much steeper than the spectrum for the non-aggregated simulation and closer to the $-5/3$ spectrum. This difference is consistent with the convective system being more energetic in the large scales for the aggregated simulation. In the upper troposphere, DKE is similar to RKE at most scales for the non-aggregated simulation and DKE is slightly larger than RKE for $k_h/\Delta k < 30$ (wavelengths larger than 20 km) in the aggregated simulation. The significant DKE at all scales is likely because of the fact that there is no rotation or large-scale baroclinic instability in our study. The lack of rotation leads to the domination of the DKE in the non-aggregated and aggregated simulation, as confirmed by the simulation with rotation. The addition of rotation was found to facilitate aggregation and development of a -3 spectrum dominated by RKE, in line with other studies.

In the upper troposphere, there is energy gain from the buoyancy flux for both the aggregated and non-aggregated simulations. Buoyancy flux due to latent heating from the convection injects energy into the upper troposphere. In both the non-aggregated and aggregated simulation, the energy gain from buoyancy flux is balanced by energy loss from the vertical energy flux for $k_h/\Delta k < 30$. In the upper troposphere for both simulations, the transfer term transfers some energy from large to small scales and that energy is dissipated, which is consistent with a direct energy cascade.

In the lower stratosphere, the horizontal kinetic energy spectrum is shallower than -5/3 and steepens at larger k_h from dissipation. The horizontal kinetic energy spectrum for the aggregated simulation resembles the $-5/3$ spectrum for $4 < k_h/\Delta k < 20$. DKE dominates the horizontal kinetic energy spectrum at all k_h for both simulations. The spectral budgets for both the aggregated and non-aggregated simulations are similar in shape but different in magnitude. The vertical energy flux injects energy to the lower stratosphere and this energy gain is balanced by energy loss from the buoyancy flux, the transfer term and the dissipation at most scales. Note that the sum of the transfer term has to be zero. The energy loss at $k_h/\Delta k > 1$ is transferred upscale and results in energy gain in the mean flow, which suggests that inverse energy transfer exists in the lower stratosphere. This upscale energy transfer energizes the mean flow in the lower stratosphere, which can be

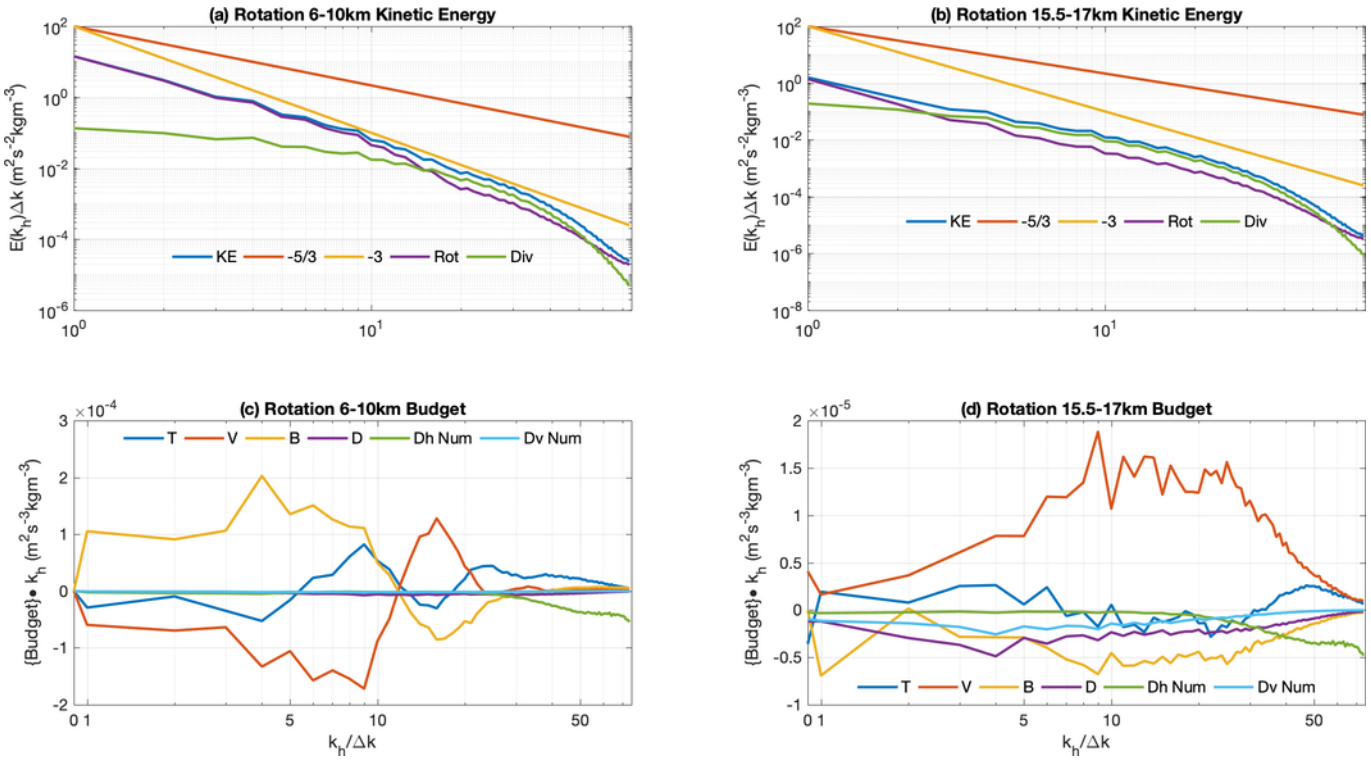


Figure 2.10: The horizontal kinetic energy spectrum (blue), rotational kinetic energy spectrum (purple), and divergent kinetic energy spectrum (green) for (a) the upper troposphere (6-10 km) of the rotation simulation and (b) the lower stratosphere (15.5-17 km) of the rotation simulation; and the spectral budget, including horizontal nonlinear energy transfer (blue), buoyancy flux (yellow), vertical flux divergence (red), dissipation from the subgrid mixing scheme (purple), and numerical dissipation (green), in the upper troposphere for (c) the upper troposphere (6-10 km) of the rotation simulation and (d) the lower stratosphere (15.5-17 km) of the rotation simulation. All spectra are averaged in the vertical and in time from 841 to 1008 hours. Budget spectra are multiplied by k_h, for all k_h except for $k_h = 0$, to preserve area on semi-log plots. Note that $k_h = 0$ is shown in Figs. c-d.

explained by the Eliassen-Palm wave-mean-flow analysis. The transfer of energy to the mean flow in the lower stratosphere is likely due to interactions with small-scale waves. Strong wave activity in the lower stratosphere triggers the wave-mean-flow interaction, and hence energy is transferred from small scales to the mean flow. This may suggest that wave-mean-flow interaction may be responsible for the inverse energy transfer in the lower stratosphere, but not necessarily the same kind of energy cascade/transfer found in inertial-gravity waves and strongly stratified turbulence in explaining the -5/3 spectrum.

Even without large-scale forcing and rotation in our non-aggregated and aggregated simulations, the magnitudes of our compensated kinetic energy spectra are similar to spectra calculated from aircraft data. Our results show that latent heating and radiative cooling, through buoyancy and vertical energy fluxes, can force a KE spectrum that resembles a -5/3 power law. This spectrum is not due to a turbulent cascade; the role of the nonlinear advective transfer is relatively insignificant. These results serve as a caution that care should be taken when making interpretations about dynamics from the shape of the KE spectrum alone. Note that aggregation does not seem to be an inverse cascade; it results from the buoyancy flux and the vertical energy flux, not the transfer.

In this work, we use model simulations to explore different phenomena and mechanisms that govern the mesoscale energy spectrum. These phenomena and mechanisms are present in the real atmosphere, and idealized simulations allow us to isolate them. RCE experiments focus on dynamics driven by convection, in contrast to previous idealized studies that have focused on, for example, stratified turbulence (Lindborg, 2006) and baroclinic instability (Waite and Snyder, 2009). We show that RCE develops an energetic mesoscale from a spectral budget that is not an energy cascade, but rather a balance between buoyancy flux and vertical flux. The implication of these results is that in regions dominated by convection, the mesoscale spectrum develops differently than a turbulent cascade.

Future work should focus on the effect of domain size and more carefully identifying gravity waves. Due to the computational expense, it is difficult to run long RCE simulations with a larger domain or higher resolution. Limited domain size may affect our results, and presents a challenge for comparisons with other studies at larger scales. The energy transfer to the mean flow should be investigated with a larger domain. Note that in Peng et al. (2015b) and Menchaca and Durran (2019), the domain size of their simulation was significantly larger than the simulations we presented and rotation was present. This suggests that an inverse energy cascade may exist at scale as large as O(1000 km), at least in the presence of rotation. While we suggest that wave activity may lead to energy transfer from small to large scales, more investigation should be performed. In the H500 mountain simulation from Menchaca and Durran (2019), DKE dominated the HKE spectra in the lower stratosphere at scales less than 900 km. Hence, they concluded that IGWs are

important in the lower stratosphere and that might be an explanation for the inverse energy transfer. Is there a way to measure wave activity at a particular length scale? There is a need to confirm if wave activity is crucial in explaining the inverse energy transfer found in the lower stratosphere in the future. DKE is one tool but more work is needed to confirm that DKE identifies waves, and how the wave-mean-flow interaction in our work compares to the inverse cascades reported elsewhere.

2.5 Acknowledgments

This research was enabled in part by support provided by the Shared Hierarchical Academic Research Computing Network (SHARCNET: www.sharcnet.ca) and the Digital Research Alliance of Canada (alliancecan.ca), and funding from the Natural Sciences and Engineering Research Council of Canada and the Canadian Foundation for Innovation.

2.6 Appendix: Modified Equation

When investigating the effect of numerical dissipation for a partial differential equation, the modified equation can be used. The modified equation is a partial differential equation to which the discretization is a better approximation that the original PDE. It takes both the temporal and spatial discretization into consideration. The modified equation for a one-dimensional linear advection equation, discretized as in WRF, will be given in this section. Consider an advection equation $\frac{\partial q}{\partial t} = -U\frac{\partial q}{\partial x}$ with a constant and positive flow velocity of U. The RK3 time-integration scheme used by WRF for the advection (Skamarock et al., 2008) is given by

$$q_i^{n+1} = q_i^n - \frac{U\Delta t}{\Delta x}(q_{i+\frac{1}{2}}^{**} - q_{i-\frac{1}{2}}^{**}), \tag{2.34}$$

where

$$q_i^{**} = q_i - \frac{U\Delta t}{2\Delta x}(q_{i+\frac{1}{2}}^{*} - q_{i-\frac{1}{2}}^{*}), \tag{2.35}$$

$$q_i^{*} = q_i - \frac{U\Delta t}{3\Delta x}(q_{i+\frac{1}{2}} - q_{i-\frac{1}{2}}). \tag{2.36}$$

For horizontal advection, a fifth order discretization for $q_{i-\frac{1}{2}}$ is used:

$$q_{i-\frac{1}{2}} = (q^{adv})_{i-\frac{1}{2}}^{6th} - \frac{1}{60}((q_{i+2} - q_{i-3}) - 5(q_{i+1} - q_{i-2}) + 10(q_i - q_{i-1})), \tag{2.37}$$

where $(q^{adv})^{6th}_{i-\frac{1}{2}}$ is the sixth order flux

$$(q^{adv})^{6th}_{i-\frac{1}{2}} = \frac{37}{60}(q_i + q_{i-1}) - \frac{2}{15}(q_{i+1} + q_{i-2}) + \frac{1}{60}(q_{i+2} + q_{i-3}). \tag{2.38}$$

Letting $Cr = U\Delta t/\Delta x$, we can substitute the flux in (2.37) in (2.34-2.36), then Taylor expand to obtain

$$\begin{aligned} &\frac{\partial q}{\partial t} + \frac{\Delta t}{2!}\frac{\partial^2 q}{\partial t^2} + \frac{\Delta t^2}{3!}\frac{\partial^3 q}{\partial t^3} + \frac{\Delta t^3}{4!}\frac{\partial^4 q}{\partial t^4} + \frac{\Delta t^4}{5!}\frac{\partial^5 q}{\partial t^5} + \frac{\Delta t^5}{6!}\frac{\partial^6 q}{\partial t^6} \\ &\quad = -U\frac{\partial q}{\partial x} + \frac{1}{\Delta t}\left[\frac{Cr}{60}\Delta x^6\frac{\partial^6 q}{\partial x^6} + \frac{Cr^2}{2}\left(\Delta x^2\frac{\partial^2 q}{\partial x^2}\right) - \frac{Cr^3}{3!}\left(\Delta x^3\frac{\partial^3 q}{\partial x^3}\right)\right] + h.o., \end{aligned} \tag{2.39}$$

where $h.o.$ represents the sixth order terms.

The modified equation for the horizontal advection can be obtained by repeatedly differentiating (2.39) to replace time derivatives with spatial derivatives (as in e.g. Durran, 2010):

$$\frac{\partial q}{\partial t} + U\frac{\partial q}{\partial x} = \left(\frac{Cr}{60\Delta t}\Delta x^6 - \frac{UCr^5\Delta x^5}{72}\right)\frac{\partial^6 q}{\partial x^6} - \frac{UCr^3\Delta x^3}{24}\frac{\partial^4 q}{\partial x^4} - \frac{UCr^4\Delta x^4}{30}\frac{\partial^5 q}{\partial x^5} + h.o. \tag{2.40}$$

Note that the third term on the right side of (2.40) is dispersive and the first and second term on the right side of (2.40) are dissipative. Similarly, letting $Cr = W\Delta t/\Delta z$, the modified equation for the vertical advection (Skamarock et al., 2008) is

$$\frac{\partial q}{\partial t} + W\frac{\partial q}{\partial z} = \frac{-Cr}{12\Delta t}\Delta z^4\frac{\partial^4 q}{\partial z^4} - \frac{WCr^3\Delta z^3}{24}\frac{\partial^4 q}{\partial z^4} + h.o., \tag{2.41}$$

where $h.o.$ represents the terms which are $O(\Delta z^4)$. Note that the first two terms in (2.41) are dissipative. The horizontal numerical dissipation and vertical numerical dissipation presented are defined using the first two terms of (2.40) and (2.41), respectively.

3

Backscatter in Radiative-Convective Equilibrium

3.1 Introduction

Radiative convective equilibrium (RCE) is an idealized model for the atmosphere of tropical regions. The radiative cooling and convective heating are balanced in RCE to reach an equilibrium state (e.g. Wing et al., 2017). Its simplicity makes it a useful framework for the comparison of parameterizations. RCE is also an ideal framework for the fundamental study of convectively-driven moist fluid dynamics. For example, RCE has been used in studies of subgrid scale parameterizations such as the role of entrainment (e.g. Tompkins and Semie, 2017) and cloud microphysics (e.g. Satoh and Matsuda, 2009). Because of the absence of baroclinic instability and large-scale forcing, RCE creates convective plumes of various length scales.

There is a well-known phenomenon in idealized RCE simulation of self-aggregation (e.g. Wing et al., 2017), in which many small, random convective plumes organize into several large convective systems. Tompkins and Semie (2017) performed an investigation of the role of entrainment on self-aggregation using different subgrid turbulence mixing schemes. Their results suggested that a less dissipative subgrid turbulence scheme was less likely to lead to self-aggregation in RCE simulations. This was a likely explanation for the resolution dependence of self-aggregation found in other studies, such as Muller and Held (2012).

Direct numerical simulation (DNS) solves the governing equations with a resolution that can resolve the smallest dissipative eddies, which is impossible for geophysical scale

flows. As a result, significant resources are needed if the domain or time of the simulation is large. A more cost-effective solution is large eddy simulations (LES). It is a technique that simulates only the large, energy-containing eddies and parameterizes the eddies that are smaller than the grid resolution. Subgrid scale turbulence mixing schemes parameterize the subgrid scale turbulence. In idealized cloud-resolving simulations, the eddy viscosity model is one of the most commonly used subgrid turbulence mixing schemes (e.g. Bryan and Morrison, 2012; Muller and Held, 2012; Lai and Waite, 2020). These models are dissipative by design because they are developed based on the energy cascade hypothesis (e.g. Meneveau and Katz, 2000; Moser et al., 2021). While it is true that the energy transfers from the resolved scales to subgrid scales on average, it is not always true in a local sense. Locally, there can be an energy transfer from subgrid scales to resolved scales. Such energy transfer from subgrid scales to resolved scales is known as backscatter. Research on isotropic turbulence (e.g. Domaradzki et al., 1993; Vela-Martín, 2022), stratified turbulence (e.g. Khani and Waite, 2016) and idealized squall lines (e.g. Lai and Waite, 2020) have shown that while the net subfilter energy transfer rate is dissipative, it is the net result of a large amount of dissipation and backscatter. Khani and Waite (2016) found that an increase in the buoyancy Reynolds number increased the subfilter energy transfer rate. Hence, they suggested that the subfilter energy transfer rate was not random and it might relate to the characteristics of a flow. As a result, RCE is an ideal platform for performing a subfilter energy transfer rate analysis. Analysis of subfilter energy transfer rate is often used in the development of a subgrid mixing scheme (e.g. Moeng et al., 2010; Thiry and Winckelmans, 2016; Khani and Porté-Agel, 2017; Vela-Martín, 2022).

Subfilter energy transfer rate analysis is important because commonly used eddy viscosity schemes are overly dissipative with no backscatter (e.g. Meneveau and Katz, 2000; Pope, 2000). It is important to investigate the role of backscatter in convectively-driven atmospheric flows. We also know that RCE is sensitive to eddy viscosity (e.g. Tompkins and Semie, 2017). Hence, RCE is a good place to explore the effect of backscatter to improve subgrid turbulence schemes that include backscatter, such as the dynamic Smagorinsky models and stochastic backscatter models (e.g. Pope, 2000). Turbulence parameterization evaluations are often done by course-graining or filtering the outputs from DNS (e.g. Khani and Porté-Agel, 2017). The effect of turbulence mixing at the order of kilometres are still unknown and it is prohibitively expensive to analyze such scales by filtering DNS.As a result, it is cost-effective if one can study the effects of turbulence parameterizations by course-graining high-resolution LES simulations rather than DNS (Verrelle et al., 2015, 2017; Strauss et al., 2019, 2022). In this chapter, we apply a similar technique of course-graining a LES to study subfilter energy transfer. Subfilter energy transfer can be analyzed with a priori analysis, where data from a high-resolution simulation is filtered,

and the subfilter energy transfer is calculated explicitly. Normally, subfilter energy transfer rate analyses are done on turbulence DNS (e.g. Piomelli et al., 1991; Khani and Waite, 2016; Khani and Porté-Agel, 2017; Buzzicotti et al., 2018). An alternative approach, which is more feasible for atmospheric flows, is to filter LES output to perform the subfilter energy transfer analysis at kilometre scales. Such an approach has been used in Lai and Waite (2020) on an idealized squall line simulation. In Lai and Waite (2020), the high-resolution simulation was filtered horizontally to a scale of 1 km. They found that while the net subfilter energy transfer rate was dissipative, it was the result of a large amount of dissipation and backscatter. They also found that the streamwise and shear components were responsible for the significant rate of the subfilter energy transfer in the core of the idealized squall line simulation.

In Chapter 2, we performed an analysis of kinetic energy spectra and the spectral energy budget in RCE. We found that while there was downscale energy transfer in the upper troposphere, upscale energy transfer was found in the lower stratosphere. We suggested that wave-mean-flow interaction could be one of the responsible mechanisms for the upscale energy transfer in the lower stratosphere. To understand small-scale energy transfers in convectively-driven environments, implications for energy cascades and parameterizations, we will perform an a priori study on the subfilter energy transfer rate at O(km) scales in RCE. The remaining chapter will be organized as follows. Section 3.2 is the methodology. In the methodology section, we will give the details of the model and the details of the subfilter energy transfer rate analysis. In section 3.3, we will present our results and discussion. In particular, section 3.3.1 will be an overview of the simulation. Sections 3.3.2 and 3.3.3 will be the results and discussions of the subfilter energy transfer rate with the box filter and its components. In section 3.3.4, we will discuss the effect of the Gaussian filter and the spectral cutoff filter on the subfilter energy transfer rate. In section 3.3.5, we will present the horizontal kinetic energy spectra and the spectral energy budget. Section 3.4 will be the conclusion section.

3.2 Methodology

3.2.1 Model

The simulations presented in this chapter are performed using the Advanced Research Weather Research and Forecasting (WRF) model (Skamarock et al., 2008). WRF solves the fully compressible non-hydrostatic Euler equations. The time-stepping scheme that WRF uses is the third-order Runge-Kutta scheme. A third-order finite-difference advection

scheme is used in the vertical direction, and a fifth-order finite-difference advection scheme is used in the horizontal directions.

The main simulation presented in this chapter originates from the RCE test case in WRF. The domain size of the simulation is 600 km (x) $\times$ 600 km (y) $\times$ 25 km (z). The sea surface temperature in our simulation is 302 K. The Revised MM5 Monin-Obukhov surface layer scheme (Jiménez et al., 2012) is used in our simulation. Longwave and shortwave RRTMG radiation schemes (Iacono et al., 2008) with no diurnal cycle are used. The zenith angle is 50.5 degrees, which is equivalent to incoming solar radiation of 434.12 W/m^2 (e.g. Holloway and Woolnough, 2016). There is no rotation and no planetary boundary layer (PBL) scheme in our simulation. A PBL scheme parameterizes the vertical heat, moisture and momentum turbulence mixing in the boundary layer. A PBL scheme is not used in this thesis for three reasons. First, a three-dimensional subgrid turbulence scheme, which includes vertical mixing, is used, so a PBL is not necessary. Second, the study presented in this chapter should be consistent with the previous chapter, where no PBL scheme is used. Third, the spectral energy budget is simpler without a PBL scheme. Periodic boundary conditions in x and y are used. The microphysics scheme used in this simulation is the Thompson scheme (Thompson et al., 2008).

The simulation uses a terrain-following hydrostatic pressure coordinate as the vertical coordinate, with 199 vertical levels. The vertical resolution is not uniform in height. The vertical level spacing from the bottom of the domain to 15 km of height is approximately 100 m; the level spacing is then stretched from approximately 100 m at a height of 15 km to approximately 400 m at the top of the domain. There is a 5 km Rayleigh damping layer at the top of the domain with a damping coefficient of 0.003 s^{-1}.

The simulation is run for 14 days with a 1-km horizontal resolution with the standard 1.5 order turbulence kinetic energy (TKE) subgrid turbulence mixing scheme (Skamarock et al., 2008). The initial condition of the simulation is created by a spin-up simulation. The spin-up simulation is the non-aggregated simulation presented in Chapter 2. The spin-up simulation has the same setup as the simulation presented in this chapter, except that the spin-up simulation has a lower resolution. The spin-up simulation is run for 63 days. The last output of the spin-up simulation is interpolated from a horizontal resolution of 4 km to 1 km to create the initial condition for the 1-km simulation that we present in this chapter. The simulation is then run for 14 days with an increased horizontal resolution of 1 km for our analysis. A lower-resolution simulation with 4 km resolution is also performed over the same 14-day period for comparison.

3.2.2 Diagnostics

To investigate backscatter, we will perform a priori analysis. The subfilter energy transfer rate P (e.g. Piomelli et al., 1991) is defined as

$$P(x_1, x_2, x_3, t) = \rho(x_1, x_2, x_3, t) \sum_{i,j=1}^{3} \tau_{ij}(x_1, x_2, x_3, t)\overline{S_{ij}}(x_1, x_2, x_3, t), \tag{3.1}$$

where ρ is the density and $\overline{(\cdot)}$ represent a low-pass filter. In this chapter, we will calculate the subfilter energy transfer rate with three different filters, and the details of these filters will be discussed later. Let

$$\tau_{ij} = \overline{u_i u_j} - \overline{u_i}\ \overline{u_j}$$

be the subgrid scale momentum flux and

$$\overline{S_{ij}} = \frac{1}{2}\left(\frac{\partial \overline{u_i}}{\partial x_j} + \frac{\partial \overline{u_j}}{\partial x_i}\right)$$

be the filtered rate of strain tensor. The subfilter energy transfer rate is the sum of nine components $P = \Sigma_{i,j=1}^{3} P_{ij}$. The components of P are defined as

$$P_{ij}(x_1, x_2, x_3, t) = \rho(x_1, x_2, x_3, t)\tau_{ij}(x_1, x_2, x_3, t)\overline{S_{ij}}(x_1, x_2, x_3, t), \tag{3.2}$$

where $i, j = 1, 2, 3$ (no summation over i and j). Note that P_{ij} is symmetric, which means that $P_{ij} = P_{ji}$. Consistent with Lai and Waite (2020), backscatter is defined as the positive value of the subfilter energy transfer rate

$$P_+(x_1, x_2, x_3, t) = \frac{P(x_1, x_2, x_3, t) + |P(x_1, x_2, x_3, t)|}{2},$$

which represents the energy added to the resolved flow from subfilter to filtered, and dissipation is the negative value of the subfilter energy transfer rate

$$P_-(x_1, x_2, x_3, t) = \frac{P(x_1, x_2, x_3, t) - |P(x_1, x_2, x_3, t)|}{2},$$

represents the energy removed from the filtered to subfilter.

Filters are defined following Pope (2000). Since we are investigating the effect of small horizontal scales on RCE, the filters are only applied in the horizontal directions. When defining the filters, Δ_1 and Δ_2 are filtered scales in x_1 and x_2, respectively. We are filtering

the 1-km resolution data to a horizontal scale of 4 km, so $\Delta_1 = \Delta_2 = \Delta = 4$ km. Note that 4 km is also the resolution of the simulations presented in Chapter 2, which makes it convenient for comparison. The box filter is defined as

$$\overline{\zeta}(a,b) = \frac{1}{\Delta^2}\int_{a-\frac{\Delta}{2}}^{a+\frac{\Delta}{2}}\int_{b-\frac{\Delta}{2}}^{b+\frac{\Delta}{2}} \zeta(x_1,x_2)dx_1dx_2, \tag{3.3}$$

The Gaussian filter is defined as

$$\overline{u}(a,b) = \int_{-\infty}^{\infty}\int_{-\infty}^{\infty} u(x_1-a,x_2-b)G(x_1)G(x_2)dx_1dx_2, \tag{3.4}$$

where

$$G(r) = \sqrt{\frac{6}{\pi\Delta^2}}\exp\left(\frac{-6r^2}{\Delta^2}\right)$$

is the Gaussian filter function following Pope (2000). The spectral cutoff filter is defined using the Fourier transform. Let $\hat{U}(k,l)$ be the Fourier transform of $U(x_1,x_2)$. The filtered field

$$\hat{\overline{U}}(k,l) = \hat{G}(k)\hat{G}(l)\hat{U}(k,l), \tag{3.5}$$

where $\hat{G}(k) = H(k_c - |k|)$ with $k_c = \pi/\Delta$ and $\hat{G}(l) = H(l_c - |l|)$ with $l_c = \pi/\Delta$.

Note that both the box filter and Gaussian filter do not have clear cutoffs at the filter scale. To avoid aliasing in the subfilter energy transfer rate with the spectral cutoff filter, the data is interpolated to 50% higher resolution using fast Fourier transform before applying the spectral cutoff filter. To compare the subfilter energy transfer rate at a horizontal resolution of 4 km, we also calculated the eddy dissipation of the 4-km non-aggregated simulation. In the 4-km non-aggregated simulation, the modelled subgrid scale momentum flux is defined by (Skamarock et al., 2008)

$$\tau_{ij}^d = -2K_{h,v}\overline{S_{ij}}, \tag{3.6}$$

where K_h is the horizontal eddy viscosity and K_v is the vertical eddy viscosity given by the TKE subgrid turbulence mixing scheme in chapter 1. K_v is used when at least one of i,j is 3, otherwise, K_h is used. The eddy dissipation is defined as

$$P_K(x_1,x_2,x_3,t) = \rho(x_1,x_2,x_3,t)\sum_{i,j=1}^{3}\tau_{ij}^d(x_1,x_2,x_3,t)\overline{S_{ij}}(x_1,x_2,x_3,t), \tag{3.7}$$

which is consistent with the definition of the subfilter energy transfer rate from equation 3.1.

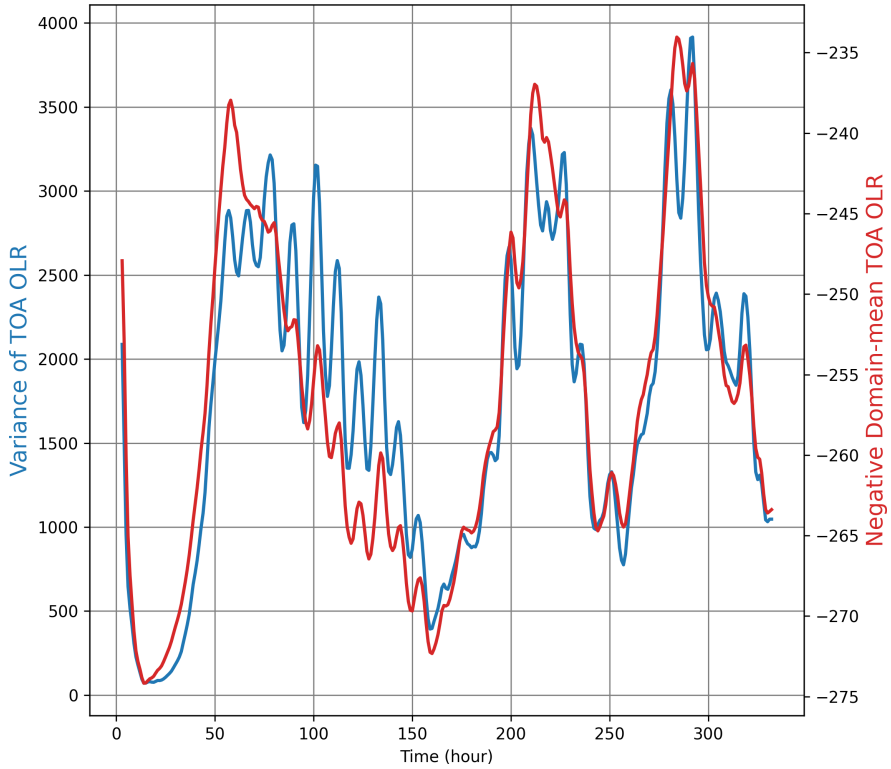


Figure 3.1: The time series of the domain-averaged variance of TOA OLR (blue) and the negative of the domain-mean TOA OLR (red). The negative is added to the domain-mean TOA OLR to show that the variance of the TOA OLR aligns with the negative of the domain-mean TOA OLR. A 6-hour moving average is used to improve readability.

3.3 Results and Discussion

3.3.1 Overview of the Simulations

To give a general picture of the evolution of aggregation and disaggregation of convection in the simulation, time series of the variance of the outgoing longwave radiation (OLR) and the negative domain-mean OLR at the top of the atmosphere (TOA) are shown in figure 3.1. The most intuitive way of identifying aggregation is by spotting the formation of one or several convective systems. As a result, we quantify aggregation using the variance of TOA OLR and the negative domain-mean TOA OLR. If there are only several isolated convective plumes, the variance of OLR will be large. Whereas, if the convective plumes

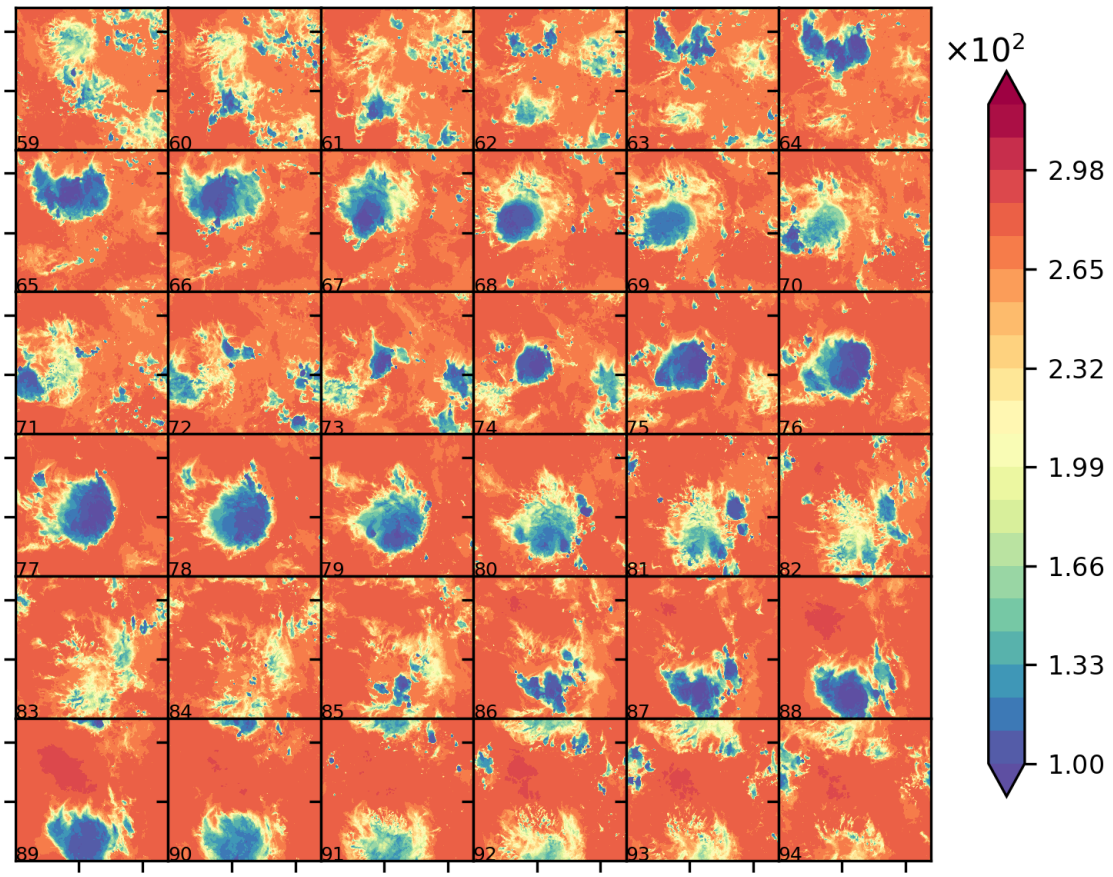


Figure 3.2: The outgoing longwave radiation (W/m^2) at the top of the atmosphere (TOA OLR) from hours 59 to 94 to show the typical evolution of a non-aggregated simulation in RCE. Note that the presented plots show the full 600 km (x) $\times$ 600 km (y) domain.

are randomly distributed over the whole domain, the variance of OLR will be small. In other words, the variance of OLR increases when there is aggregation. Similarly, if there is aggregation, the majority of the domain will have little to no clouds. Therefore, there will be an increase in domain-mean TOA OLR when there is aggregation. As a result, some previous studies (e.g. Wing and Emanuel, 2014) suggested using the domain-mean OLR as a metric for quantifying aggregation.

The first approximately 40 hours of the simulation are the adjustment period due to the increase in the resolution at the start of the simulation. After this adjustment, three main aggregation periods are represented in the three peaks in figure 3.1. The first peak happens at about 50 to 100 hours, the second peak happens at about 200 to 230 hours, and the third peak happens at about 275 to 300 hours. Within those peaks, there are still strong fluctuations in the time series of the variance of TOA OLR, which suggests that the convective system aggregates and disaggregates rapidly. At about 150 hours, 250 hours and 325 hours, the variance of OLR and the negative domain-mean TOA OLR reach a low point after a peak.

It has been shown that a less dissipative subgrid turbulence mixing scheme combined with a relatively high resolution does not produce aggregation in RCE (Tompkins and Semie, 2017). As expected, because of the resolution and the use of the default TKE subgrid turbulence mixing scheme, the convective system does not stay aggregated throughout the simulation. The simulation presented is considered a non-aggregated simulation of RCE. Similar behaviour occurs in the non-aggregated simulation of Chapter 2, from which this simulation is initialized.

The evolution of the OLR at TOA from 59 to 94 hours is presented in figure 3.2 to visualize the simulation. As seen in figure 3.1, there are three main aggregation periods in the simulation, and the event shown in the OLR at the TOA in figure 3.2 is in the first aggregation event of our simulation. Note that while some short-lived aggregation occurs in the simulation presented in this chapter, this is still considered as a non-aggregated simulation. In aggregated simulations (cf. aggregated simulation from Ch. 2), the convective system stays aggregated after the initial aggregation and it is very hard for an aggregated simulation to disaggregate (Wing et al., 2017). For non-aggregated simulations, even though there is some aggregation, it disaggregates quickly and the convective system does not stay aggregated for a long time. TOA OLR is used to visualize the evolution of deep clouds. From the evolution of the OLR at the TOA (Fig. 3.2), small and random convective plumes organize into a large convective system (74 to 79 hours in Fig. 3.2). The aggregated convective system is usually circular. The diameter of an aggregated convective system is approximately 300 km, which is about the size of half of the domain. The large convective system does not stay aggregated, and it disaggregates after a short time (80 to 84 hours in

Fig. 3.2). This behaviour is typical in non-aggregated simulation of RCE, and the process of aggregating and disaggregating will repeat throughout the simulation (as in Chapter 2). Around the time of the OLR peaks, there are multiple cycles of aggregation and disaggregation with periods of approximately 12 hours. As suggested by figure 3.2, there are three cycles of aggregation and disaggregation between 59-94 hours. One can also identify the period as approximately 12 hours by noting that there are four small oscillations between 50-100 hours from the variance of TOA OLR in figure 3.1. At the times with low values of variance of TOA OLR and negative domain-mean TOA OLR (approximately 160 hours, not shown), there is little to no convection in the whole domain.

3.3.2 Subfilter Energy Transfer Rate

To investigate the subfilter energy transfer rate in RCE, we perform a priori analysis. In this subsection, we will discuss the subfilter energy transfer rate calculated with the box filter in the upper troposphere and lower stratosphere. Similar to Chapter 2, the upper troposphere is defined as the altitude between 6-10 km and the lower stratosphere is defined as the altitude between 15.5 to 17 km. The effect of different filters will be discussed in section 3.3.4.

The net subfilter energy transfer rate is the sum of a large amount of dissipation and backscatter in both the upper troposphere and the lower stratosphere (Fig. 3.3). This is consistent with the findings from studies on transitional flow (e.g. Piomelli et al., 1991), stratified turbulence (e.g. Khani and Waite, 2016; Khani and Porté-Agel, 2017) and idealized squall line simulation (e.g. Lai and Waite, 2020). The three OLR peaks in figure 3.1 that correspond to periods of aggregations can also be observed in the dissipation and backscatter in the upper troposphere and lower stratosphere. The times at which the dissipation and backscatter peak in both the upper troposphere and lower stratosphere coincide well with the time series of the variance of OLR. In the variance of OLR, the first two peaks have a similar magnitude, and the last peak is slightly stronger than the previous two peaks. Similar results are identified with the time series of the subfilter energy transfer rate in both the upper troposphere and lower stratosphere. Table 3.1 shows the correlation between the subfilter energy transfer rate with the box filter and the OLR in the upper troposphere and lower stratosphere, respectively. Only the correlation for the box filter is shown because the results from the other two filters give similar conclusions. The dissipation and backscatter are correlated to the domain-mean OLR and the variance of the OLR. This suggests that the evolution of the dissipation and backscatter is affected by the aggregation and disaggregation of the convective system.

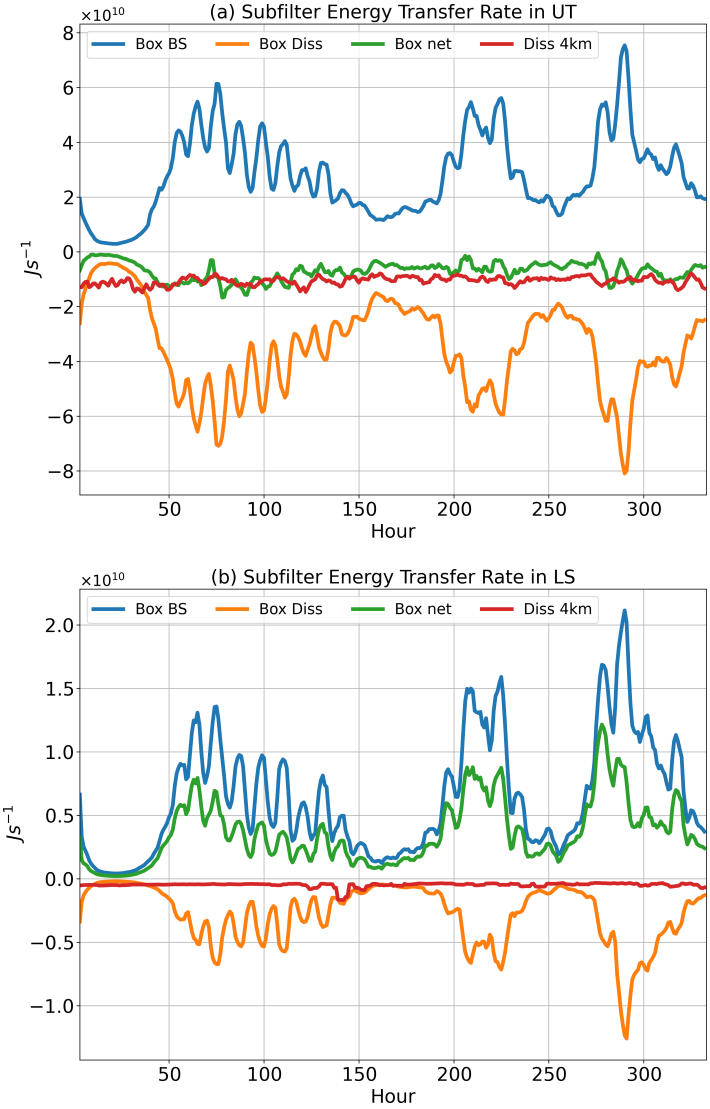


Figure 3.3: Time series of domain total subfilter energy transfer rate $\iiint_V P dx_1 dx_2 dx_3$ with box-filter (Box) (a) in the upper troposphere and (b) in the lower stratosphere. A 6-hour moving average is used to improve the readability. Backscatter (BS) is the integral of the positive value ($\iiint_V P_+ dx_1 dx_2 dx_3$) of the subfilter energy transfer rate to represent the energy added to the resolved flow, dissipation (Diss) is the negative value ($\iiint_V P_- dx_1 dx_2 dx_3$) of the subfilter energy transfer rate to represent the energy removed from the resolved flow, and the net dissipation $\iiint_V P_+ dx_1 dx_2 dx_3$ is the sum of dissipation and backscatter. The dissipation given by the eddy viscosity from the 4-km non-aggregated simulation is also included for comparison.

To further investigate the cause of these correlations, we separate the time series of dissipation and backscatter in regions with high OLR (OLR215K) and low OLR (OLR$\leq$ 215K) in the upper troposphere (Fig. 3.4) and the lower stratosphere (Fig. 3.5). The time series of dissipation and backscatter in regions with high OLR are relatively flat compared to regions with low OLR in both the upper troposphere and the lower stratosphere. This suggests that dissipation and backscatter do not have significant changes during the simulation time in high OLR regions. In the upper troposphere, the regions with low OLR have strong dissipation and backscatter, and the regions with high OLR have significantly weaker dissipation and backscatter than the low OLR regions when aggregation occurs (Fig. 3.4). In the lower stratosphere, while dissipation and backscatter in low OLR regions are still stronger than in high OLR regions, dissipation in the low OLR region is marginally stronger than dissipation and backscatter in the high OLR regions when aggregation occurs (Fig. 3.5). Note that regions with low OLR correspond to regions with deep convection. These results from the conditional time series of dissipation and backscatter based on OLR suggest that regions with deep convections are responsible for the majority of the dissipation and backscatter.

	OLR mean	OLR variance
Box net (UT)	0.32	-0.39
Box backscatter (UT)	-0.73	0.80
Box dissipation (UT)	-0.77	0.86
Box net (LS)	-0.66	0.65
Box backscatter (LS)	-0.70	0.74
Box dissipation (LS)	-0.64	0.72

Table 3.1: The correlation between the time series of the subfilter energy transfer with the box filter and the time series of mean OLR and variance of OLR in the upper troposphere (UT) and the lower stratosphere (LS)

In the upper troposphere, the net subfilter transfer rate is negative at all times (Fig. 3.3a), which means that the net subfilter transfer rate is dissipative, and there is energy transfer from filtered to subfilter scales. Since the evolution of the dissipation and backscatter are very similar, the resulting time series of the net subfilter energy transfer rate is relatively flat when compared to the time series of the dissipation and backscatter. Hence, the three peaks can not be easily identified in the net subfilter energy transfer rate in the upper troposphere. The fact that the net subfilter energy transfer rate is flat is because the strong backscatter and dissipation cancel each other. The modelled dissipation from the 4-km non-aggregated simulation is more dissipative than the net subfilter energy transfer rate

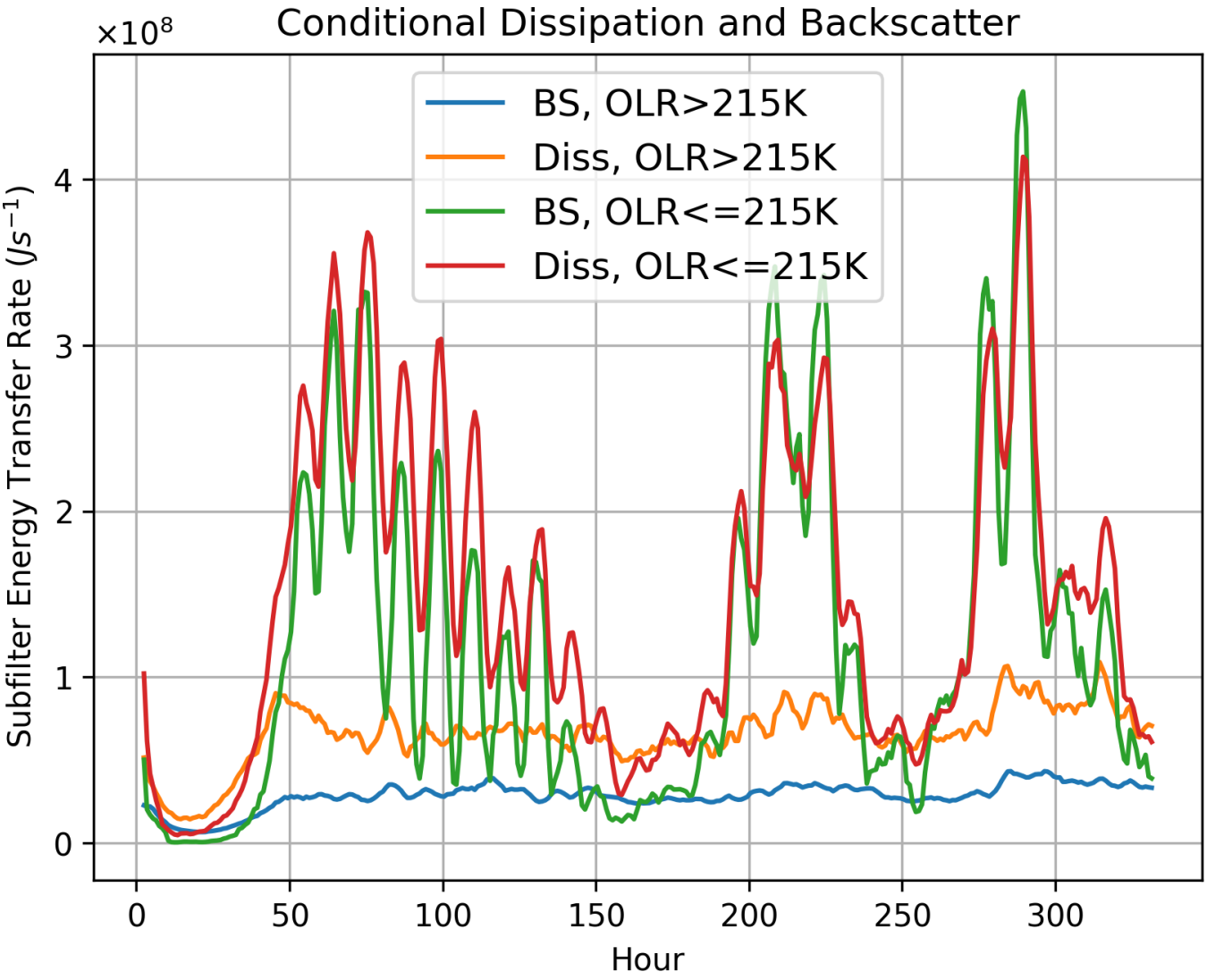


Figure 3.4: Time series of vertically-averaged dissipation (Diss) and backscatter (BS) with box-filter in region with high OLR (OLR$<$ 215K) and low OLR (OLR$\leq$ 215K) in the upper troposphere. A 6-hour moving average is used to improve the readability.

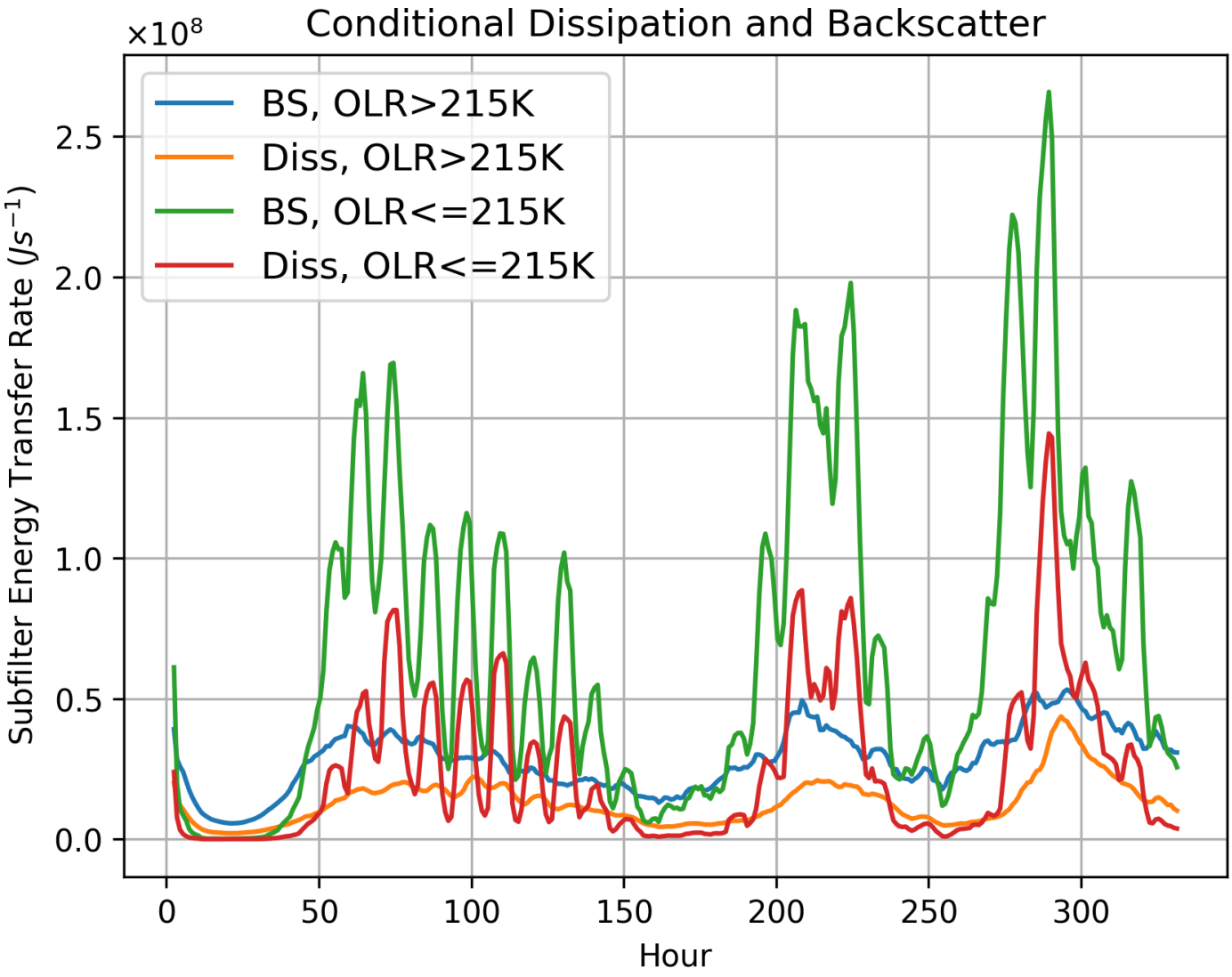


Figure 3.5: As in Fig. 3.4, but in the lower stratosphere.

after the initial adjustment period. Note that the eddy dissipation in the 4 km simulation also parameterizes dissipation due to unresolved vertical scales, which are not captured in the a priori analysis of the 1-km simulation. Overall, these results suggest that at a horizontal scale of 4 km, there are lots of interactions between the resolved and the subfilter scales that are not captured by a purely dissipative subgrid turbulence mixing scheme.

Unlike in the upper troposphere, the net subfilter energy transfer rate in the lower stratosphere is positive at all times (Fig. 3.3b), which means that there is net backscatter at the filter scale of 4 km. Backscatter at the filter scale of 4 km indicates that there is a transfer of energy from subfilter (sub-4 km) scales to resolved scales (scales larger than 4 km). The three peaks identified in the variance of TOA OLR align well with the three peaks in the dissipation and backscatter in the lower stratosphere. Similar to the upper troposphere, the first two peaks of the dissipation and the backscatter have similar magnitude, and the last peak is significantly stronger in the lower stratosphere. In our previous study on the spectral budget of kinetic energy in RCE (Chapter 2), we found upscale energy transfer from almost all horizontal scales into the mean flow, likely due to wave-mean-flow interactions (e.g. Menchaca and Durran, 2019). This net backscatter is naturally not captured by the eddy dissipation in the 4 km simulation, which is negative at all times.

In figure 3.3, the net subfilter energy transfer rate is the sum of a large amount of dissipation and backscatter. To investigate the distribution of the dissipation and backscatter, we present the normalized histogram of the subfilter energy transfer rate calculated over all grid points of the full 14-day simulation in the upper troposphere and lower stratosphere. Normalized histograms are calculated using 5000 bins with values from -10^5 to 10^5 Js^{-1}. Subfilter energy transfer rates larger than 10^5 Js^{-1} and smaller than -10^5 Js^{-1} are not included in the normalized histogram.

Similar to other studies of subfilter energy transfer rate in stratified turbulence (e.g. Khani and Porté-Agel, 2017) and isotropic turbulence (e.g. Vela-Martín, 2022), histograms of the subfilter energy transfer rate in the upper troposphere and lower stratosphere are peaked at zero (Fig. 3.6). In the upper troposphere, the histogram is relatively symmetric, with more large negative values of subfilter energy transfer rate (dissipation) than large positive values of subfilter energy transfer rate (backscatter). The average subfilter energy transfer rate in the upper troposphere is negative and close to zero. This finding underlines the fact that although the net subfilter energy transfer rate is dissipative, it is the result of a lot of regions with positive and negative values of subfilter energy transfer rate summing together (Fig. 3.6).

By contrast, in the lower stratosphere, there are more large positive values of subfilter

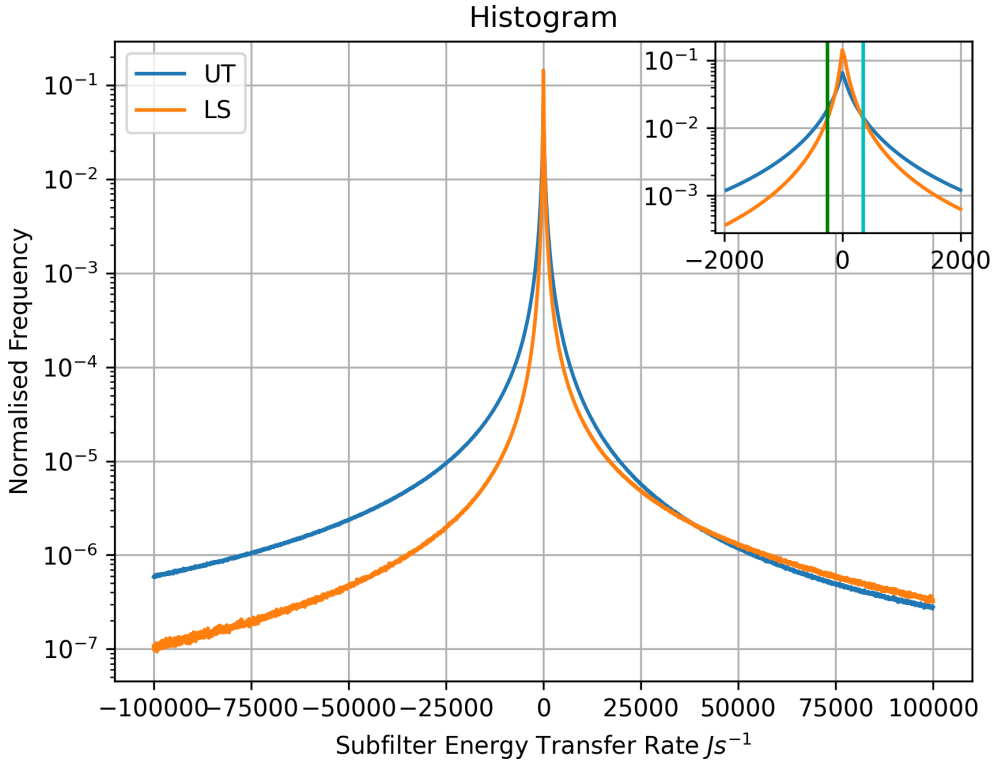


Figure 3.6: Normalized histogram of the subfilter energy transfer rate in the upper troposphere (blue) and the lower stratosphere (orange). The normalized histograms are computed with 5000 bins over -10^5 to 10^5 Js^{-1}. 99.76 % and 99.91% of points are between -10^5 to 10^5 Js^{-1} in the upper troposphere and lower stratosphere, respectively. A zoom-in plot is also provided in the top right corner of each plot. The average subfilter energy transfer rates in the upper troposphere and lower stratosphere are represented with the green and light blue vertical lines in the zoom-in plot, respectively.

energy transfer rate than large negative values of subfilter energy transfer rate (Fig. 3.6), which suggests that there are more regions with large backscatter than dissipation. The histogram in the lower stratosphere is not as symmetric as the histogram in the upper troposphere. The average subfilter energy transfer rate in the lower stratosphere is positive. This suggests that the fact that the net subfilter transfer rate is positive is not only the net result of stronger backscatter but also the net result of more points with strong backscatter than strong dissipation.

To summarize, although there is more dissipation than backscatter in the upper troposphere, and there is more backscatter than dissipation in the lower stratosphere, the net subfilter energy transfer rates in both the upper troposphere and lower stratosphere are the net result of a large amount of backscatter and dissipation. The existence of the backscatter is not represented by most subgrid turbulence mixing models. To get a better understanding of the subfilter energy transfer rate, we further decompose the subfilter energy transfer rate into six components in the following subsection.

3.3.3 Components of Subfilter Energy Transfer Rate

The subfilter energy transfer rate is the sum of six independent components, namely, P_{11}, P_{22}, P_{33}, P_{12}, P_{13} and P_{23}. To get a deeper understanding of the subfilter energy transfer rate, we identify the components to determine which terms dominate P. In the figures presented in this subsection, the diagonal components are multiplied by 2 so that the panels add up to P. The three peaks that are identified in the time series of the subfilter energy transfer rate in the upper troposphere (Fig. 3.3a), the lower stratosphere (Fig. 3.3b), the variance of TOA OLR and the negative domain-mean TOA OLR (Fig. 3.1) can also be identified in the time series of all components of the subfilter energy transfer rate in the upper troposphere (Fig. 3.7) and the lower stratosphere (Fig. 3.8). Note that even the frequency of the oscillation within the peak is similar in the time series of the variance of OLR and the time series of the components of the subfilter energy transfer rate.

Consider the time series of the six components of the subfilter energy transfer rate in the upper troposphere (Fig. 3.7). The magnitude of dissipation and backscatter are similar for all six components. The dissipation is larger than the backscatter most of the time in the upper troposphere, with the exception that the backscatter is larger than the dissipation at the top of the three peaks of P_{33}. The component P_{33} is the strongest. The magnitudes of P_{13} and P_{23} are about half of P_{33}. The magnitude of P_{11} and P_{22} is slightly weaker than P_{13}, and P_{23} and P_{12} are the weakest. The dissipation and backscatter curves are strongest in the components of the subfilter energy transfer rate that are related to the vertical

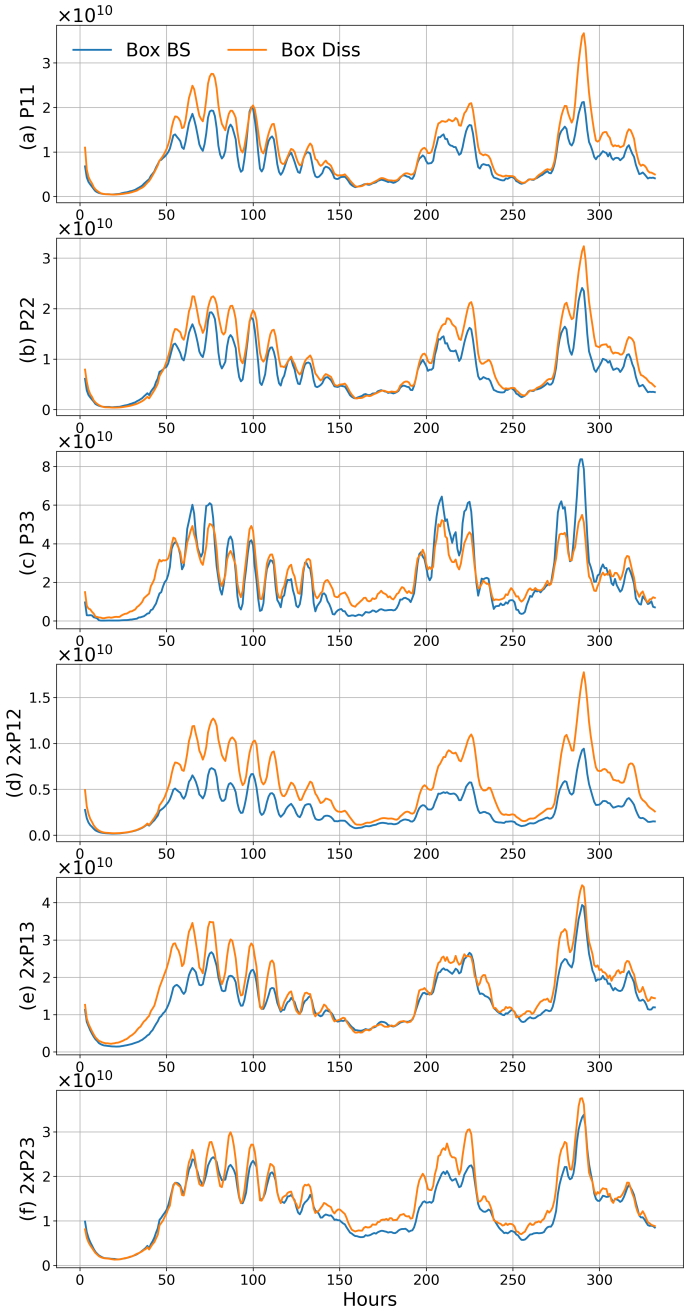


Figure 3.7: Time series of the integral of the components of subfilter energy transfer rate (P_{ij}) = (a) P_{11}, (b) P_{12}, (c) P_{13}, (d) P_{22}, (e) P_{23}, (f) P_{33} in the upper troposphere. A 6-hour moving average is used to improve readability.

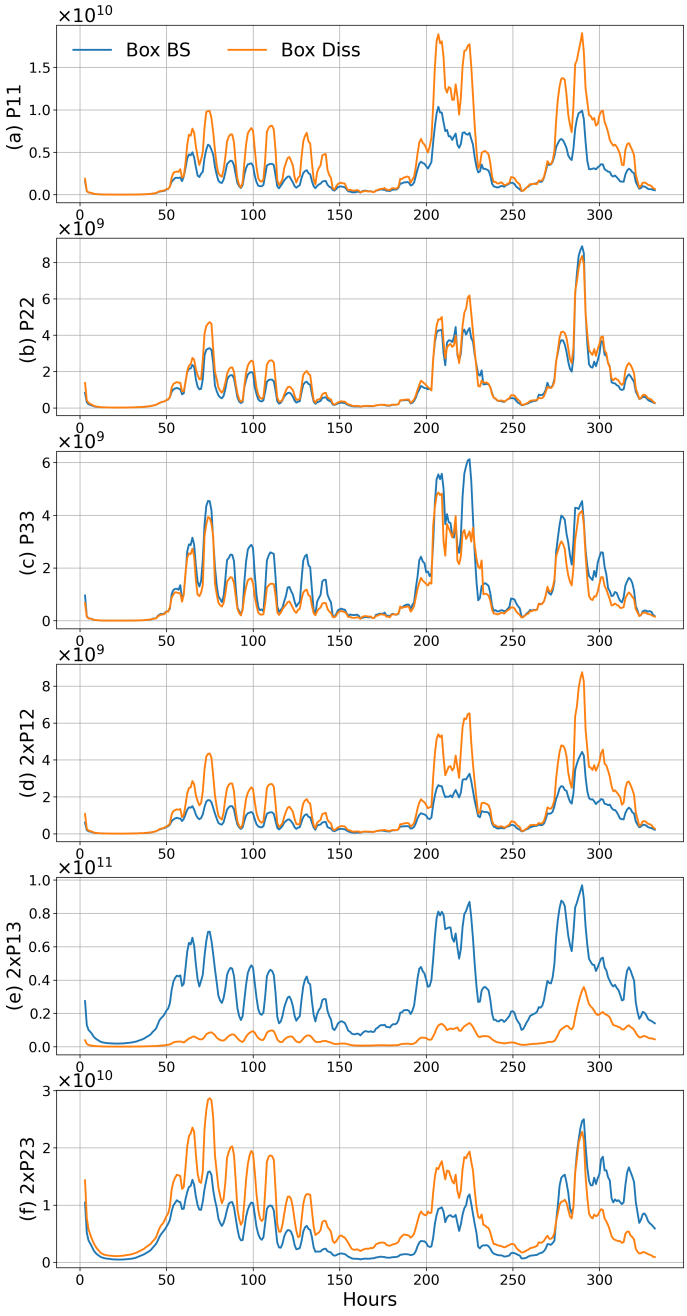


Figure 3.8: As in Fig. 3.7, but in the lower stratosphere.

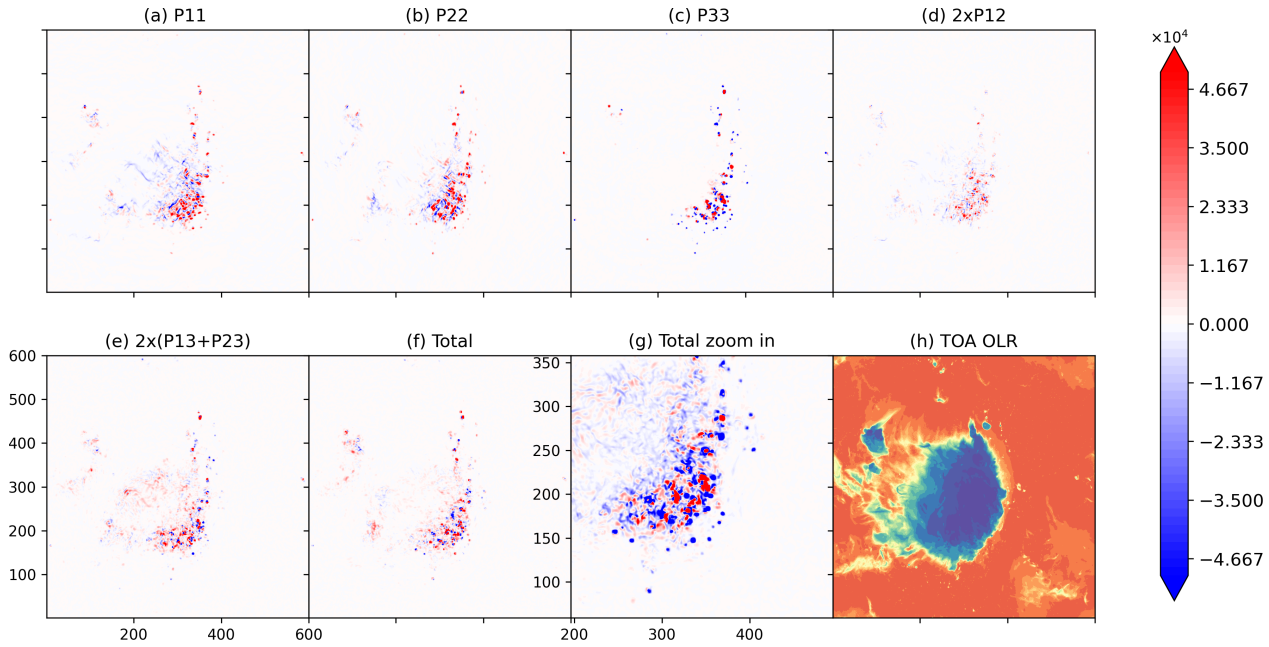


Figure 3.9: The vertically-averaged subfilter energy transfer rate with the box filter at 77 hours in the upper troposphere. The subfilter energy transfer rate P (panel g) is decomposed into component P_{ij} = (a) P_{11}, (b) P_{12}, (c) P_{13}, (d) P_{22}, (e) P_{23}, (f) P_{33}. The zoom-in plot of the total subfilter energy transfer rate (g) uses the point with the highest absolute value of subfilter transfer rate as the center to give a closer look (300 km $\times$ 300 km) to the total subfilter energy transfer rate. The TOA OLR (h) uses the same colourmap as Fig.3.2. Other than the zoom-in plot (Fig. g), all other plots show the full 600 km (x) $\times$ 600 km (y) domain.

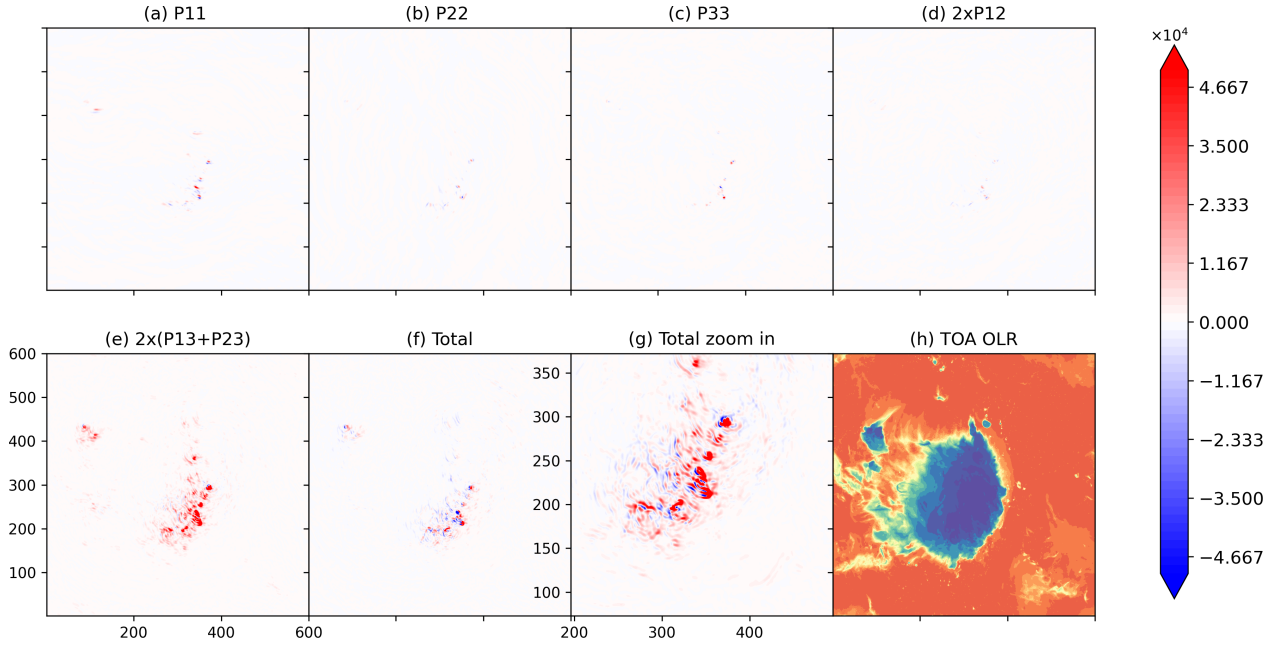


Figure 3.10: As in Fig. 3.9, but in the lower stratosphere.

direction. This finding shows that the vertical components are important in generating backscatter and dissipation. P_{33} is the energy transfer due to the subfilter vertical flux of vertical momentum by subfilter vertical motion. The fact that the dominance of the vertical terms is important is not surprising because there are no lateral forcings and RCE are balanced by sensible heat flux, latent heat release and radiation, which primarily create vertical motion, hence convective plumes. These findings are different from what was found for an idealized squall line propagating in the x (streamwise) direction, for which components related to the streamwise and shear direction are stronger than the component related to the y (spanwise) direction (Lai and Waite, 2020). This finding suggests that the dissipation and backscatter are therefore determined by the structure and dynamics of the flow.

In the lower stratosphere, the three peaks can still be identified in the time series of the components of the subfilter energy transfer rate (Fig. 3.8). By contrast with the upper troposphere, the subfilter energy transfer rate in the lower stratosphere is dominated by P_{13} rather than P_{33}. Specifically, the subfilter energy transfer rate in the lower stratosphere is dominated by the backscatter from P_{13} at all times. The dissipation in P_{13} is relatively flat throughout the whole simulation. Although the contribution of dissipation and backscatter of P_{23} is not as strong as the backscatter in P_{13}, they are still significant and the magnitudes

of the dissipation in P_{23} are about half of the backscatter of P_{13}. Dissipation dominates P_{11} at all times and dominates P_{23} at most times except towards the end of the simulation. Dissipation and backscatter have similar magnitude with P_{22} and P_{33}, they are also weaker than P_{13}, P_{11} and P_{23} in magnitude. Note that while P_{13} and P_{23} are significant in both the upper troposphere and the lower stratosphere, P_{33} is only significant in the upper troposphere but not the lower stratosphere. These results are consistent with the fact that different types of subfilter motion are present at different levels. In the upper troposphere, the convective updrafts are the dominant motion. In the lower stratosphere, there are no strong updrafts because of the stable stratification in the lower stratosphere. The updraft from the upper troposphere is inhibited from going upward, hence the shear contribution is more important.

Investigation of the dissipation and backscatter time series can help us understand the overall picture of each component of the subfilter energy transfer rate, but it cannot help us visualize the physical structure. Here, we take a closer look at one of these peaks, at 77 hours, by looking at the structures of the subfilter energy transfer rate. We have selected 77 hours for further investigation because it is at the most mature state in the aggregation event that happens between 74 hours and 80 hours. It is also a typical organized convective system in our simulation. The vertically-averaged of P_{ij} at 77 hours in the upper troposphere and lower stratosphere is plotted in figures 3.9 and 3.10, respectively. The subfilter energy transfer rate in both the upper troposphere and the lower stratosphere is close to zero over most of the domain apart from the region of reduced OLR, where there are strongly positive and negative values of subfilter energy transfer rate.

In the upper troposphere, the distributions of dissipation and backscatter are fairly random at both inside and outside the core convective region. When comparing the zoom-in plot (Fig. 3.9g) with the TOA OLR (Fig. 3.9h), one can see that strong backscatter and dissipation can be located inside the region with the lowest OLR. No coherent large-scale structures are observed in all the components of the subfilter energy transfer rate. Regions with dissipation and backscatter are distributed randomly in the domain. Inside the core, the region with the lowest OLR (highest value of subfilter energy transfer rate) has structures that are scales of 10 km. The region that is inside the core but with a slightly higher OLR has structures that are scales of 1 km and a weaker subfilter energy transfer rate. In other words, deeper clouds (lower OLR) correspond to larger structures and a stronger subfilter energy transfer rate in the upper troposphere. Note that while P_{33} is identified as the strongest component in the time series of the six component of the subfilter energy transfer rate in the upper troposphere (Fig. 3.7c), the area with strong P_{33} (Fig. 3.9c) is smaller than the area with strong subfilter energy transfer rate in other components. In other words, the strong P_{33} is concentrated in fewer points inside the core.

In the lower stratosphere, the backscatter is strong inside the core (Fig. 3.10g). The contribution from the P_{11}, P_{22}, P_{33}, and P_{12} are negligible. It is obvious that the sum of P_{13} and P_{23} is very dominant (Fig. 3.10e) and it is the main source of backscatter in the lower stratosphere. Similar to the upper troposphere, the region with the deepest clouds inside the core (lowest OLR) has larger structures than the region with a slightly higher OLR inside the core. Those structures inside the deepest clouds have sizes of about 50 km.

It has been found in Lai and Waite (2020) that the region with the most intense updraft has the most significant subfilter energy transfer rate. In contrast to the random structures found in the subfilter energy transfer rate in our work, the dissipation and backscatter found in Lai and Waite (2020) formed coherent structures. This is likely because Lai and Waite (2020) performed the subfilter energy transfer analysis in a squall line with wind shear. In this chapter, the presented simulation is an RCE simulation with no large-scale or lateral forcing. RCE creates a system of convection with many different scales interacting with each other. This may be the reason why there are less coherent spatial structures of dissipation and backscatter found in the subfilter energy transfer rate of RCE than the squall line in Lai and Waite (2020).

3.3.4 Effect of Filters

As suggested by other studies (e.g. Piomelli et al., 1991; Cardesa et al., 2015; Khani and Porté-Agel, 2017; Buzzicotti et al., 2018), changing the filter type has an impact on the subfilter energy transfer rate. As a result, we perform a study of the effect of filters on subfilter energy transfer rate by considering two more commonly used filters: the Gaussian filter and the spectral cutoff filter. The Gaussian filter is chosen because, similar to the box filter, it does not have a clear separation between the resolved scales and the subfilter scales. Unlike the box filter and the Gaussian filter, the spectral cutoff filter has a clear separation between the resolved scales and the subfilter scales. Because of that, investigation of the spectral cutoff filter will give us a different insight into the effect of filters on the subfilter energy transfer rate.

Backscatter and dissipation time series computed with the three different filters are shown in figure 3.11. The backscatter and dissipation computed with the Gaussian filter are almost identical to the results from the box filter in both the upper troposphere and lower stratosphere. However, the dissipation and backscatter computed with the cutoff filter are approximately four times stronger than those computed with the box filter and the Gaussian filter. Not surprisingly, and similar to results from the box filter, the three peaks from the variance of TOA OLR and the domain-mean TOA OLR can also be identified

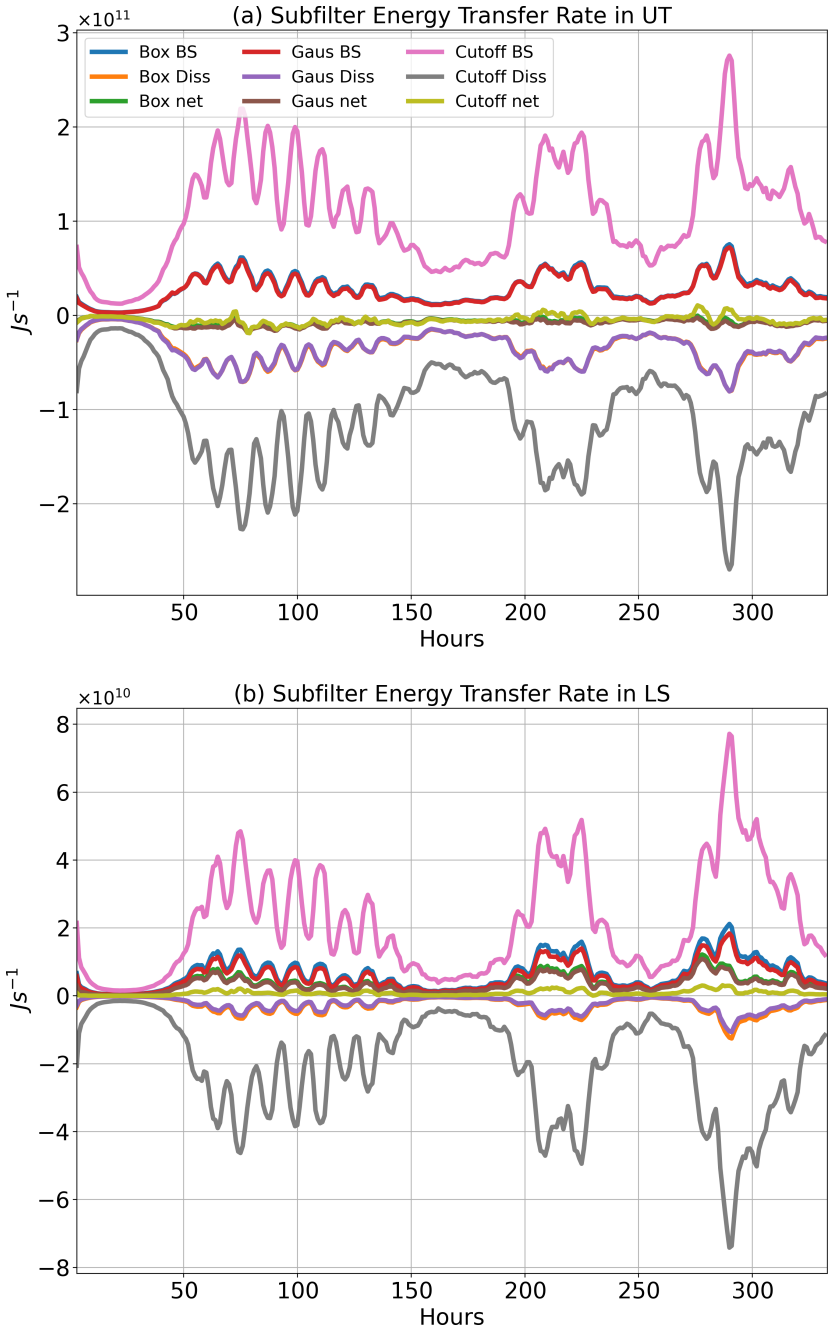


Figure 3.11: As in Fig. 3.3, but with the box filter (Box), Gaussian filter (Gaus), the spectral cutoff filter (cutoff) in the (a) upper troposphere and (b) lower stratosphere. Note that the dissipation from the 4-km non-aggregated simulation is not included in this figure.

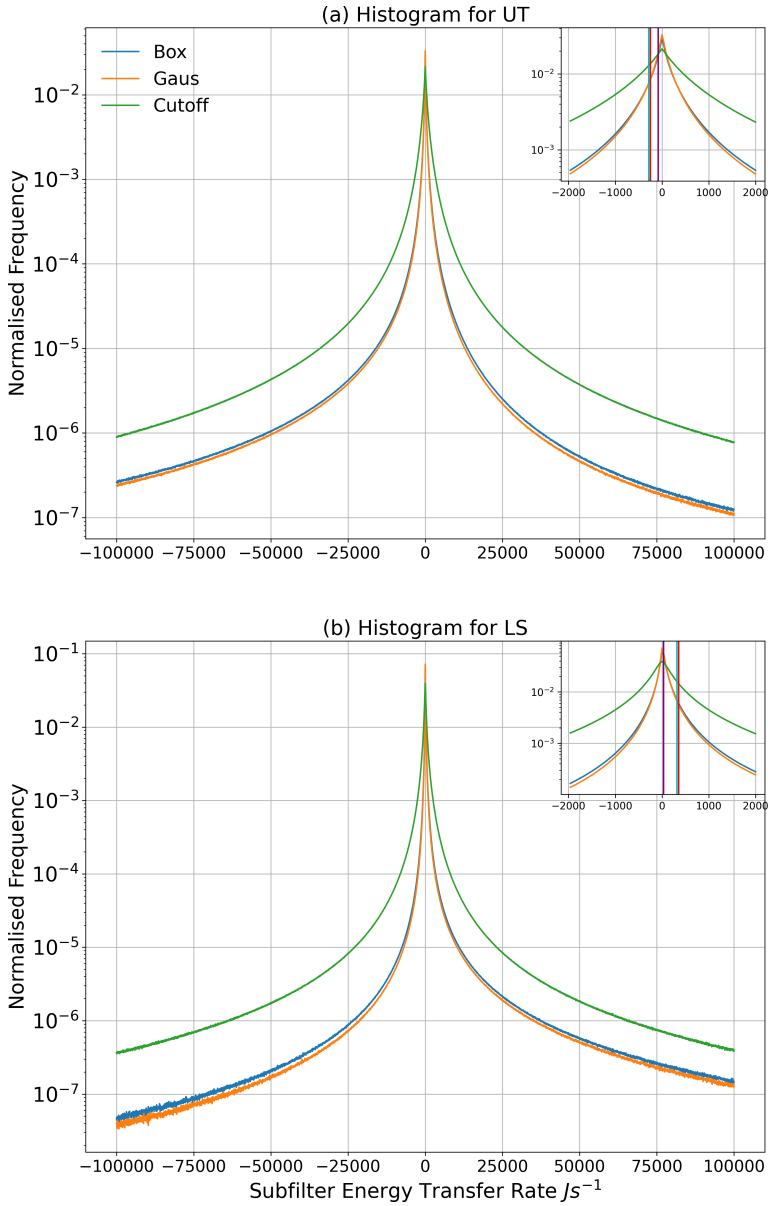


Figure 3.12: As in Fig. 3.6, but with the box filter (Box), Gaussian filter (Gaus), the spectral cutoff filter (cutoff) in (a) the upper troposphere and (b) the lower stratosphere. The average subfilter energy transfer rate of the box filter, the Gaussian filter and the spectral cutoff filter are represented with the red, light blue and purple vertical lines in the zoom-in plot, respectively. When the spectral cutoff filter is used, 99.86 % and 99.69% of points are between -10^5 to 10^5 Js^{-1} in the upper troposphere and lower stratosphere, respectively.

with the Gaussian filter and the spectral cutoff filter. The net subfilter energy transfer rate computed with the Gaussian filter and the spectral cutoff filter are the net results of a large amount of dissipation and backscatter, which is consistent with the findings from the results of the box filter. The net subfilter energy transfer rates computed by all three filters are similar in magnitude in the upper troposphere, despite the larger magnitudes of the dissipation and backscatter from the cutoff filter. The net subfilter energy transfer rate from the box filter and the Gaussian filter remain negative throughout the simulation in the upper troposphere. By contrast, the net subfilter energy transfer rate from the spectral cutoff filter is negative in the upper troposphere at most times, except at about 75 hours, 220 hours and 275 hours the net subfilter energy transfer rate is slightly positive, indicating net backscatter at these times in the upper troposphere. Those three times are also the times when the dissipation and backscatter curves are peaked. The aggregation of the convective system also peaked at those times as suggested by the variance of TOA OLR and the domain-mean OLR (Fig. 3.1). Results in the lower stratosphere are similar to the upper troposphere, except that the net subfilter energy transfer rates computed by all three filters in the lower stratosphere are positive. Unlike the net subfilter energy transfer rate in the upper troposphere, the net result of the subfilter energy transfer rate is significantly weaker for the spectral cutoff filter than the other two filters.

Histograms of the subfilter energy transfer rate computed with different filters are shown in figure 3.12. Given that the time series of the subfilter energy transfer rate of the box filter and the Gaussian filter are almost identical, it is not surprising that the histograms of the subfilter energy transfer rate for the box filter and the Gaussian filter are almost identical as well (Fig. 3.12). The histogram is significantly more symmetric with the spectral cutoff filter, with more large values of dissipation and backscatter than the box filter and the Gaussian filter, in both the upper troposphere and the lower stratosphere. Consequently, the peak of the histogram of the subfilter energy transfer rate of the spectral filter is lower than the box filter and the Gaussian filter. In other words, fewer values of subfilter energy transfer rate are close to zero with the spectral filter than with the box filter and the Gaussian filter. These findings are consistent with the fact that the backscatter and dissipation time series with the spectral cutoff filter have similar magnitudes and are significantly stronger than the dissipation and backscatter from the other two filters at all times (Fig. 3.11) in both the upper troposphere and lower stratosphere. The fact that the histogram of the subfilter energy transfer rate with the spectral cutoff filter is symmetric with more large values of dissipation and backscatter than the other two filters has also been reported (cf. Figs. 8 & 11 of Khani and Porté-Agel (2017)), where they compared the subfilter energy transfer rate with the Gaussian filter and the spectral cutoff filter in stratified turbulence. The magnitude of the dissipation and backscatter has also been

found to be significantly stronger with the spectral cutoff filter than the Gaussian filter in Piomelli et al. (1991). They explained the difference (cf. Fig.7 of Piomelli et al. (1991)) by noting that because the Gaussian filter is not a sharp filter at the filter scale, some of the subfilter energy transfer classified by the spectral cutoff filter is classified as a resolved-resolved or subfilter-subfilter energy transfer, instead of a resolved-subfilter energy transfer, by the Gaussian filter.

3.3.5 Spectral Energy Budget

To provide some context to the subfilter energy transfer shown above, we present the horizontal kinetic energy spectra and the spectral energy budget in both the upper troposphere and lower stratosphere in figure 3.13. Compared to the 4-km non-aggregated resolution kinetic energy and spectral energy budget of RCE from Chapter 2, the spectral energy budget of the 1-km simulation from this study extends to larger wavenumbers but is otherwise similar to the 4-km resolution (non-aggregated) simulation in both the upper troposphere and the lower stratosphere of the previous study. In the upper troposphere, the horizontal kinetic energy spectrum is closer to the -5/3 spectrum (Fig. 3.13a) than the horizontal kinetic energy spectrum from the non-aggregated simulation of the previous study (cf. Fig. 2.4a). The rotational and divergent kinetic energy spectra are similar in magnitude except at the small scales. At small scales, the rotational kinetic energy is stronger than the divergent kinetic energy. In the previous study, the divergent kinetic energy was marginally stronger than the rotational kinetic energy, which is the opposite of what we have in this study. The energy gain in buoyancy flux is balanced by the energy loss from the vertical flux and the transfer term is relatively weak compared to the other two terms, which is similar to the result from the previous study (Fig. 3.13c). One can see that in the non-linear energy transfer, there is a loss of energy in the largest scales and a gain in energy in the small scales, indicating that there is downscale energy transfer in the upper troposphere.

In the lower stratosphere, the horizontal kinetic energy resembles the -5/3 spectrum more closely than the lower-resolution study (non-aggregated). Similar to the previous study, the divergent kinetic energy dominates the rotational kinetic energy by a large margin (Fig. 3.13b). In the lower stratosphere, the non-linear energy transfer is balanced by the vertical energy flux and the buoyancy flux is relatively weak (Fig. 3.13d), which is again similar to the result presented in the previous study. There is a strong energy gain in the mean flow by the transfer term and a corresponding energy loss at most length scales, which suggests that there is an upscale energy transfer likely due to wave-mean-flow interactions, as shown in Chapter 2.

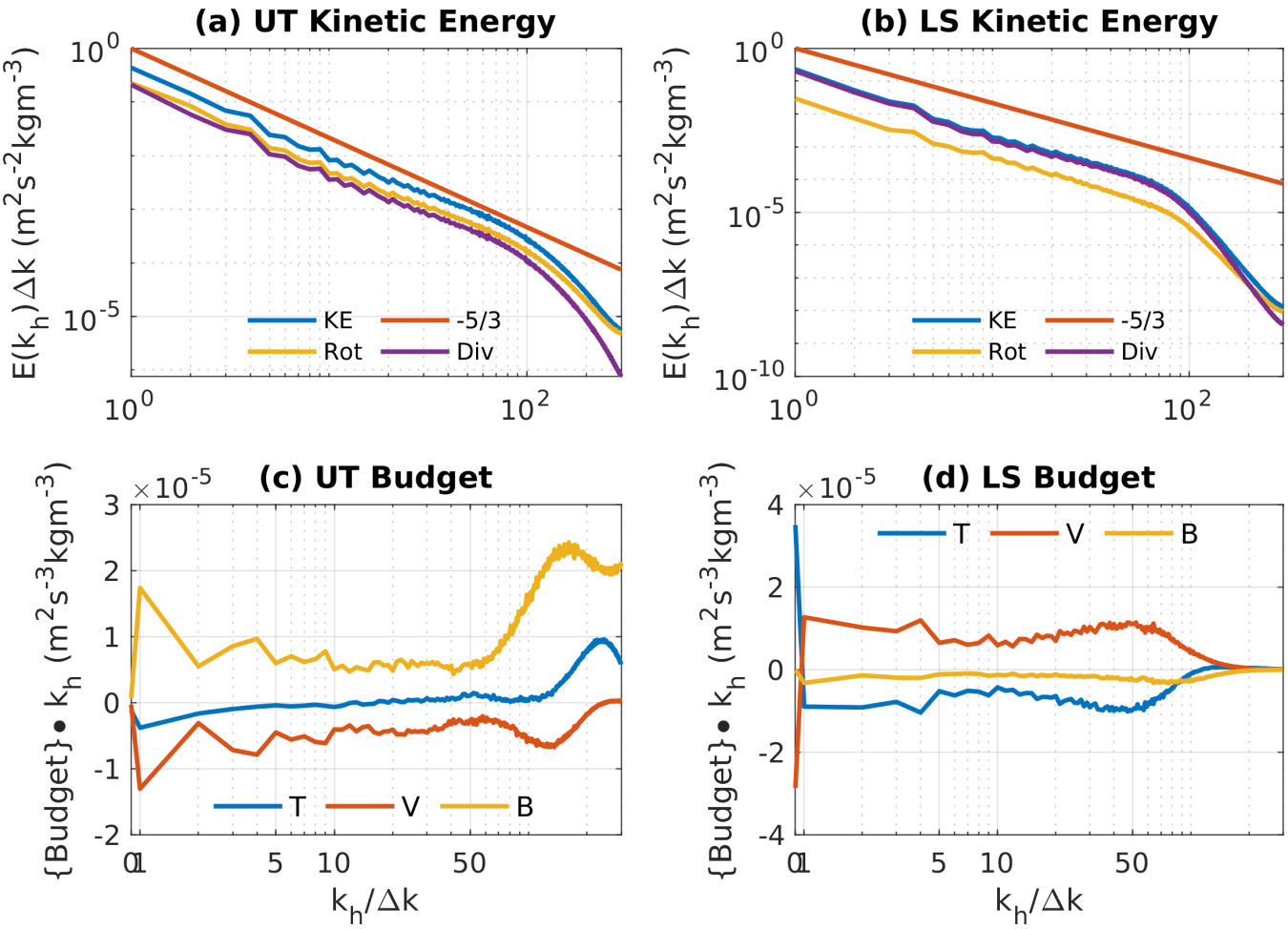


Figure 3.13: The horizontal kinetic energy spectra (a) in the upper troposphere (6-10 km) and (b) in the lower stratosphere (15.5-17 km). The horizontal kinetic energy spectra (blue) can be decomposed into rotational kinetic energy spectrum (yellow) and divergent kinetic energy spectrum (purple). The spectral energy budget (c) in the upper troposphere (6-10 km) and (d) in the lower stratosphere (15.5-17 km). The spectral budget is composed of the horizontal nonlinear energy transfer (blue), buoyancy flux (yellow), vertical energy flux divergence (red) and dissipation (not shown). All the spectra are averaged in time over the full 14-day simulation and in the vertical.

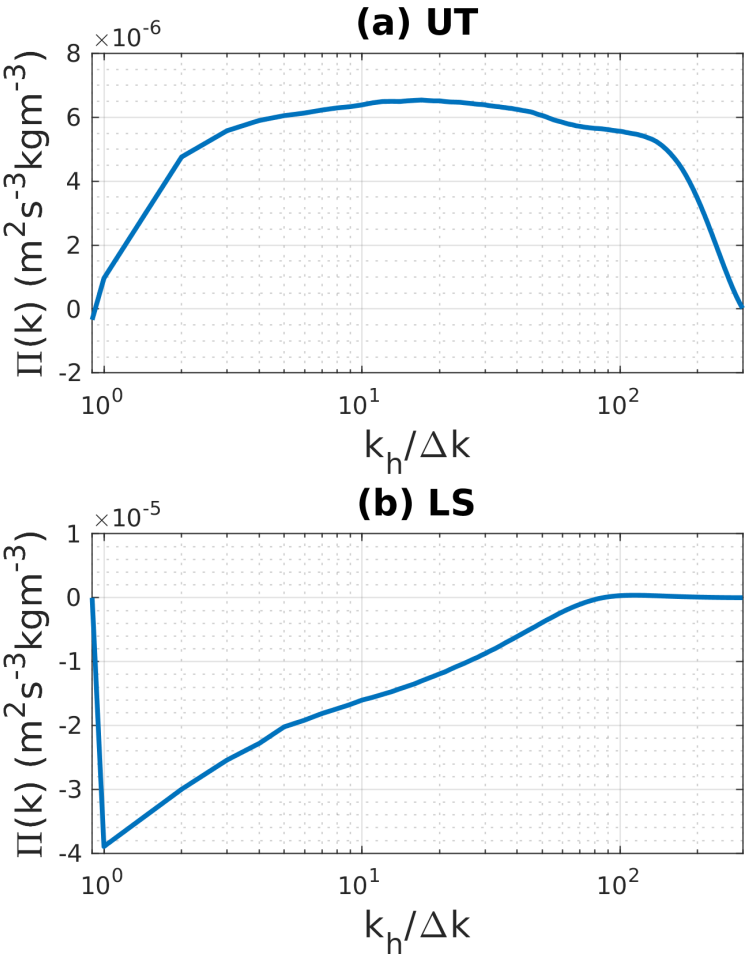


Figure 3.14: The nonlinear transfer spectral energy flux $\Pi(k)$ ($\mathrm{m^2 s^{-3} kg m^{-3}}$) for (a) the upper troposphere and (b) lower stratosphere, which are averaged in time over the full 14 days of the simulation and in the vertical.

The nonlinear spectral energy flux $\Pi(k_h, z)$ is defined as (e.g. Peng et al., 2015b)

$$\Pi(k_h, z)/\Delta k = \sum_{k \geq k_h} Re(T(k, z)), \tag{3.8}$$

where $\Delta k = 2\pi/L$ and $L = 600$ km. The value of nonlinear spectral energy flux indicates the direction of the energy transfer. If the nonlinear spectral energy flux is positive (negative), there is a direct (inverse) or downscale (upscale) energy cascade/transfer. For isotropic turbulence, the spatial-averaged subfilter energy transfer rate with spectral cutoff filter size of r is equal to the nonlinear spectral energy flux at dimensionalized wavenumber $k = \pi/r$ (e.g. Cardesa et al., 2015). While the flow presented in this study is not isotropic turbulence, $\Pi(\pi/r, z)$ corresponds to the rate at which kinetic energy is transferred downscale past wavenumber π/r, suggesting a correspondence between P and Π at the filter scale. Hence, we perform an investigation of nonlinear spectral energy flux analysis, to which the subfilter energy transfer rate with the cutoff filter will be compared. Similar to the finding from Chapter 2, the nonlinear spectral energy flux is positive at all scales in the upper troposphere (Fig. 3.14a), which suggests that there is a direct energy cascade in the upper troposphere. In contrast to the upper troposphere, in the lower stratosphere the nonlinear spectral energy flux is negative from the smallest wavenumber, which corresponds to a scale of 600 km, to $k = 80$, which corresponds to a scale of 7.5 km. This finding suggests that there is an inverse energy transfer from scales of 600 km to 7.5 km. For $k > 80$, the nonlinear spectral energy flux is slightly positive, which suggests that there is a direct energy cascade at scales smaller than 7.5 km. Negative nonlinear spectral energy flux at the non-dimensionalized cutoff wavenumber $k_c = 75$ is consistent with the net backscatter found across the filter scale of 4 km in the lower stratosphere. The non-dimensionalized cutoff wavenumber of $k_c = 75$ corresponds to the filter scale of 4 km. From (3.5), the cutoff wavenumber is given by π/Δ, where $\Delta = 4$ km when the filter scale is 4 km. To nondimensionalized the cutoff wavenumber, one should multiply the dimensionalized wavenumber by $L/2\pi$. For $\Delta = 4$ km, the corresponding cutoff wavenumber $k_c = (\pi/\Delta)(L/2\pi) = 75$ (cf. eq. 2 of Cardesa et al., 2015). The Gaussian filter and the box filter are not sharp filters at the filter scale. As a result, the spatial-averaged subfilter energy transfer rate with the box or Gaussian filter does not have to be equal to the nonlinear spectral energy flux.

3.4 Conclusions

In this work, a priori analysis of the subfilter energy transfer rate in an idealized non-aggregated RCE simulation at a horizontal scale of 4 km is performed by filtering a 1-km-

resolution simulation to the resolution of 4 km. The effects of three filters, the box filter, the Gaussian filter and the spectral cutoff filter, are presented for comparison.

The fluctuation of the time series of the dissipation and backscatter aligns well with the time series of the variance of TOA OLR and the negative domain-mean TOA OLR, which are proxies for aggregation. Dissipation and backscatter are enhanced when the simulation is more aggregated and reduced when it is less aggregated. The dissipation in the 4-km non-aggregated simulation is weak when compared to the subfilter energy transfer rate of the 1-km simulation. The net subfilter energy transfer rate is negative in the upper troposphere, which suggests that the subfilter energy transfer is dissipative in the upper troposphere. However, the net subfilter energy transfer rate is positive in the lower stratosphere, which suggests that there is net backscatter in the lower stratosphere. In both the upper troposphere and lower stratosphere, the net subfilter energy transfer rates are the net result of a large amount of dissipation of backscatter throughout the whole domain. Strong dissipation and backscatter can be identified in regions with low TOA OLR, which suggests that the subfilter energy transfer rate is associated with deep clouds. The vertical and the vertical shear components $(i, j) = (1, 3), (2, 3)$ and $(3, 3)$ of the subfilter energy transfer rate are dominating terms in the upper troposphere. This is likely because there is no large-scale lateral forcing in our simulation. RCE is primarily driven by convection, which is mainly in the vertical direction. The vertical shear components $(i, j) = (1, 3), (2, 3)$ of the subfilter energy transfer rate are the dominating terms in the lower stratosphere. The fact that the component $(i, j) = (3, 3)$ of the subfilter energy transfer rate in the lower stratosphere is not as significant as in the upper troposphere can be explained by the fact that updrafts are inhibited in the lower stratosphere. The subfilter energy transfer rate from the box filter and the Gaussian filter are almost identical. The dissipation and backscatter computed with the spectral cutoff filter are four times stronger than the dissipation and backscatter computed by the box filter and the Gaussian filter, which can be explained by the fact that both the box filter and the Gaussian filter are not sharp filters (Piomelli et al., 1991). While the spectral cutoff filter may not have a problem with the cutoff scales, it may create oscillation.

The kinetic energy spectra in both the upper troposphere and the lower stratosphere resemble the -5/3 spectra in this study, which is different from Chapter 2. Compared to the previous study, the increase in resolution does not lead to a dramatic change in the spectral energy budget in both the upper troposphere and lower stratosphere. In the upper troposphere, the energy is gained by the buoyancy flux, and it is balanced by the energy loss in the vertical flux. The transfer term is weak at most scales, except that there is an energy loss in the mean flow and an energy gain in the scales smaller than 6 km. In the lower stratosphere, the energy gain in the vertical flux is balanced by the energy loss

from the transfer term at most scales, except at the mean flow. The buoyancy flux is weak in the lower stratosphere. There is a direct energy transfer from the large scales to the scales smaller than approximately 6 km in the upper troposphere. There is an inverse energy transfer into the mean flow in the lower stratosphere. The results from the budget are consistent with the results from the subfilter energy transfer rate in both the upper troposphere and the lower stratosphere.

In conclusion, at scales of approximately 4 km, which is the resolution of some cloud-resolving simulations (e.g. Wing and Emanuel, 2014; Peng et al., 2014; Lai and Waite, 2023), the subfilter energy transfer consists of a large amount of backscatter and dissipation. This backscatter is not represented by commonly used dissipative-only subgrid turbulence mixing schemes such as the Smagorinsky turbulence model. In the lower stratosphere, the backscatter dominates. As a result, there is a need to include the backscatter in subgrid turbulence models to improve the performance of convective-permitting simulations of convectively driven flows at these scales. The lack of subgrid backscatter in a subgrid turbulence scheme will lead to an inaccurate representation of the local subgrid energy transfer, which may result in less realistic predictions at small scales.

4

A Backscatter-Allowing Stochastic Subgrid Turbulence Scheme

4.1 Introduction

Commonly-used eddy viscosity schemes are designed to be dissipative. However, a priori analysis has suggested that while subfilter energy transfer is dissipative on average, backscatter, the subfilter energy transfer from the subgrid scales to the resolved scales, exists in a local sense (e.g. Piomelli et al., 1991). Moreover, a priori analysis of subfilter turbulence in direct numerical simulation (e.g. Khani and Porté-Agel, 2017) and high-resolution large eddy simulations (e.g. Lai and Waite, 2020) suggested that backscatter and dissipation are both significant. As a result, it may be beneficial to represent backscatter in a subgrid turbulence mixing scheme. This can be done in a deterministic fashion. For example, Kirkil et al. (2012) performed a large eddy simulation with a range of subgrid mixing schemes in WRF, from a relatively simple Smagorinsky scheme to more complex backscatter-allowing schemes such as the Lagrangian-averaged scale-dependent dynamic (LASD) model, nonlinear backscatter and anisotropy model (NBA) and dynamic reconstruction models (DRM). While the simulation time with LASD and DRM took 25-28% longer than the Smagorinsky scheme, they were more accurate than the Smagorinsky scheme. While backscatter-allowing deterministic subgrid turbulence schemes can address the issue of backscatter in traditional purely dissipative eddy viscosity models, they lack stochastic components. Backscatter and dissipation are often randomly distributed (e.g. Khani and Waite, 2016). Still, there are also connections to large-scale structure, as seen in Lai and Waite (2020). As a result, adding a stochastic process is a natural way to give

randomness to a subgrid model.

Stochastic parameterizations in weather forecasting models are not a new idea. They are widely used in representing model uncertainties in operational weather forecasting (e.g. Palmer et al., 2009). There are two approaches to adding stochasticity to forecast models: stochastic perturbed parameterization tendencies (SPPT) and stochastic backscatter parameterization. SPPT originated from Buizza et al. (1999), in which a scheme that perturbs horizontal wind, temperature, and humidity with a uniformly distributed multiplicative noise was introduced. A revised scheme based on Buizza et al. (1999), SPPT (Palmer et al., 2009), which uses the auto-regressive processes of first order to generate the random noise, was proposed. To improve a deterministic backscatter scheme, adding stochastic components is beneficial. Stochastic backscatter parameterization combines the idea of backscatter and stochastic parameterization. Stochastic backscatter subgrid scale scheme in LES was first proposed by Leith (1990) and Mason and Thomson (1992). Leith (1990) modified the Smagorinsky scheme by adding a stochastic backscatter acceleration to the rotational component by using a vector potential. Shutts (2005) used the dissipation to create a random horizontal streamfunction, the random pattern of which was generated by cellular automata. The stochastic backscatter scheme by Shutts (2005) improved the mesoscale -5/3 energy spectrum in the ECMWF model.

Berner et al. (2009) modified the Shutts (2005) scheme and proposed the spectral stochastic backscatter scheme (SPBS). Similar to the Shutts scheme, SPBS adds stochastic backscatter forcing to the rotational component of the wind. Unlike in the Shutts scheme, where the random streamfunction is generated by cellular automaton (Shutts, 2005), the random streamfunction perturbation in SPBS is generated by a first-order autoregressive process (Berner et al., 2009), also known as AR1. The backscatter rate in SPBS is determined by the instantaneous dissipation rate. SPBS created kinetic energy spectra that were more realistic, and it also predicted rainfall more accurately. Berner et al. (2011) implemented the stochastic kinetic energy backscatter scheme (SKEBS) in WRF. SKEBS is a simplified version of SPBS, which is designed for shorter time scales and mesoscale convective systems (Berner et al., 2011). Instead of using the instantaneous dissipation rate to calculate the backscatter rate (SPBS), the backscatter rate is set to constant (SKEBS) for simplicity. The use of a constant backscatter rate was shown to be on par with the backscatter rate calculated by the instantaneous dissipation rate (e.g. Berner et al., 2009, 2011).

While there are other methods for incorporating stochasticity into subgrid turbulence mixing models, they can be complicated to implement and computationally expensive. A simpler approach is to add a stochastic perturbation to an existing subgrid turbulence scheme. Marstorp et al. (2007) proposed a stochastic backscatter Smagorinsky scheme

which allows backscatter. The proposed scheme adds zero-mean random perturbation to the eddy viscosity of the Smagorinsky subgrid turbulence scheme. The proposed scheme improves the -5/3 kinetic energy spectrum and the enstrophy spectrum at the smaller scales over the traditional Smagorinsky scheme in decaying isotropic turbulence. It is a known issue that the Smagorinsky scheme is overly dissipative (e.g. Lai and Waite, 2020). As a result, adding a zero-mean stochastic forcing to the eddy viscosity may not solve the fact that, on average, the Smagorinsky scheme is overly dissipative.

In this chapter, two different stochastic methods for representing backscatter in WRF will be tested. In particular, the subgrid energy transfer rate and the spectral energy budget analysis will be performed for comparison. The two stochastic methods are the SKEBS scheme (Berner et al., 2011) and a scheme that is newly developed and implemented in WRF called the stochastic backscatter TKE subgrid turbulence scheme. The stochastic backscatter TKE scheme is inspired by the stochastic backscatter Smagorinsky scheme from Marstorp et al. (2007). The author implemented the stochastic backscatter TKE subgrid turbulence scheme by adding a zero-mean stochastic forcing to the horizontal eddy viscosity of the TKE subgrid turbulence mixing scheme. Details of the SKEBS scheme and the stochastic backscatter TKE scheme will be introduced in section 4.2.1-4.2.4. The details of all the simulations presented in this chapter will be given in section 4.2.5. The diagnostics in this chapter will be given in section 4.2.6. Results and discussions are given in section 4.3. The conclusions for this chapter will be given in section 4.4.

4.2 Methodology

4.2.1 Stochastic Differential Equation - Wiener Process

Before describing the red noise used in our stochastic backscatter model, we first review the Wiener process. The Wiener process is a model that describes the position of particles in Brownian motions (e.g. Lemons, 2002; Scott, 2024). Note that the following three properties are conditions that a Wiener process $W(t)$ over $[0, T]$ has to satisfy (Higham, 2001).

1. $W(0) = 0$
2. For $0 \leq t_1 \leq t_2 \leq T$, $W(t_2) - W(t_1) \sim \sqrt{t_2 - t_1} N(0, 1)$
3. For $0 \leq t_1 \leq t_2 \leq t_3 \leq t_4 \leq T$, $W(t_2) - W(t_1)$ and $W(t_4) - W(t_3)$ are independent,

where $X \sim N(0,1)$ means that the quantity X has a normal distribution with a mean of 0 and a variance of 1. According to the second property of the Wiener process listed above, we know that

$$(W(t+\Delta t) - W(t)) \sim N(0,1)\sqrt{\Delta t}.$$

The Wiener process $W(t)$ can also be expressed in differential form as following (e.g. Lemons, 2002):

$$dW(t) = N(0,1)\sqrt{dt}. \tag{4.1}$$

4.2.2 Stochastic Differential Equation - Ornstein–Uhlenbeck Process

The Ornstein–Uhlenbeck process (OU process) is used to perturb the eddy viscosity of the proposed stochastic backscatter TKE scheme. It will be beneficial to have a deeper understanding of the OU process. The OU process originated as a model that describes the velocity of particles with viscous drag and a random forcing using Newton's second law (e.g. Lemons, 2002; Scott, 2024). The governing equation of OU process (cf. Ch.7 of Lemons, 2002) is given by

$$\begin{aligned} dV(t) &= -\gamma V(t)dt + \kappa dW & (4.2)\\ &= -\gamma V(t)dt + \kappa N(0,1)\sqrt{dt}, & (4.3) \end{aligned}$$

where γ is the viscous drag constant and κ is the standard deviation of the random forcing. It is easy to recognize that the governing equation for the mean of $V(t)$ is

$$\frac{d\langle V(t)\rangle}{dt} = -\gamma\langle V(t)\rangle,$$

where $\langle V(t)\rangle$ is the mean of $V(t)$ and solving it will give

$$\langle V(t)\rangle = \nu_0 e^{-\gamma t}, \tag{4.4}$$

where $\nu_0 = \langle V(0)\rangle$ is the initial condition. Similarly, one can obtain the governing equation for $\langle V(t)^2\rangle$ (Lemons, 2002). The variance is

$$\begin{aligned} \mathrm{var}(V(t)) &= \langle V(t)^2\rangle - \langle V(t)\rangle^2 & (4.5)\\ &= \left(\frac{\kappa^2}{2\gamma}\right)(1 - e^{-2\gamma t}). & (4.6) \end{aligned}$$

In order to implement the OU process for numerical simulations, it is necessary to obtain the equation for time stepping (Lemons, 2002). Consider t goes from $t = 0$ to $t = \Delta t$,

$$V(\Delta t) = N_0^{\Delta t}\left(V(0)e^{-\gamma\Delta t}, \left(\frac{\kappa^2}{2\gamma}\right)(1 - e^{-2\gamma\Delta t})\right) \tag{4.7}$$

$$= V(0)e^{-\gamma\Delta t} + N_0^{\Delta t}\left(0, \left(\frac{\kappa^2}{2\gamma}\right)(1 - e^{-2\gamma\Delta t})\right), \tag{4.8}$$

where $N_{t=a}^{t=b}(0,1)$ represents a random number with the standard normal distribution (with mean of 0 and variance of 1) when time stepping from $t = a$ to $t = b$. Similarly, we further advance one step from $t = \Delta t$ to $t = 2\Delta t$,

$$V(2\Delta t) = V(\Delta t)e^{-\gamma\Delta t} + N_{\Delta t}^{2\Delta t}\left(0, \left(\frac{\kappa^2}{2\gamma}\right)(1 - e^{-2\gamma\Delta t})\right). \tag{4.9}$$

Now, we generalize the idea from the previous time stepping and obtain the time stepping formula for the OU process when t goes from $t = t$ to $t = t + \Delta t$,

$$V(t + \Delta t) = V(t)e^{-\gamma\Delta t} + N_t^{t+\Delta t}\left(0, \left(\frac{\kappa^2}{2\gamma}\right)(1 - e^{-2\gamma\Delta t})\right). \tag{4.10}$$

The OU process is a continuous-time analogue of the first-order autoregressive (AR1), which is a discrete-time process. The AR1 process will be used in SKEBS and the stochastic backscatter scheme. More details of the AR1 process will be given in the next two subsections.

4.2.3 Technical Details for SKEBS

Different stochastic parameterizations have also been implemented in WRF. The stochastic kinetic energy backscatter scheme (SKEBS) is created by combining the ideas of stochastic forcing and backscatter. The details of the implementation of SKEBS in WRF can be found in Berner (2013). The idea of SKEBS is that a streamfunction forcing with a prescribed spatial spectrum will be created to provide the backscatter. Hence, only the rotational component of the 2D wind will be perturbed.

Following the notation used in Berner (2013), the streamfunction forcing $\psi'(x, y, t) = \frac{\partial\psi}{\partial t}$ gives the zonal wind forcing $u'(x, y, t)$ and meridional wind forcing $v'(x, y, t)$:

$$u'(x, y, t) = -\frac{\partial\psi'(x, y, t)}{\partial y}, \tag{4.11}$$

$$v'(x, y, t) = \frac{\partial\psi'(x, y, t)}{\partial x}. \tag{4.12}$$

The corresponding two-dimension Fourier transformed streamfunction ψ_{kl} satisfies

$$\psi(x,y,t) = \sum_{k=-K_X/2}^{K_X/2} \sum_{l=-K_Y/2}^{K_Y/2} \psi_{kl}(t) e^{2\pi i(kx/L_X + ly/L_Y)}, \tag{4.13}$$

where k and l are the dimensionless (integer) zonal and meridional wavenumbers, respectively.

To obtain the rate of kinetic energy perturbation, there are two important facts to know.

1. The streamfunction at the next time step $t + \Delta t$ is given by

$$\psi_{kl}(t + \Delta t) = \psi_{kl}(t) + S_{kl}\Delta t + \psi'_{kl}(t), \tag{4.14}$$

where S_{kl} is the spectral source term due to advection, diffusion and physical parameterization (Berner, 2013). Note that the source term is not correlated with the streamfunction perturbation. SKEBS further simplifies the problem by assuming that all spectral source terms are negligible. As a result,

$$\langle \psi_{kl}(t + \Delta t)\psi'_{kl}(t + \Delta t)\rangle = \langle \psi_{kl}(t)\psi'_{kl}(t + \Delta t)\rangle + \langle \psi'_{kl}(t)\psi'_{kl}(t + \Delta t)\rangle, \tag{4.15}$$

where $\langle \psi_{kl}(t)\rangle$ represents the mean of $\psi_{kl}(t)$

2. SKEBS forcing is given as an AR1 process:

$$\psi'_{kl}(t + \Delta t) = (1 - \alpha_{SKEBS})\psi'_{kl}(t) + g_{kl}\sqrt{\alpha_{SKEBS}}\epsilon_{kl}(t), \tag{4.16}$$

where α_{SKEBS} is a constant, g_{kl} is the noise amplitude, and ϵ_{kl} is a complex Gaussian white noise with mean equals to zero and variance equals to σ. In SKEBS,

$$\alpha_{SKEBS} = \Delta t/\tau, \tag{4.17}$$

where τ is the decorrelation time, and the wavenumber-dependent amplitude of the noise is defined by using the power-law:

$$g_{kl} = b(k^2/L_X^2 + l^2/L_Y^2)^{\beta_{SKEBS}/2}, \tag{4.18}$$

where the value of β_{SKEBS} will be set based on the -5/3 energy spectrum. Note that to be consistent to the notation (Berner, 2013) and avoid confusion, α_{SKEBS} and β_{SKEBS} are used in the SKEBS scheme, which is different from the α and β used in

the time-stepping formula for an OU process (4.26) and stochastic backscatter TKE scheme (4.30) in the previous subsection.

The variance of this AR1 process can be calculated by using (4.29):

$$\mathrm{var}(\psi'_{kl}(t)) = \langle \psi'_{kl}(t)\psi'^{*}_{kl}(t)\rangle = \frac{g_{kl}^2\sigma^2}{2-\alpha_{SKEBS}}.$$

3. Since $\langle \psi_{kl}(t)\epsilon_{kl}(t)\rangle = 0$ and $\langle \psi'_{kl}(t)\epsilon_{kl}(t)\rangle = 0$, one can substitute (4.16) into (4.15) to obtain

$$\langle \psi_{kl}(t+\Delta t)\psi'_{kl}(t+\Delta t)\rangle = (1-\alpha_{SKEBS})\langle \psi_{kl}(t)\psi'_{kl}(t)\rangle + \langle \psi'_{kl}(t)\psi'_{kl}(t)\rangle \tag{4.19}$$

Note that since AR1 is a stationary process, $\langle \psi_{kl}(t+\Delta t)\psi'_{kl}(t+\Delta t)\rangle = \langle \psi_{kl}(t)\psi'_{kl}(t)\rangle$ and

$$\langle \psi_{kl}(t)\psi'_{kl}(t)\rangle = \left(\frac{1}{\alpha_{SKEBS}} - 1\right)\langle \psi'_{kl}(t)\psi'_{kl}(t)\rangle \tag{4.20}$$

The rate of change of horizontal kinetic energy E'_{kin} is given by

$$E'_{kin} = \frac{2\pi^2}{\Delta t}\sum_{k=-K_X/2}^{K_X/2}\sum_{l=-K_Y/2}^{K_Y/2}(k^2/L_X^2 + l^2/L_Y^2)\langle |\psi_{kl}(t+\Delta t)|^2 - |\psi_{kl}(t)|^2\rangle \tag{4.21}$$

$$= \frac{2\pi^2}{\Delta t}\sum_{k=-K_X/2}^{K_X/2}\sum_{l=-K_Y/2}^{K_Y/2}(k^2/L_X^2 + l^2/L_Y^2)\langle 2|\psi_{kl}(t)\psi'_{kl}(t)| + |\psi'_{kl}(t)|^2\rangle \tag{4.22}$$

$$= \frac{2\pi^2}{\Delta t}\sum_{k=-K_X/2}^{K_X/2}\sum_{l=-K_Y/2}^{K_Y/2}(k^2/L_X^2 + l^2/L_Y^2)\left(\frac{2}{\alpha_{SKEBS}} - 1\right)\langle |\psi'_{kl}(t)|^2\rangle \tag{4.23}$$

$$= 2\pi^2\sigma^2\tau\sum_{k=-K_X/2}^{K_X/2}\sum_{l=-K_Y/2}^{K_Y/2}(k^2/L_X^2 + l^2/L_Y^2)^{\beta_{SKEBS}+1}b^2. \tag{4.24}$$

We can define the parameter b in terms of E'_{kin}:

$$b^2 = \frac{E'_{kin}\alpha_{SKEBS}}{2\pi^2\sigma^2\sum_{k=-K_X/2}^{K_X/2}\sum_{l=-K_Y/2}^{K_Y/2}(k^2/L_X^2 + l^2/L_Y^2)^{\beta_{SKEBS}+1}}, \tag{4.25}$$

where E'_{kin} is the backscatter rate of the streamfunction, which is assumed to be constant.

4.2.4 Stochastic Backscatter TKE scheme

A new subgrid scale model called stochastic backscatter TKE scheme will be proposed in this subsection. The stochastic backscatter TKE scheme is inspired by the stochastic backscatter Smagorinsky scheme from Marstorp et al. (2007). The idea of the stochastic backscatter TKE scheme is that backscatter can be added by using a stochastic forcing to the horizontal eddy viscosity from the standard TKE scheme. We are modifying Marstorp et al. (2007) approach to the TKE scheme for numerical weather prediction models.

The AR1 process used in the stochastic backscatter TKE scheme is created by setting $\kappa^2/2\gamma = 1$ and $\gamma = 1/\tau$ in (4.10). As a result, the time-stepping formula for the stochastic forcing is

$$G(\boldsymbol{x}, t_n) = \alpha G(\boldsymbol{x}, t_{n-1}) + \beta g(\boldsymbol{x}, t_n), \tag{4.26}$$

where $\alpha = \exp(-\Delta t/\tau)$, $\beta^2 = 1 - \alpha^2$, τ is the relaxation time scale, and $g(\boldsymbol{x}, t_n)$ is Gaussian white noise with mean of 0 and variance of 1. The mean of this process is zero. Note that the OU process is stationary, which means that the autocorrection function $B(t_1, t_1) = \langle V(t_1)V(t_2)\rangle$ will only depend on the time difference, ie. $B(t_1, t_2) = B(t_1 - t_2)$ (cf. section 2.2 of Scott, 2024). Hence, the variance of the OU process is constant. The variance for $\text{var}(G(\boldsymbol{x}, t_n))$ is

$$\text{var}(G(\boldsymbol{x}, t_n)) = \alpha^2 \text{var}(G(\boldsymbol{x}, t_{n-1})) + \text{var}(\beta g(\boldsymbol{x}, t_n)) \tag{4.27}$$

$$\text{var}(G(\boldsymbol{x}, t_n)) = \alpha^2 \text{var}(G(\boldsymbol{x}, t_n)) + \beta^2 \tag{4.28}$$

$$\text{var}(G(\boldsymbol{x}, t_n)) = \frac{\beta^2}{1 - \alpha^2}. \tag{4.29}$$

Since $\beta^2 = 1 - \alpha^2$, the variance of $G(\boldsymbol{x}, t_n)$ is 1.

In the simulations with the proposed stochastic backscatter scheme, the stochastic horizontal eddy viscosity is defined by (Skamarock et al., 2008)

$$K_h^S = C_k(1 + aG(\boldsymbol{x}, t))\Delta_h\sqrt{e}, \tag{4.30}$$

where $C_k = 0.15$ is the default constant for the standard TKE subgrid turbulence mixing scheme, and e is the turbulence kinetic energy calculated by a prognostic equation in the TKE subgrid turbulence mixing scheme. The function G the function given by (4.26)

For consistency with the previous chapter, since backscatter was diagnosed with horizontal filtering, the addition of stochastic forcing only applies to the horizontal eddy viscosity for momentum mixing. Since the TKE equation has an eddy viscosity in it, the perturbed eddy viscosity also directly affects the evolution of e. There are no changes to the eddy viscosity used for mixing scalars.

4.2.5 Model

The Advanced Research Weather Research and Forecasting Model (WRF) is used for this chapter (Skamarock et al., 2008). WRF solves the fully compressible nonhydrostatic Euler equations. WRF uses a third-order Runge-Kutta time-stepping scheme. For the advection scheme, WRF uses a fifth-order scheme in the horizontal directions and a third-order scheme in the vertical direction. A terrain-following hydrostatic pressure coordinate is used as the vertical coordinate.

There will be a total of seven simulations that will be discussed in this chapter. The setup for all the simulations are the same as those from Chapters 2 and 3 except the use of different resolution and subgrid turbulence schemes. Here are the details of the simulations. They are created by modifying the radiative-convective equilibrium test case from WRF. The sea surface temperature is set to be 302K. RRTMG longwave and shortwave radiation schemes are used (Iacono et al., 2008). The diurnal cycle is removed, and the incoming solar radiation is set to be 434.12 W/m^2, which corresponds to a zenith angle of 50.5 degrees (Holloway and Woolnough, 2016). Thompson microphysics scheme is used (Thompson et al., 2008). A periodic boundary condition is used in the horizontal directions. No rotation and no planetary boundary layer schemes are used in the simulations. At the top of the domain, 5-km Rayleigh damping layer with the coefficient of 0.003 s^{-1} is used. The domain has size of $L_X \times L_Y \times H$, where L_X = 600 km, L_Y = 600 km, and H =25 km. All the simulations are run for 14 days. Similar to the simulation from Chapter 3, the initial condition of all the simulations is given by the last output of a 63-day spin-up non-aggregated simulation of Chapter 2. For all simulations, there will be 199 non-uniform vertical grids. The vertical resolution from the bottom to about the height of 15 km of the domain is approximately 100 m. For heights beyond 15 km, the vertical resolution is then stretched to 400 m at the top of the domain.

The seven simulations presented in this chapter are composed of four simulations with the stochastic backscatter TKE scheme, one SKEBS simulation, the standard simulation with no stochastic forcing and the higher resolution dx = 1 km simulation. Except for the dx = 1 km simulation, the other six simulations have horizontal resolution of 4 km. The dx = 1 km simulation is the high-resolution simulation from Chapter 2, which uses the default TKE subgrid turbulence scheme. The standard simulation is the non-aggregated simulation from Chapter 2, which uses the default TKE subgrid turbulence scheme. The SKEBS simulation is created by replacing the TKE subgrid turbulence scheme of the standard simulation with the SKEBS scheme in WRF (Berner et al., 2011; Berner, 2013). The default values for the parameters for SKEBS in WRF are used (Berner, 2013). The four stochastic backscatter TKE situations are created by replacing the TKE subgrid turbulence

scheme of the standard simulation with the newly-implemented stochastic backscatter TKE scheme described by (4.30). The four stochasic backscatter TKE simulations are labelled by the perturbation amplitude (standard deviation) and the relaxation timescale. The four stochastic backscatter TKE simulations are given the labels a1tau50, a1tau500, a1pt5tau50 and a2tau50. The label can be understood by an example. Let's take a1pt5tau50 as an example: a1pt50tau50 means that the value of the standard deviation is 1.5 ($a = 1.5$), and the value of the relaxation timescale is 50 seconds ($\tau = 50$). The values of a and τ are chosen based on Marstorp et al. (2007). Marstorp et al. (2007) suggested the value of $\tau = 0.2 \left(\frac{\Delta^2}{\langle \tau_{ij} \overline{S_{ij}} \rangle} \right)^{1/3}$ using dimensional analysis and $a = 2.3$. The value of $\langle \tau_{ij} \overline{S_{ij}} \rangle$ is estimated using the result from Chapter 3, which gives $\tau \approx 500$ s. As a result, based on Marstorp et al. (2007) and Chapter 3, different values of a and τ are tested to investigate the effect of stochasticity on subfilter energy transfer rate. The list of all simulations in this chapter is given in table 4.1.

Name	Resolution (Δx)	Scheme	Details
a1tau50	4 km	Stochastic Backscatter TKE	$a = 1$, $\tau = 50$ s
a1tau500	4 km	Stochastic Backscatter TKE	$a = 1$, $\tau = 500$ s
a1pt5tau50	4 km	Stochastic Backscatter TKE	$a = 1.5$, $\tau = 50$ s
a2tau50	4 km	Stochastic Backscatter TKE	$a = 2$, $\tau = 50$ s
SKEBS	4 km	SKEBS	Default Values
Standard	4 km	Standard TKE	Non-aggregated from Ch. 2
$dx = 1$ km	1 km	Standard TKE	1-km simulation from Ch. 3

Table 4.1: The list of all simulations for this chapter. The four stochastic backscatter simulations and the SKEBS are modified and initialized from the non-aggregated simulation from Chapter 2. The parameters for stochastic backscatter TKE scheme are referring to a and τ from 4.30. The SKEBS simulation uses the default parameter values from WRF. The standard simulation is the non-aggregated simulation from Chapter 2 continued over the same time period as the other simulations in this chapter. The $dx = 1$ km simulation is the simulation presented in Chapter 3 also continued over the same time period as the other simulations in this chapter.

4.2.6 Diagnostics

Similar to the subgrid energy transfer rate and subfilter energy transfer rate analysis from Chapter 2, the comparison between the stochastic backscatter TKE scheme, the SKEBS

scheme, the standard simulation and the $dx = 1$ km simulation will be performed by the following. The subgrid energy transfer rate of the stochastic backscatter TKE scheme and the standard simulation is given by

$$P_K(x_1, x_2, x_3, t) = \rho \sum_{i,j=1}^{3} \tau_{ij}^d(x_1, x_2, x_3, t) S_{ij}(x_1, x_2, x_3, t), \tag{4.31}$$

which is consistent with the definition of the subfilter energy transfer rate from (3.1). The modelled subgrid scale momentum flux τ_{ij}^d is defined by

$$\tau_{ij}^d = -2K_{h,v}S_{ij}, \tag{4.32}$$

where K_h and K_v are the horizontal eddy viscosity and the vertical eddy viscosity, respectively. In the standard simulation, the horizontal and vertical eddy viscosity is given by TKE subgrid turbulence mixing scheme (e.g. Wyngaard, 2010). In the stochastic backscatter TKE simulations, the horizontal eddy viscosity is given by (4.30). If at least one of i, j is 3, then K_v is used. Otherwise, K_h is used.

The SKEBS scheme does not model the subgrid scale energy by an eddy viscosity model. Instead, the SKEBS scheme uses a zonal wind forcing u' and a meridional wind forcing v' given in subsection 4.2.3. To compare the subgrid energy transfer rate of the SKEBS simulation to the other simulations fairly, the formula of the subgrid energy transfer rate of the SKEBS simulation has to be modified, and it is given by

$$P_K(x_1, x_2, x_3, t) = \rho(uu' + vv'). \tag{4.33}$$

Similarly, to perform a spectral energy budget, the definition of the dissipation term has to be modified for SKEBS, and it is given by

$$D(\boldsymbol{k}, z) = \overline{\rho}\left(\hat{u}^* \mathcal{F}\left(u'\right) + \hat{v}^* \mathcal{F}\left(v'\right)\right). \tag{4.34}$$

4.3 Result

4.3.1 Overview

In order to have an overview of the evolution of the simulations, we first consider the top of the atmosphere (TOA) outgoing longwave radiation (OLR). The domain-averaged OLR can help to quantify aggregation (e.g. Wing et al., 2018). To be consistent with Chapter

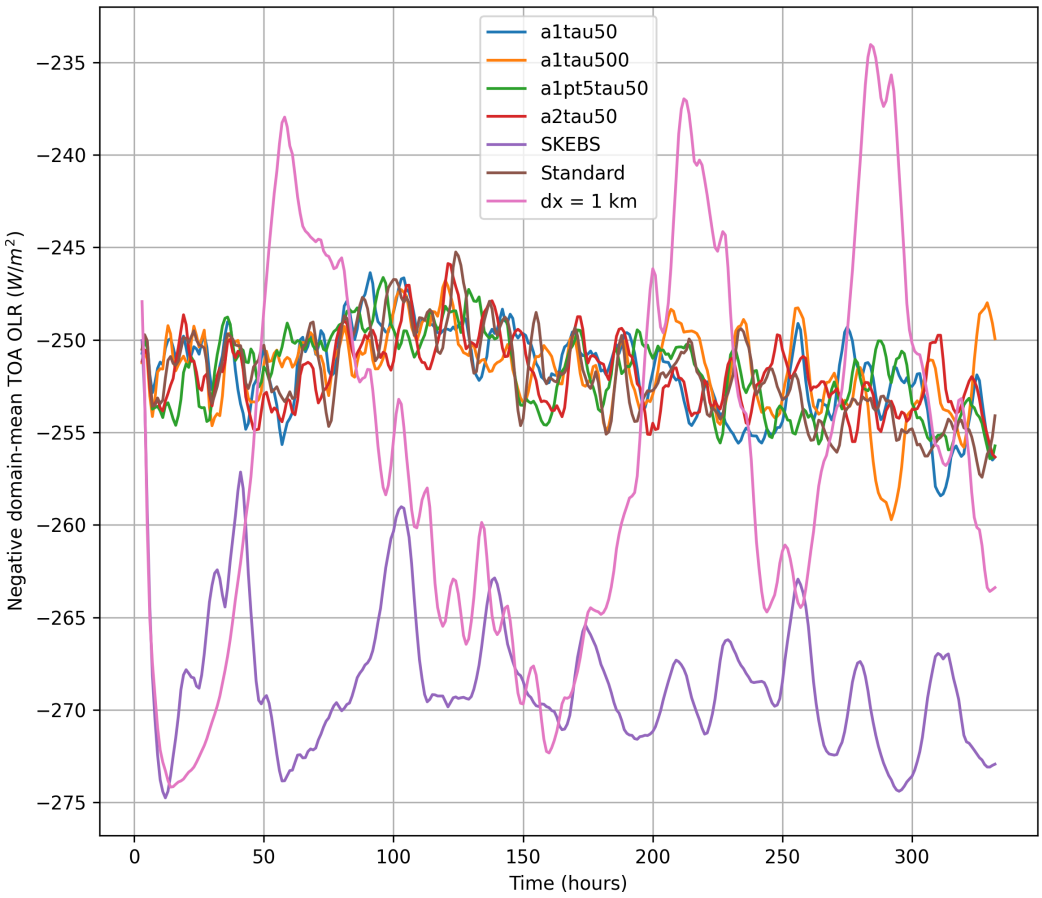


Figure 4.1: The time series of the negative of the domain-mean outgoing longwave radiation (W/m^2) at the top of the atmosphere (TOA OLR) for the a1tau50 (blue), a1tau500 (orange), a1pt5tau50 (green), a2tau50 (red), SKEBS (purple), standard (brown), $dx = 1$ km (pink) simulation. A 6-hour moving average is used to improve the readability.

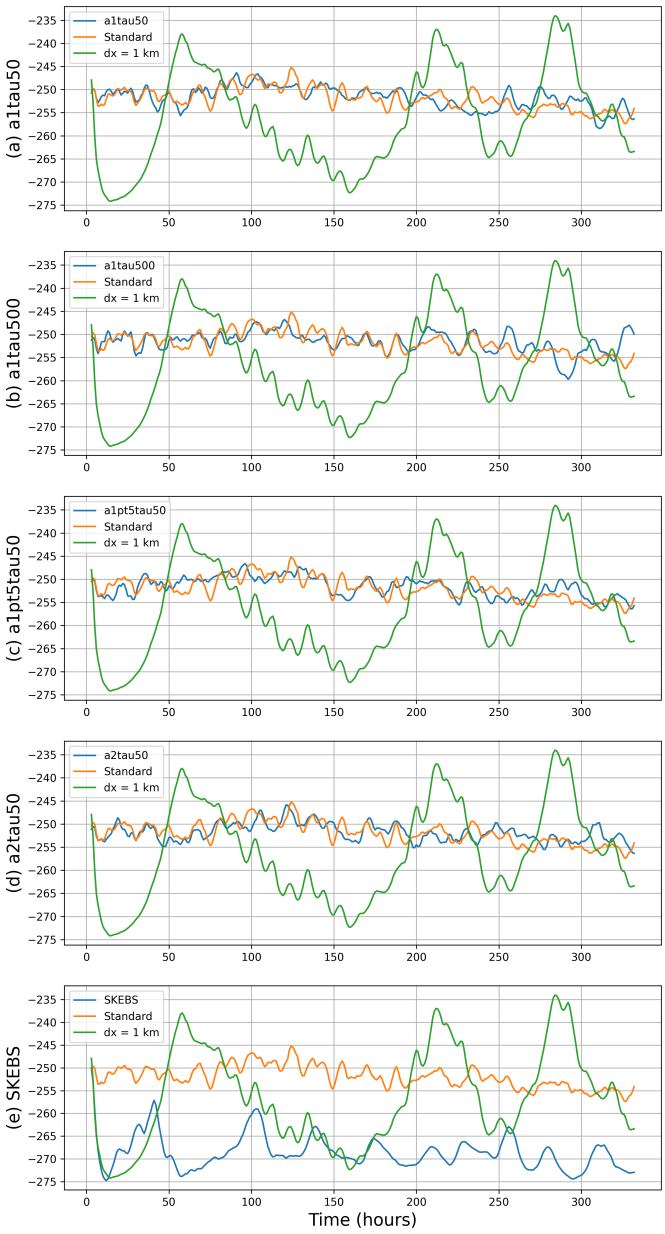


Figure 4.2: The time series of the negative of the domain-mean TOA OLR for the standard and the $dx = 1$ km simulations when compared with the (a) a1tau50, (b) a1tau500, (c) a1pt5tau50, (d) a2tau50, and (e) SKEBS simulations. A 6-hour moving average is used to improve the readability.

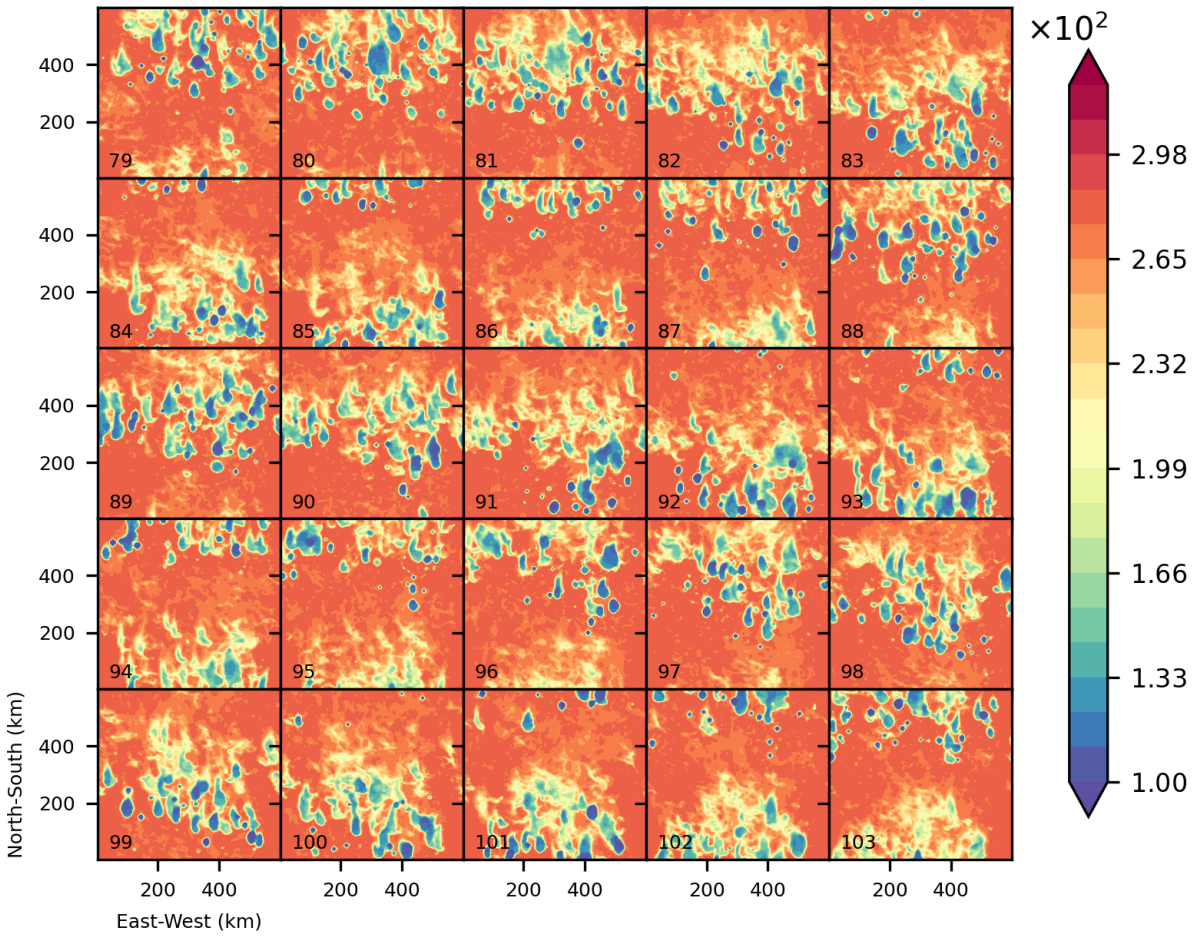


Figure 4.3: The TOA OLR ($\mathrm{W/m^2}$) 12 hours before and 12 hours after the most aggregated state for the a1tau50 simulation. The full 600 km (x) $\times$ 600 km (y) domain is shown.

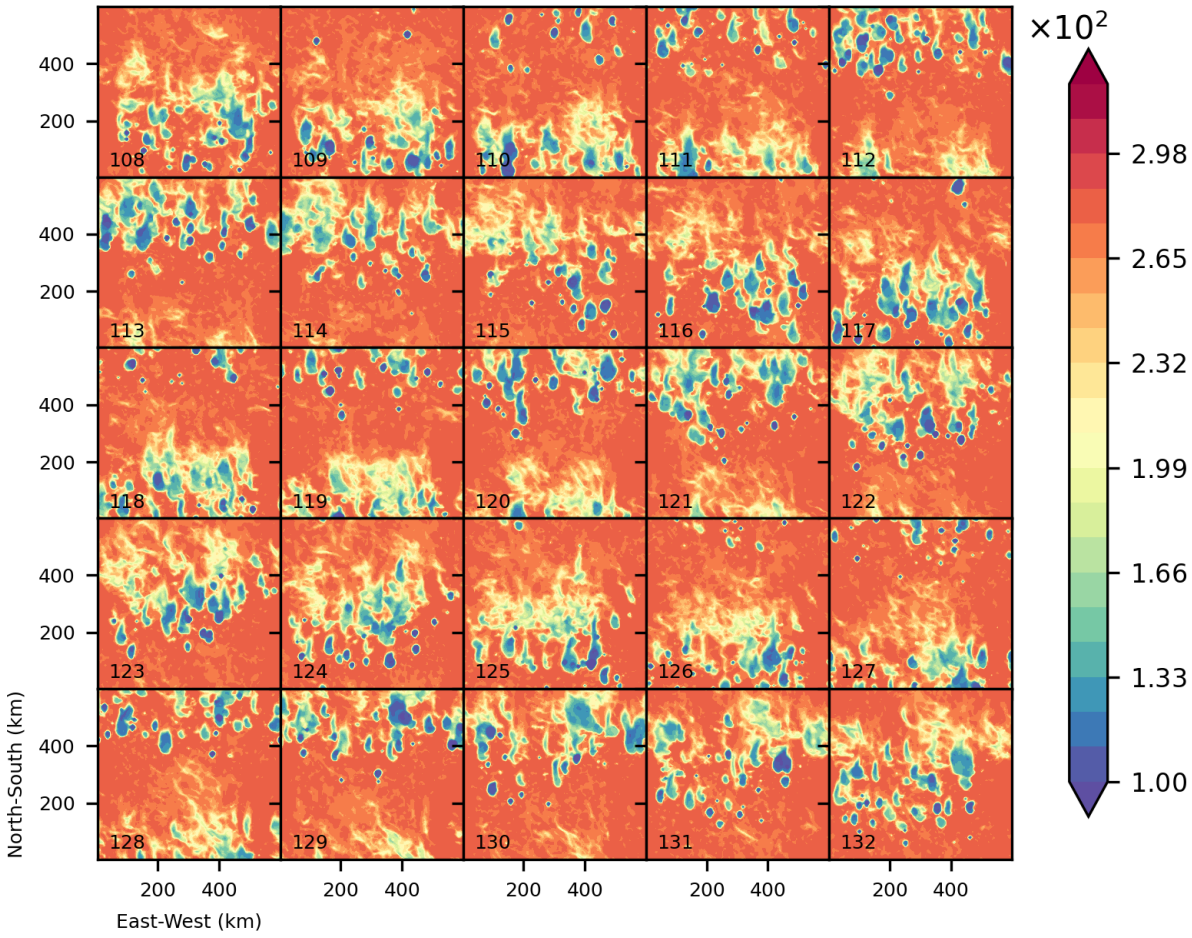


Figure 4.4: As in Fig. 4.3, but for the a1tau500 simulation.

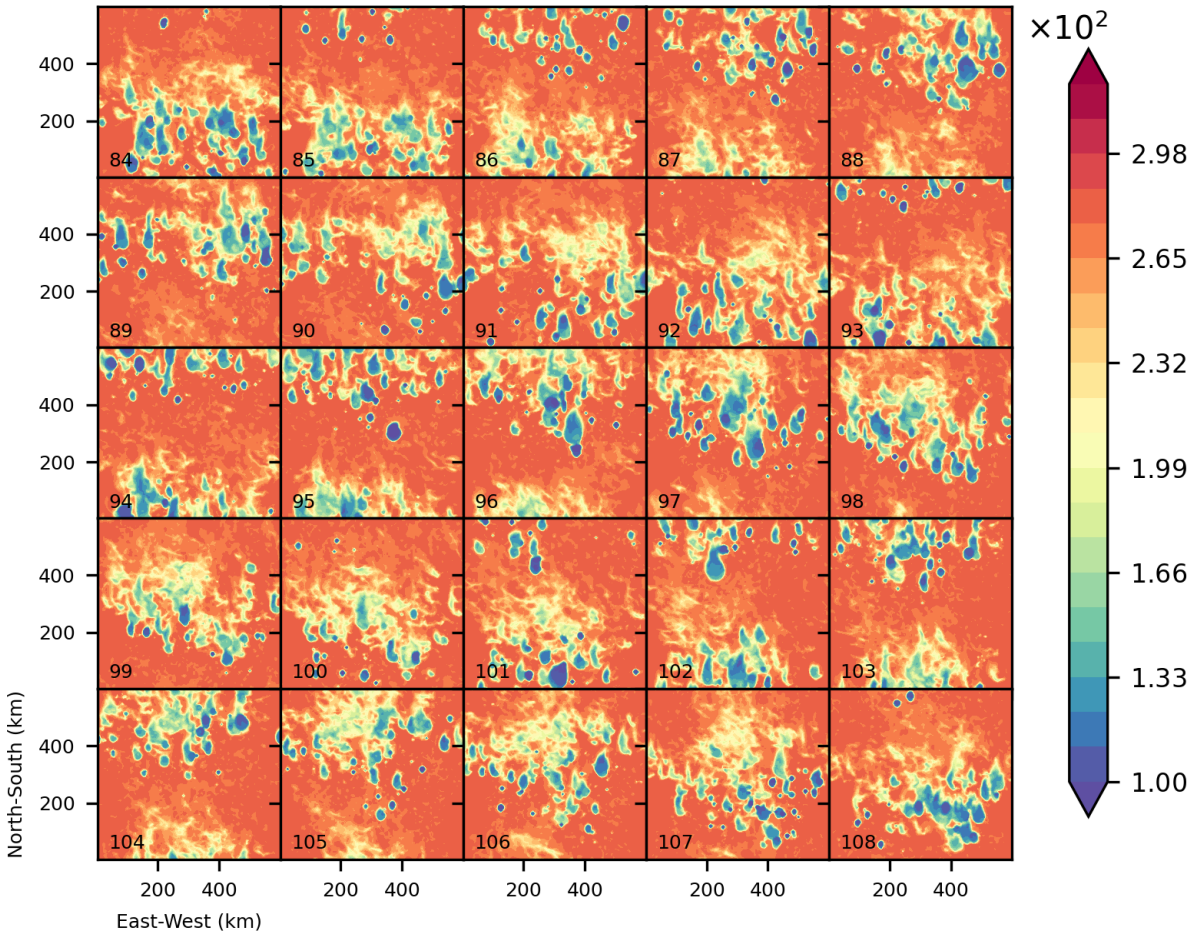


Figure 4.5: As in Fig. 4.3, but for the a1pt5tau50 simulation.

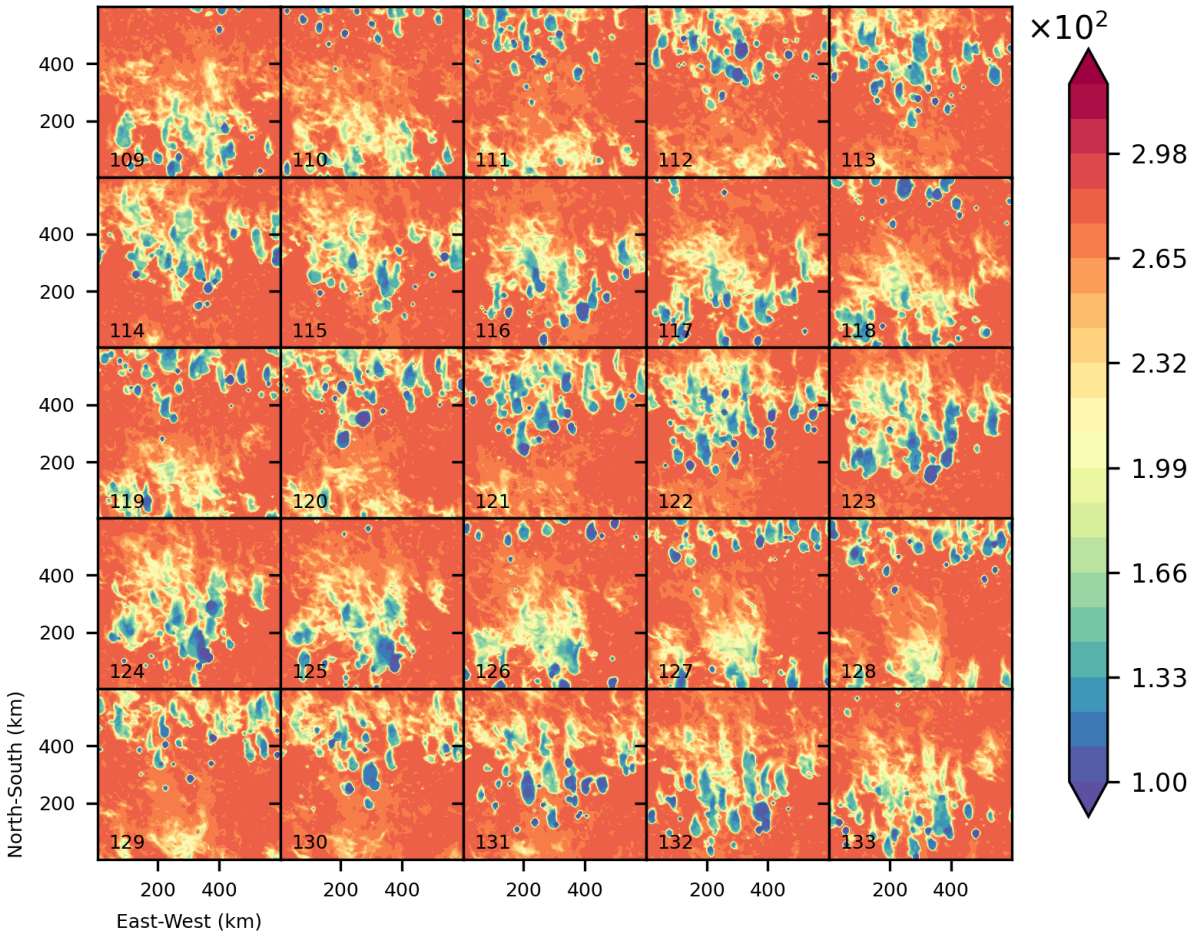


Figure 4.6: As in Fig. 4.3, but for the a2tau50 simulation.

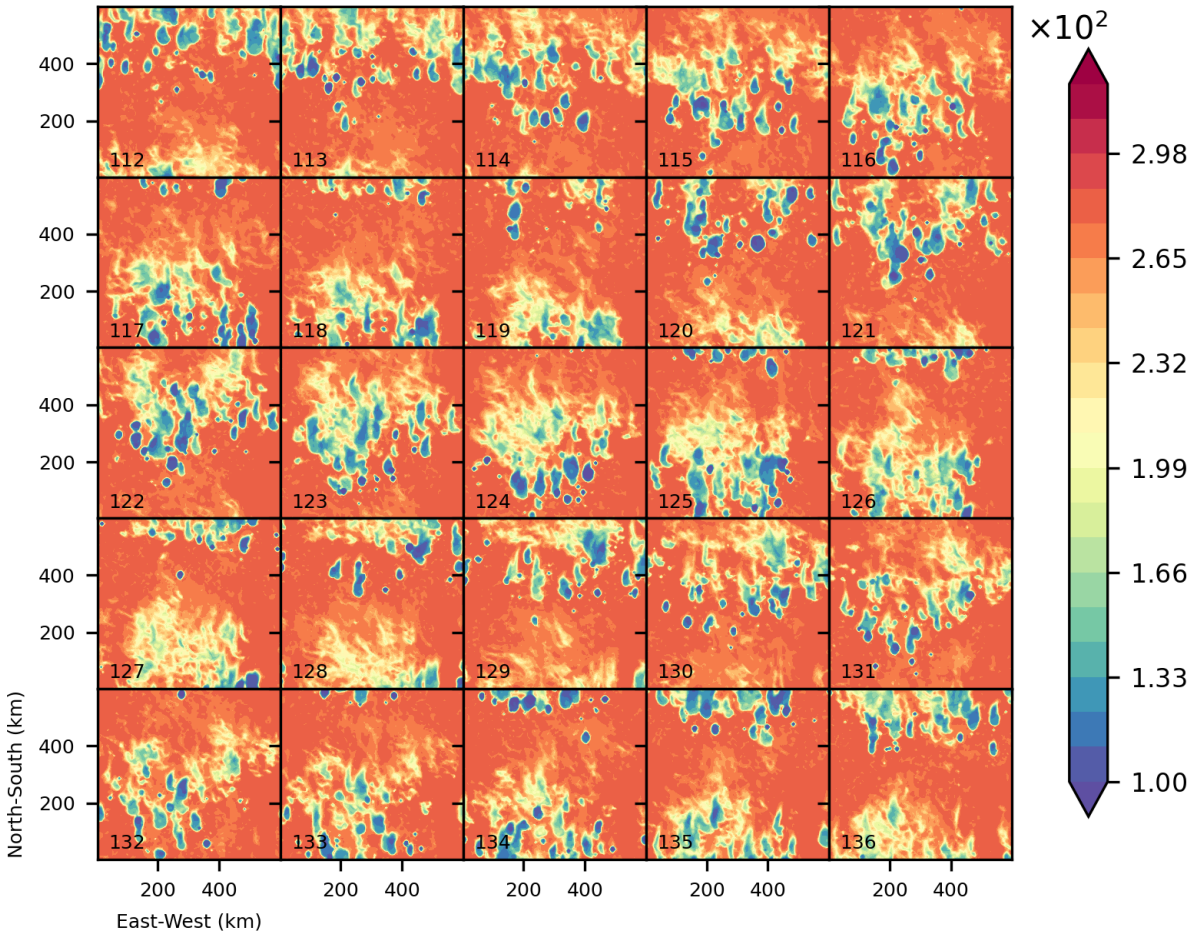


Figure 4.7: As in Fig. 4.3, but for the standard simulation.

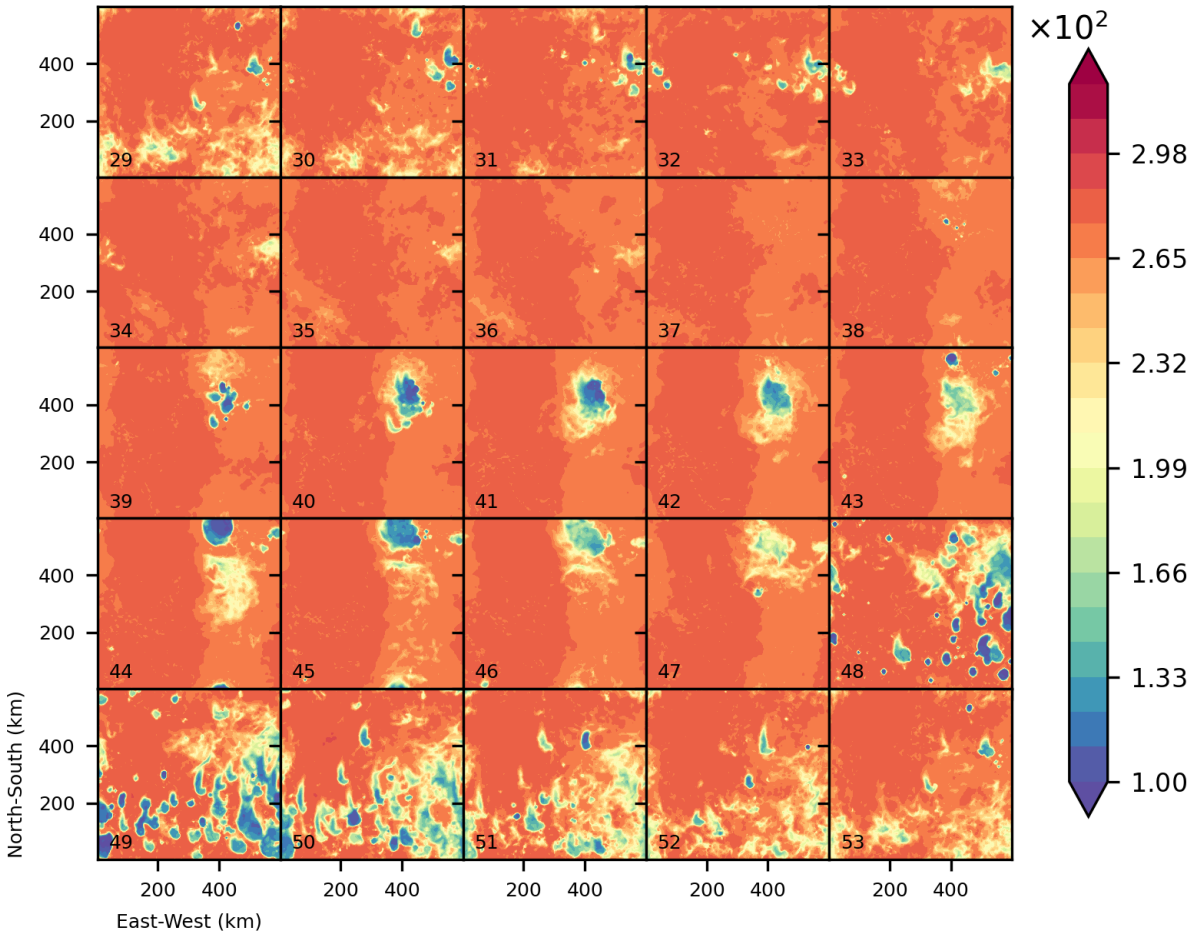


Figure 4.8: As in Fig. 4.3, but for the SKEBS simulation.

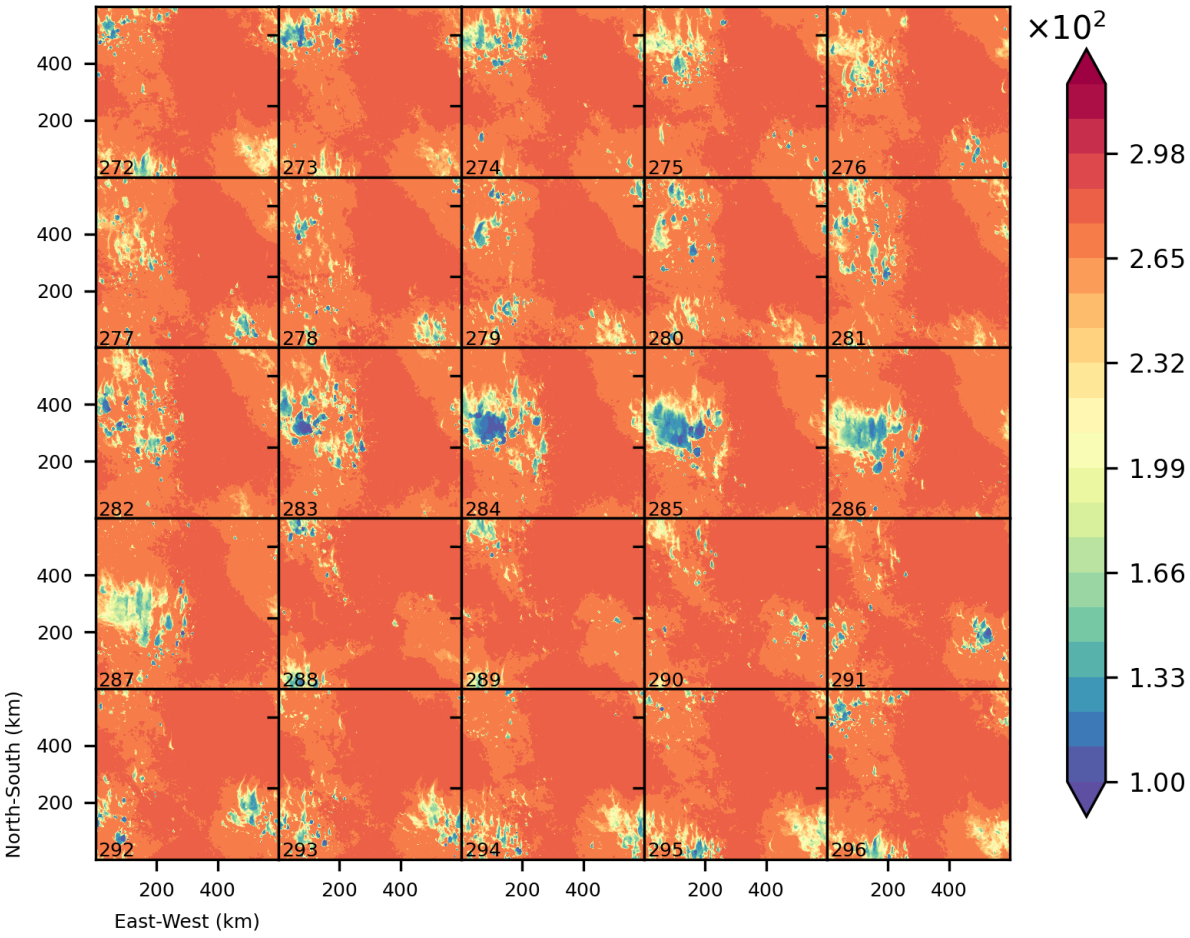


Figure 4.9: As in Fig. 4.3, but for the $dx = 1$ km simulation.

3, the negative of the domain-averaged TOA OLR is used. The negative of the domain-averaged TOA OLR will increase if there is more aggregation. This is because when there is more aggregation, the majority of the domain will have fewer clouds. We will first show the negative domain-averaged OLR for all seven simulations in Fig. 4.1. To compare the effect of stochastic backscatter schemes on TOA OLR to the regular TKE scheme, we will compare the negative of the domain-averaged TOA OLR of the five simulations with stochastic backscatter scheme individually (a1tau50, a1tau500, a1pt5tau50, a2tau50 and SKEBS) to the standard and $dx = 1$ km simulations in Fig. 4.2. The 25-hour TOA OLR contour of the most aggregated state for each simulation is also provided to help visualize the evolution of the RCE in each simulation (Fig. 4.3-4.9).

Adding a stochastic backscatter element to the TKE scheme does not significantly affect the evolution of average OLR (Fig. 4.1). The standard simulation does not have a strong peak in the time series of OLR, which means that the standard simulation does not create a convective system with aggregation. This is expected because the standard simulation is the non-aggregated simulation from Chapter 2. The time series of OLR of all four of the simulations with the stochastic backscatter TKE scheme (a1tau50,a1tau500,a1pt5tau50,a2tau50) are similar to the standard simulation (Fig. 4.1). Such a result also indicates that using the stochastic backscatter TKE scheme, at least with the values of the parameters used in this chapter, does not trigger aggregation in the non-aggregated simulation. Figure 4.2 compares the time series of OLR of the simulations with backscatter added in the subgrid turbulence scheme to the standard simulation and the $dx = 1$ km simulation. The standard simulation and the four simulations with the stochastic backscatter TKE scheme have a relatively flat OLR time series when compared to the $dx = 1$ km simulation and the SKEBS simulation (Fig. 4.2). In the $dx = 1$ km simulation, there are three strong, distinct peaks in the OLR time series, which are not captured in any of the lower-resolution simulations. The time series of the OLR for the simulation with SKEBS has weaker but more distinct peaks than the $dx = 1$ km simulation. Over a longer time, the simulation with a higher tau value seems to deviate more from the standard simulation at a later time. A stronger stochastic perturbation magnitude (the a value) deviates from the standard at some point, and the magnitude of deviation depends on the a value.

The 25-hour OLR contour of the most aggregated state for each simulation (Figs. 4.3-4.9) are discussed in this paragraph. The most aggregated state is when the 6-hour moving average of the negative of the domain-averaged OLR is at its highest value. The OLR contours of the 12 hours before and 12 hours after the most aggregated state for all simulations are provided to visualize the evolution of the RCE (Figs. 4.3-4.9). The standard simulation and the four simulations with the stochastic backscatter TKE scheme are non-aggregated

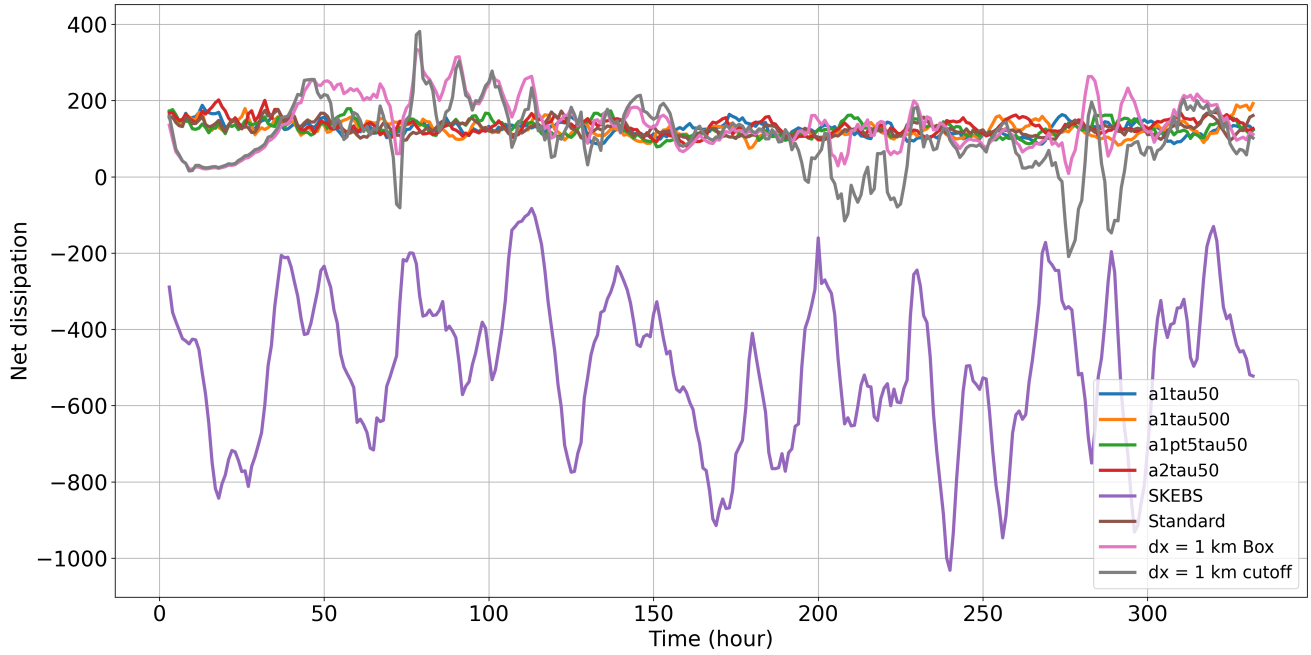


Figure 4.10: Time series of domain total net dissipation $-\iiint_V P_K dx_1 dx_2 dx_3/(5.0 \times 10^7 J/s)$ for the a1tau50 (blue), a1tau500 (orange), a1pt5tau50 (green), a2tau50 (red), SKEBS (purple), standard (brown) simulations and the subfilter energy transfer rate - $\iiint_V P dx_1 dx_2 dx_3/(5.0 \times 10^7 J/s)$ for $dx = 1$ km simulation with box-filter (pink) and cutoff filter. Positive values of net dissipation are dissipation, and negative values of net dissipation are backscatter.

simulations. Even at the most aggregated state, the convective plumes do not aggregate to form one or several large isolated convective systems. The OLR contours for SKEBS (Fig.4.8) and the high-resolution simulation (Fig.4.9) are similar. Unlike the stochastic backscatter TKE simulations, the SKEBS simulation (Fig. 4.8) developed one large isolated plume that lasted for a couple of hours before it disaggregated. Note that in an aggregated simulation (see the aggregated simulation from Chapter 2, Figure 2.1), the convective plume will stay aggregated after it becomes aggregated, and it will be hard for an aggregated convective plume to disaggregate.

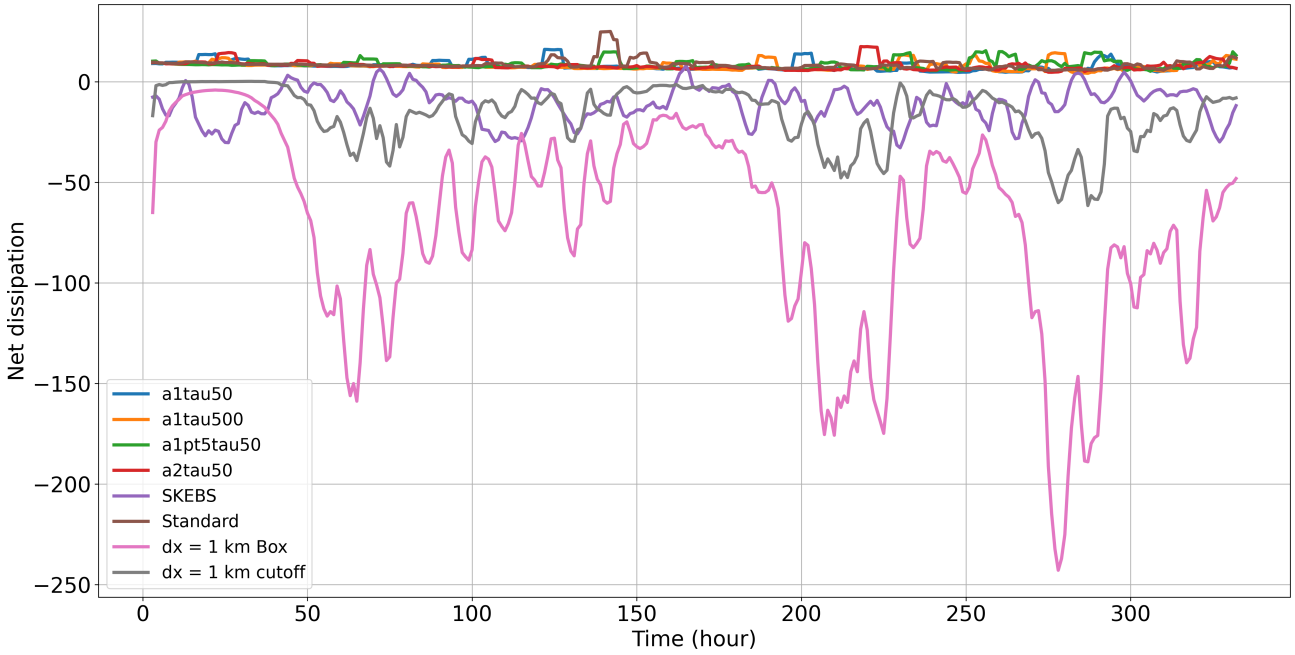


Figure 4.11: As in Fig. 4.10, but in the lower stratosphere.

4.3.2 Subgrid Energy Transfer and Subfilter Energy Transfer at 4 km Scale

As seen in the previous chapters, the dynamics of the upper troposphere and lower stratosphere are different. The remaining analysis will discuss the upper troposphere (6-10 km) and the lower stratosphere (15.5-17 km) unless otherwise stated. In order to understand the energy transfer at the horizontal resolution of 4 km, a subgrid energy transfer rate (cf. 4.31) analysis is performed. The subfilter energy transfer rate (cf. 3.2) obtained by filtering the 1-km high-resolution simulation in Chapter 3 will also be included for comparison in the discussion in this chapter.

In the upper troposphere, the time series of net dissipation (net subgrid energy transfer rate) of the standard simulation and the four simulations with the stochastic backscatter TKE scheme are similar, dissipative and relatively flat when compared to SKEBS and the subfilter energy transfer rate of the $dx = 1$ km simulation with the box filter and the cutoff filter (Fig. 4.10). The standard simulation and the four simulations with the stochastic backscatter TKE scheme are generally similar to the filtered high-resolution simulation, regardless of the filter. The net subgrid energy transfer rate of the standard

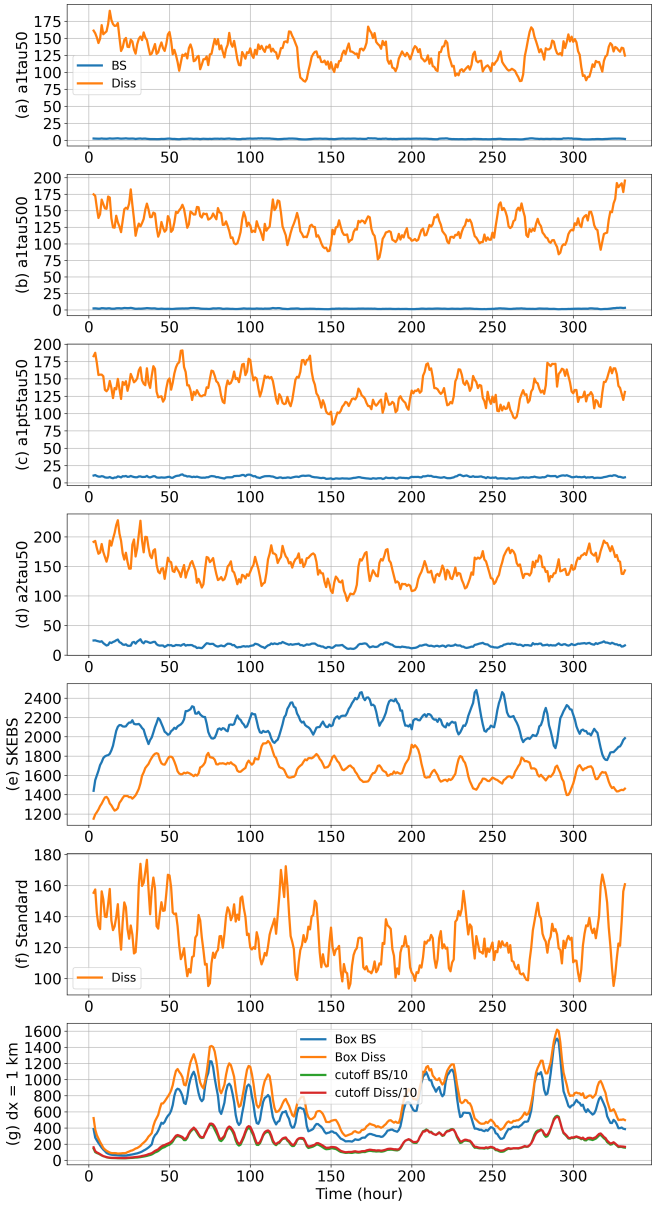


Figure 4.12: Time series of domain total dissipation (orange) and backscatter (blue) (5.0×10^7 J/s) for the (a) a1tau50, (b) a1tau500, (c) a1pt5tau50, (d) a2tau50, (e) SKEBS, (f) standard, and (g) $dx = 1$ km simulation with the box-filter and the cutoff filter in the upper troposphere. A 6-hour moving average is used to improve the readability. The net subgrid (subfilter) energy transfer rate ($\iiint_V P dx_1 dx_2 dx_3/(5.0 \times 10^7 J/s)$) are the sum of backscatter ($\iiint_V P_+ dx_1 dx_2 dx_3/(5.0 \times 10^7 J/s)$) and dissipation ($\iiint_V P_- dx_1 dx_2 dx_3/(5.0 \times 10^7 J/s)$), where $P = P_+ + P_-$ following (3.2.2) and (3.2.2).

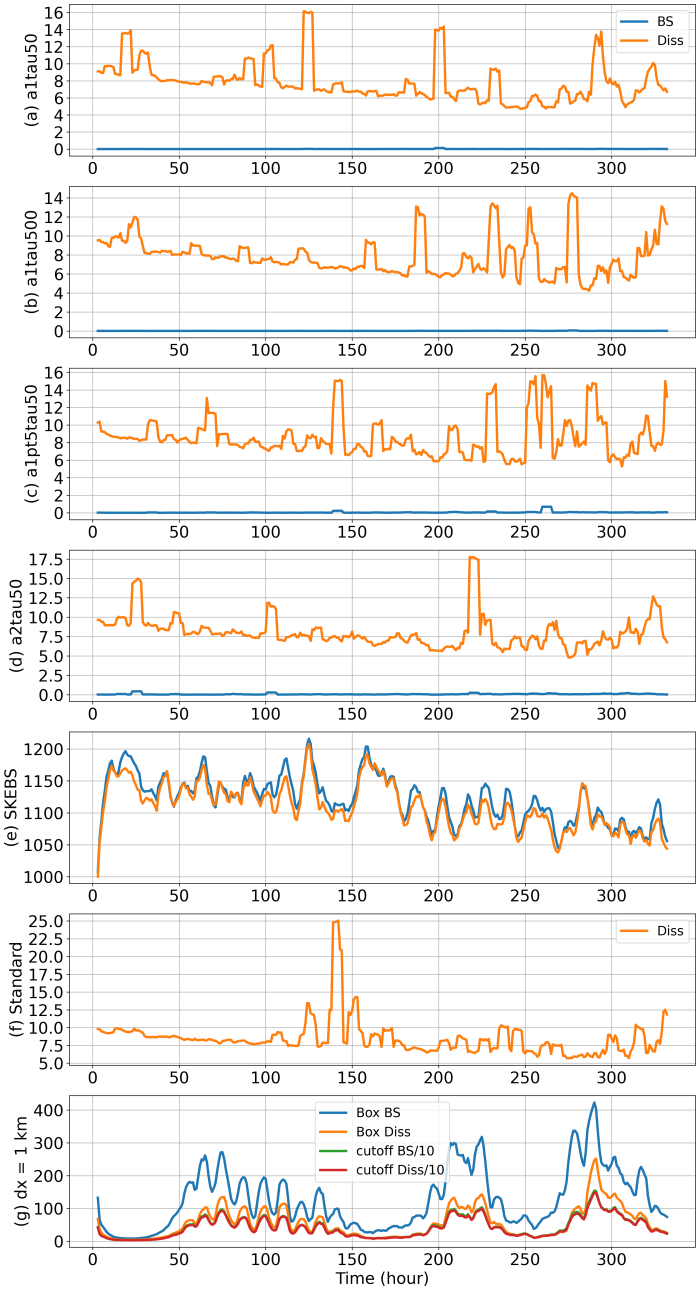


Figure 4.13: As in Fig. 4.12, but in the lower stratosphere.

simulation and the four stochastic backscatter TKE simulations are dissipative. It is known that the TKE subgrid turbulence mixing scheme used in the standard simulation is locally dissipative. The addition of a zero-mean perturbation in the eddy viscosity of the stochastic backscatter TKE scheme also results in a net dissipative subgrid energy transfer rate, but with potentially local backscatter. A net dissipative subgrid energy transfer rate has been reported in other backscatter-allowing subgrid turbulence schemes (e.g. Marstorp et al., 2007; Khani and Waite, 2015)). The subfilter energy transfer rate with the box filter of the high-resolution simulation is similar in magnitude to the standard and the four stochastic backscatter TKE simulation. The subfilter energy transfer rate of the high-resolution simulation with the cutoff filter is a lot stronger than the net dissipation from the standard simulation and the four stochastic backscatter TKE simulation. While the standard simulation, the four stochastic backscatter TKE simulation, and the subfilter energy transfer rate of the high-resolution simulation with the box filter are dissipative at all times, there is some backscattering in the subfilter energy transfer rate of the high-resolution simulation with the cutoff filter. Note that SKEBS is backscattering by design to compensate for the dissipation from effects such as the numerical dissipation (Berner et al., 2011). As a result, SKEBS is backscattering at all times (Fig. 4.10).

In the lower stratosphere, all simulations with the stochastic backscatter TKE scheme are dissipative at all times (Fig. 4.11). The magnitude of their dissipation is very similar to the standard simulation. However, the net dissipation of the SKEBS simulation and the subfilter energy transfer rate of the $dx = 1$ km simulation for both the box filter and the cutoff filter is negative (Fig. 4.11), which indicates backscattering. The backscatter in the lower stratosphere may be associated with wave-mean-flow interactions, according to the Eliassen-Palm flux analysis in Chapter 2.3.3. The backscatter in the lower stratosphere is captured by filtering the $dx = 1$ km simulation but not by the TKE parameterization, even with the stochastic effect included.

The net dissipation is obtained by subtracting the backscatter from the dissipation. To further investigate the net dissipation, the time series of the dissipation and the backscatter are presented separately for each simulation in figure 4.12. The stochastic backscatter TKE simulations have strong dissipation and relatively weak backscatter. In the stochastic backscatter TKE scheme, the backscatter occurs when the eddy viscosity is negative. The formulation of the eddy viscosity in the stochastic backscatter TKE scheme is $C_k(1 + aG)\Delta_h\sqrt{e}$, as described in (4.30). Note that the mean of G is zero, and the variance (determined by a) and the relaxation time scale τ are relatively weak. As a result, the term $1 + aG$ does not get large and negative often. Hence, the backscatter will not be very strong, and the net dissipation should be similar to the standard simulation. The backscatter and dissipation are both strong in the SKEBS simulation. The backscatter is

stronger than the dissipation in the SKEBS simulation, which is not the same as the net dissipative results from the simulations with the stochastic backscatter TKE scheme. The backscatter and dissipation are almost the same in both the subfilter energy transfer rate from the $dx = 1$ km simulation, with dissipation slightly stronger at most times.

In the lower stratosphere, the dissipation of all the stochastic backscatter TKE simulations is strong, and the backscatter is insignificant (Fig. 4.13a-d). This is similar to the upper troposphere; the magnitude of the dissipation in the lower stratosphere is significantly weaker than the upper troposphere. The magnitude of the dissipation of the standard simulation is slightly weaker than the dissipation from the simulations with the stochastic backscatter TKE scheme. The backscatter from the SKEBS simulation is marginally larger than the dissipation in the lower stratosphere (Fig. 4.13f). The $dx = 1$ km resolution also has a backscatter that is marginally larger than the dissipation in the lower stratosphere (Fig. 4.13g).

To conclude, although the stochastic backscatter TKE scheme is capable of producing backscatter, the amount of backscatter is insignificant when compared to the subfilter energy transfer rate from Chapter 3, in which a large amount of backscatter and dissipation exist. The stochastic backscatter TKE scheme also fails to produce a net backscattering in the lower stratosphere, which is likely generated by the wave-mean flow interaction according to Chapter 2. The amount of dissipation and backscatter are similar in other subfilter energy transfer rate analyses, such as transitional flows (e.g. Piomelli et al., 1991) and stratified turbulence (e.g. Khani and Waite, 2016; Khani and Porté-Agel, 2017). The net subgrid energy transfer rates from all the stochastic backscatter TKE simulations and the net subfilter energy transfer rate from the $dx = 1$ km simulation, regardless of filters, are dissipative, and they all have similar magnitude in the upper troposphere. While the magnitudes of the net subgrid energy transfer rate of the stochastic backscatter TKE simulations and the net subfilter energy transfer rate are similar, the ratio of the amount of dissipation and backscatter are different. In the stochastic backscatter TKE simulations, the amount of backscatter is negligible, and the dissipation dominates the net subgrid energy transfer rate by a large margin. In the $dx = 1$ km simulation, the net dissipation is given by a dissipation that is marginally larger than the backscatter in the upper troposphere. The SKEBS simulation is backscattering in the upper troposphere, which is different from the stochastic backscatter TKE simulations and the $dx = 1$ km simulation. In the lower stratosphere, the net subgrid energy transfer rate of the SKEBS simulation and the net subfilter energy transfer rate of the $dx = 1$ km simulation are both backscattering. In contrast to the SKEBS simulation and the $dx = 1$ km simulation, the net subgrid energy transfer rate of all the stochastic backscatter TKE simulations are dissipative in the lower stratosphere. A stronger perturbation on the stochastic forcing

may solve the problem of insufficient backscatter in the lower stratosphere when compared to the subfilter energy transfer rate of 1-km simulation.

4.3.3 Distribution of Local Energy Transfer

In the previous subsection, we have shown the time series of the dissipation and backscatter. Although the time series of the dissipation and backscatter provide some insight into the evolution of the dissipation and backscatter, they do not provide information on the distribution of the dissipation and backscatter. In this subsection, we will discuss the probability density function of the subgrid and subfilter energy transfer rate per volume at a horizontal resolution of 4 km for different schemes. Probability density function of the subfilter energy transfer rate per volume of the $dx = 1$ km simulation with both the box filter and the cutoff filter are provided for consistency with the previous subsections. Note that in the previous chapter, the discussion of the subfilter and subgrid energy transfer rates is expressed as units of energy per time, that is, J/s. In this subsection, in order to give a fair comparison to the histogram of the subfilter energy transfer rate from the a-priori study from the $dx = 1$ km simulation and the other simulations with 4-km resolution, the subfilter and subgrid energy transfer rates are compared in units of energy per time per volume, i.e. $\mathrm{J/s/m^3}$. Also instead of histogram, the probability density function is used in this chapter because the bin size of subgrid energy transfer rate from SKEBS is a lot smaller than the other simulations.

Except the probability density function for SKEBS, all the probability density functions presented in figure 4.14 have a very sharp peak at 0 and fall off rapidly to the strong positive and negative values of subfilter or subgrid energy transfer rate per volume in the upper troposphere. In the upper troposphere, the probability density functions for $dx = 1$ km with the box filter and the cutoff filter (Fig. 4.14) are similar and very symmetric, with a stronger weight on the dissipative side (negative values). Such shape from the probability density function for the subfilter energy transfer rate per volume for $dx = 1$ km with the box-filter and the cutoff filter can also be found in other a-priori analysis from DNS of homogeneous isotropic turbulence (e.g. Khani and Porté-Agel, 2017; Buzzicotti et al., 2018), homogeneous shear turbulence (e.g. Cardesa et al., 2015) and stratified turbulence (e.g. Khani and Porté-Agel, 2017)). In this chapter, the distribution of the subfilter energy transfer rate of the $dx = 1$ km simulation will be considered as a benchmark, and it will be used to compare the probability density function of the subgrid energy transfer rate per volume of the other simulations. A suitable subgrid scale model should be able to produce a subgrid energy transfer rate for low-resolution simulation that matches the subfilter energy transfer rate from DNS or high-resolution simulations.

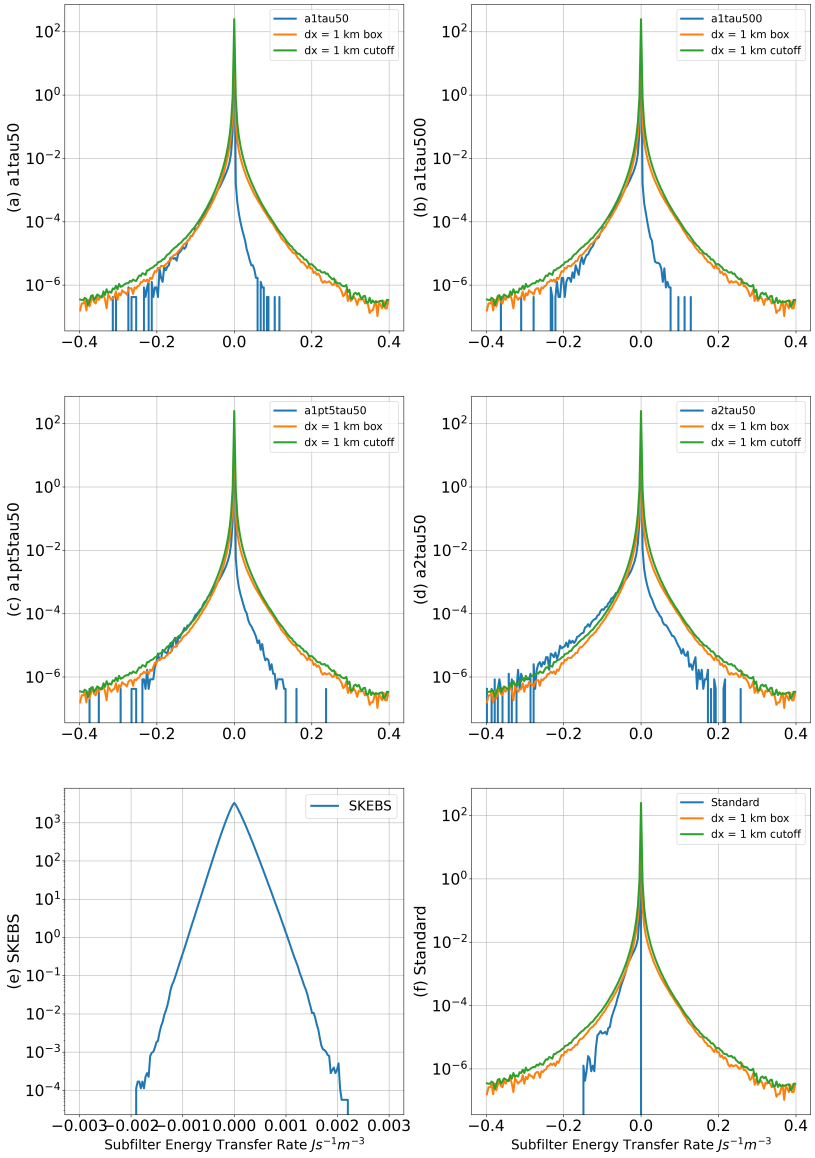


Figure 4.14: Probability density function (pdf) of the subfilter energy transfer rate per volume for $dx = 1$ km box (orange) and $dx = 1$ km cutoff (green) compared to the subgrid energy transfer rate per volume (blue) for (a) a1tau50, (b) a1tau500, (c) a1pt5tau50, (d) a2tau50, (e) SKEBS, and (f) standard simulation in the upper troposphere. The pdf are computed with 200 bins over -0.4 to 0.4 $\mathrm{Js^{-1}m^{-3}}$ except for the SKEBS simulation. The pdf for SKEBS is computed with 200 bins over -0.003 to 0.003 $\mathrm{Js^{-1}m^{-3}}$. Positive and negative values of subgrid (subfilter) transfer rate represent backscatter and dissipation, respectively.

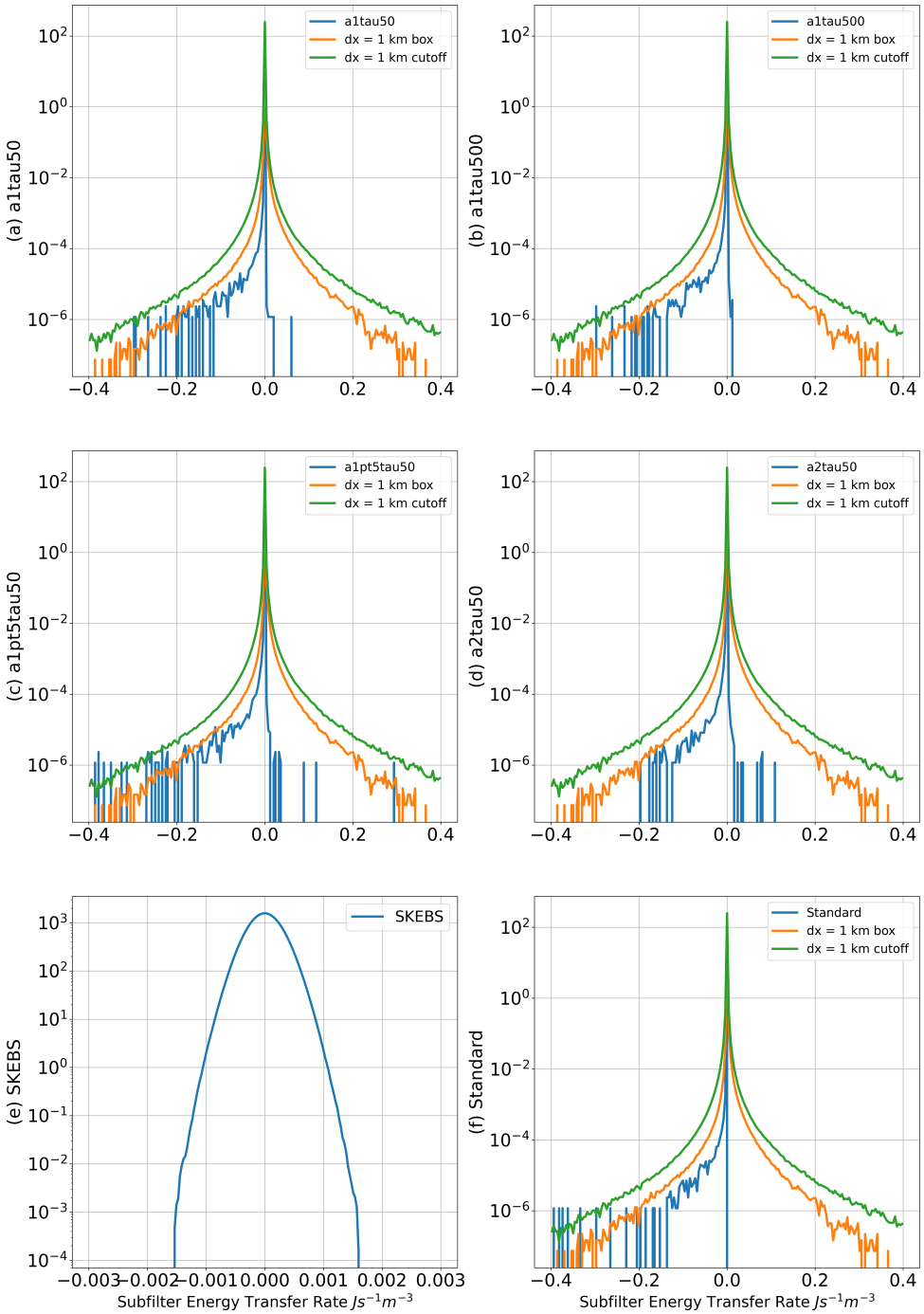


Figure 4.15: As in Fig. 4.14, but in the lower stratosphere

The four simulations with the stochastic backscatter TKE scheme can create a similar probability density function on the dissipation to the $dx = 1$ km subfilter energy transfer rate per volume (Fig. 4.14a-d) in the upper troposphere. Note that the dissipation from the standard simulation is not strong enough (Fig. 4.14f) when compared to the $dx = 1$ km subfilter energy transfer rate per volume in the upper troposphere. Hence, the addition of the stochastic backscatter component in the stochastic backscatter TKE scheme can improve the distribution of the dissipative values in a probability density function analysis. For the backscatter, one can see that the backscatter side of the probability density function is moving towards the right (large values of backscatter) and moving closer to the positive side of the probability density function $dx = 1$ km subfilter energy transfer rate per volume as we move from figure 4.14a to figure 4.14d. The a1tau50 (Fig. 4.14a) and the a1tau500 (Fig. 4.14b) simulations provide the least backscatter when one compares them to the other two stochastic backscatter TKE simulations. The a1pt5tau50 (Fig. 4.14c) have a probability density function with stronger values on the positive side when compared to the a1tau50 and a1tau500 simulations. The positive side of the probability density function of the a2tau50 simulation has the most strong values. The a2tau50 simulation is the closest to the $dx = 1$ km simulation when one compares the subfilter energy transfer rate per volume of the four stochastic backscatter TKE simulation to the $dx = 1$ km simulation.

To summarize, a stochastic backscatter TKE simulation with a stronger stochastic perturbation magnitude will provide a probability density function that is more similar to the probability density function of subfilter energy transfer rate per volume in the $dx = 1$ km simulation. Note that the ability to reproduce the distribution from $dx = 1$ km is not unique to the stochastic backscatter TKE simulations presented in this chapter. Some other backscatter-allowing subgrid turbulence schemes have also successfully reproduced the desired probability density function. For instance, the dynamic Smagorinsky scheme (e.g. Khani and Waite, 2015), the nonlinear gradient model (e.g. Khani and Porté-Agel, 2017), the modulated gradient models in stratified turbulence (e.g. Khani and Porté-Agel, 2017) and the stochastic backscatter Smagorinsky model from Marstorp et al. (2007) are examples of successfully reproducing the desired probability density function from a-priori analysis of DNS of turbulence, but not for RCE or convection permitting resolutions. While the probability density function for SKEBS also peaks at 0, the fall-off to the two sides is not as rapid as the other simulations. The probability density function of the subgrid energy transfer rate of SKEBS is fairly symmetric.

In the lower stratosphere, the probability density functions of the subfilter energy transfer rate per volume of the $dx = 1$ km simulation with both the box filter and the cutoff filter are fairly symmetric, with more weight on the positive side (backscattering). The probability density functions of the subgrid energy transfer rate per volume by all four

stochastic backscatter TKE simulations are more concentrated on the negative side (dissipative). The dissipation part of the probability density function of the subfilter energy transfer rate per volume of the $dx = 1$ km simulation is represented fairly well by all four of the stochastic backscatter TKE simulations (Fig. 4.15a-d) and even the standard simulation (Fig. 4.15f). However, all four of the stochastic backscatter TKE simulations and the standard simulation fail to reproduce the backscatter part of the subfilter energy transfer rate per volume of the $dx = 1$ km simulation by a large margin in the lower stratosphere. Such results explain the fact that all four stochastic backscatter TKE simulations fail to represent the backscattering result from the subfilter energy transfer rate of the $dx = 1$ km simulation (Fig. 4.11). In Chapter 3, we saw that the backscatter in the lower stratosphere is the result of the sum of a large amount of backscatter and dissipation. As a result, it is important that a subgrid model is capable of representing the backscatter portion of the probability density function of the subfilter energy transfer rate per volume of the $dx = 1$ km simulation. For SKEBS, the probability density function for the lower stratosphere is similar to the upper troposphere, and the probability density function for the lower stratosphere does not resemble the probability density function from other simulations.

4.3.4 Spectral Energy Budget

In the subsection, the horizontal kinetic energy spectra and the spectral energy budget in the upper troposphere and the lower stratosphere will be investigated. The kinetic energy spectra from the stochastic backscatter TKE simulations and the SKEBS simulation are compared with the observed -5/3 spectrum in the mesoscale. The spectral energy budget will provide insight into the effects of stochastic backscatter subgrid turbulence schemes on the kinetic energy spectrum.

In the upper troposphere, the horizontal kinetic energy spectra (Fig. 4.16a), the rotational kinetic energy spectra (Fig. 4.16b) and the divergent kinetic energy spectra (Fig. 4.16c) of all four of the stochastic backscatter TKE simulations are almost identical to those from the standard simulation. This can be explained by the fact that although backscatter is provided by the stochastic backscatter TKE scheme, the net dissipation is still unchanged, or the backscatter is not strong enough to affect the dynamics at larger scales. In the upper troposphere, the SKEBS scheme significantly energizes the horizontal kinetic energy spectrum at scales larger than $k = 20$ (size of 30 km), which resembles the -5/3 spectrum very well from large scales to scales before the small dissipative scales. The horizontal kinetic energy spectrum for the SKEBS simulation is also significantly more energetic than the standard and the stochastic backscatter TKE simulations at large scales. The injection of energy in the horizontal kinetic energy spectrum of the SKEBS simulation energizes both

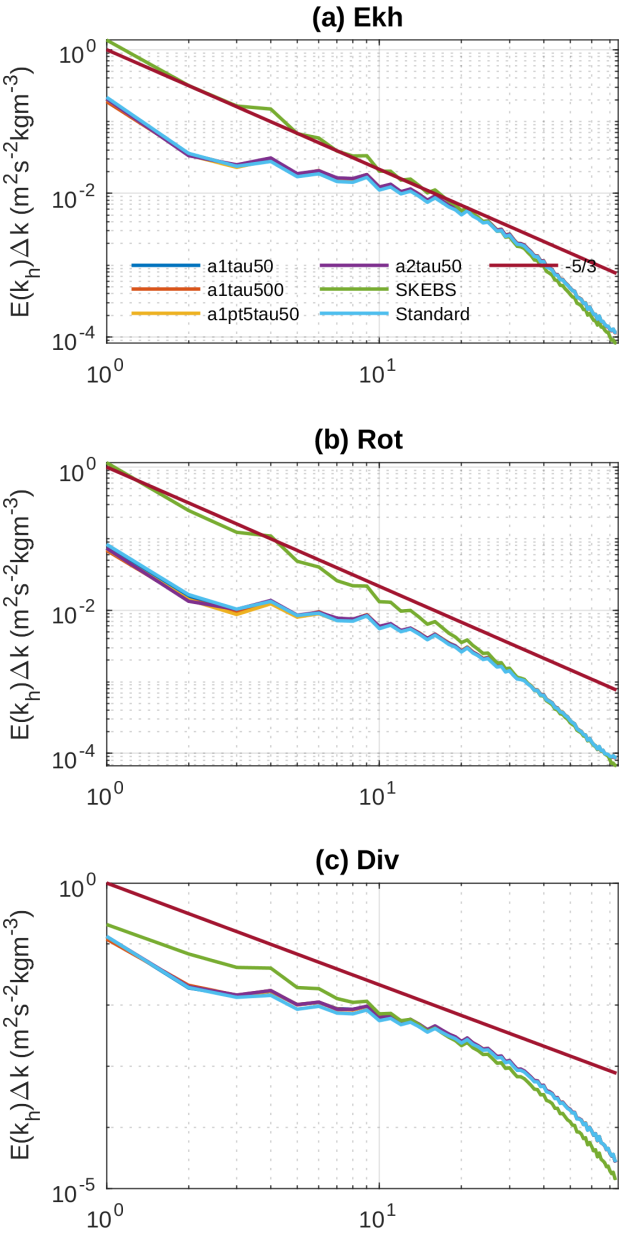


Figure 4.16: The horizontal kinetic energy spectrum can be decomposed into rotational kinetic energy spectra and divergent kinetic energy spectrum. This figure shows the (a) horizontal kinetic energy spectra, (b) rotational kinetic energy spectra and (c) divergent kinetic energy spectra for the a1tau50 (blue), a1tau500 (red), a1pt5tau50 (yellow), a2tau50 (purple), SKEBS (green) and standard (light blue) simulations in the upper troposphere. The -5/3 spectrum is given by the dark red line.

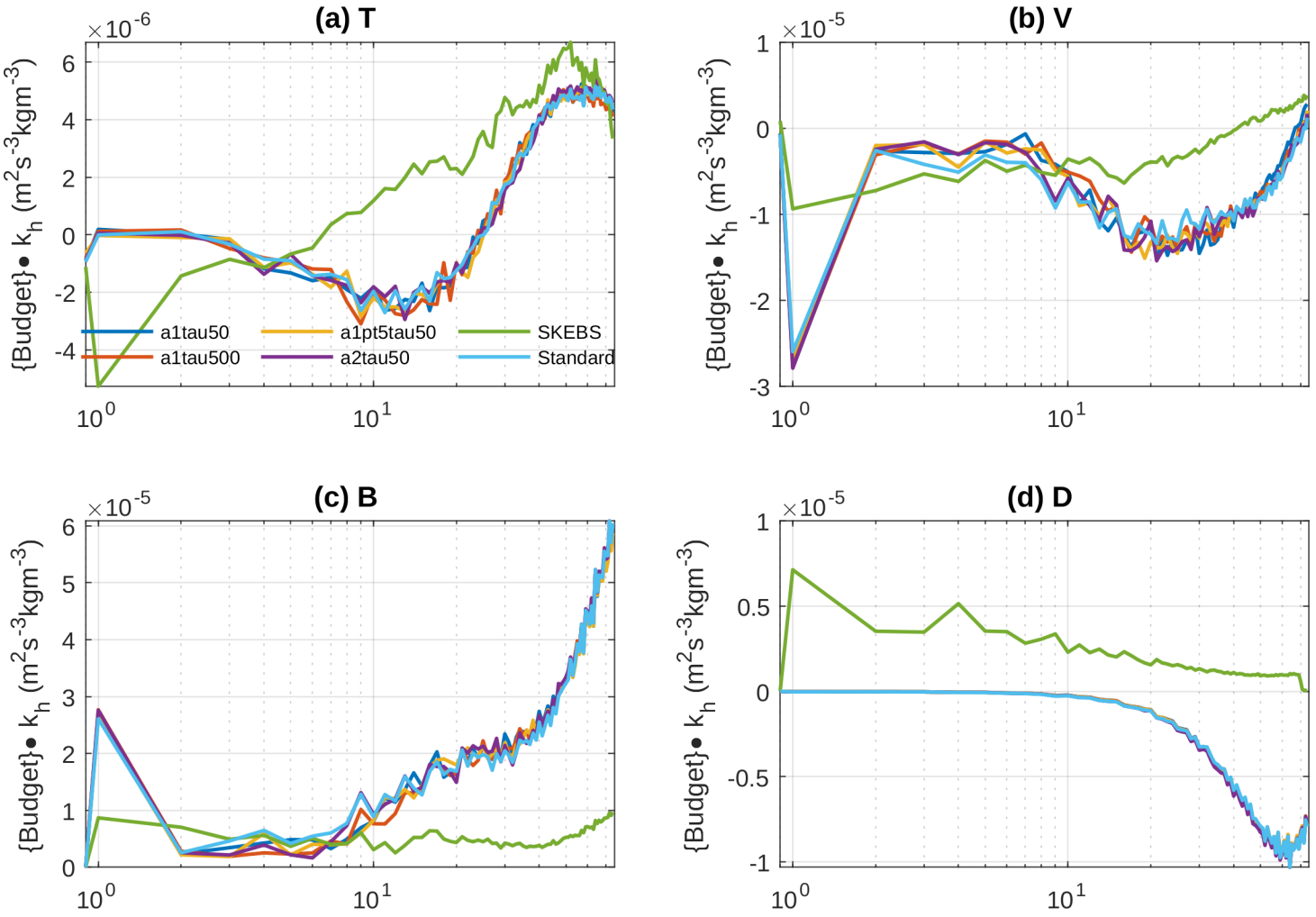


Figure 4.17: The spectral kinetic energy budget is composed of the horizontal nonlinear energy transfer, buoyancy flux, vertical energy flux divergence and dissipation. This figure shows the (a) horizontal nonlinear energy transfer, (b) vertical energy flux divergence, (c) buoyancy flux and (d) dissipation which stochastic subgrid forcings for the a1tau50 (blue), a1tau500 (red), a1pt5tau50 (yellow), a2tau50 (purple), SKEBS (green) and standard (light blue) simulations in the upper troposphere. All spectra are averaged in time over the full 14-day simulation and in the vertical.

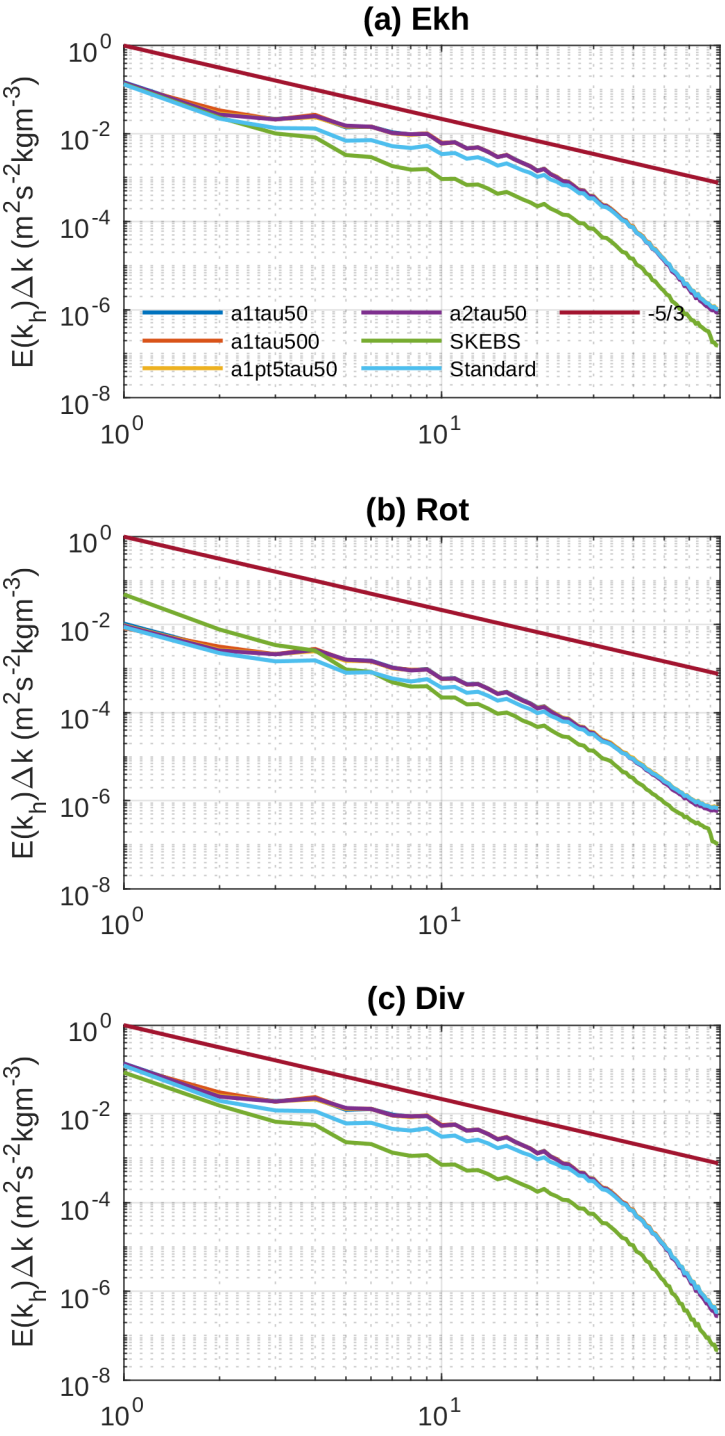


Figure 4.18: As in Fig. 4.16, but in the lower stratosphere.

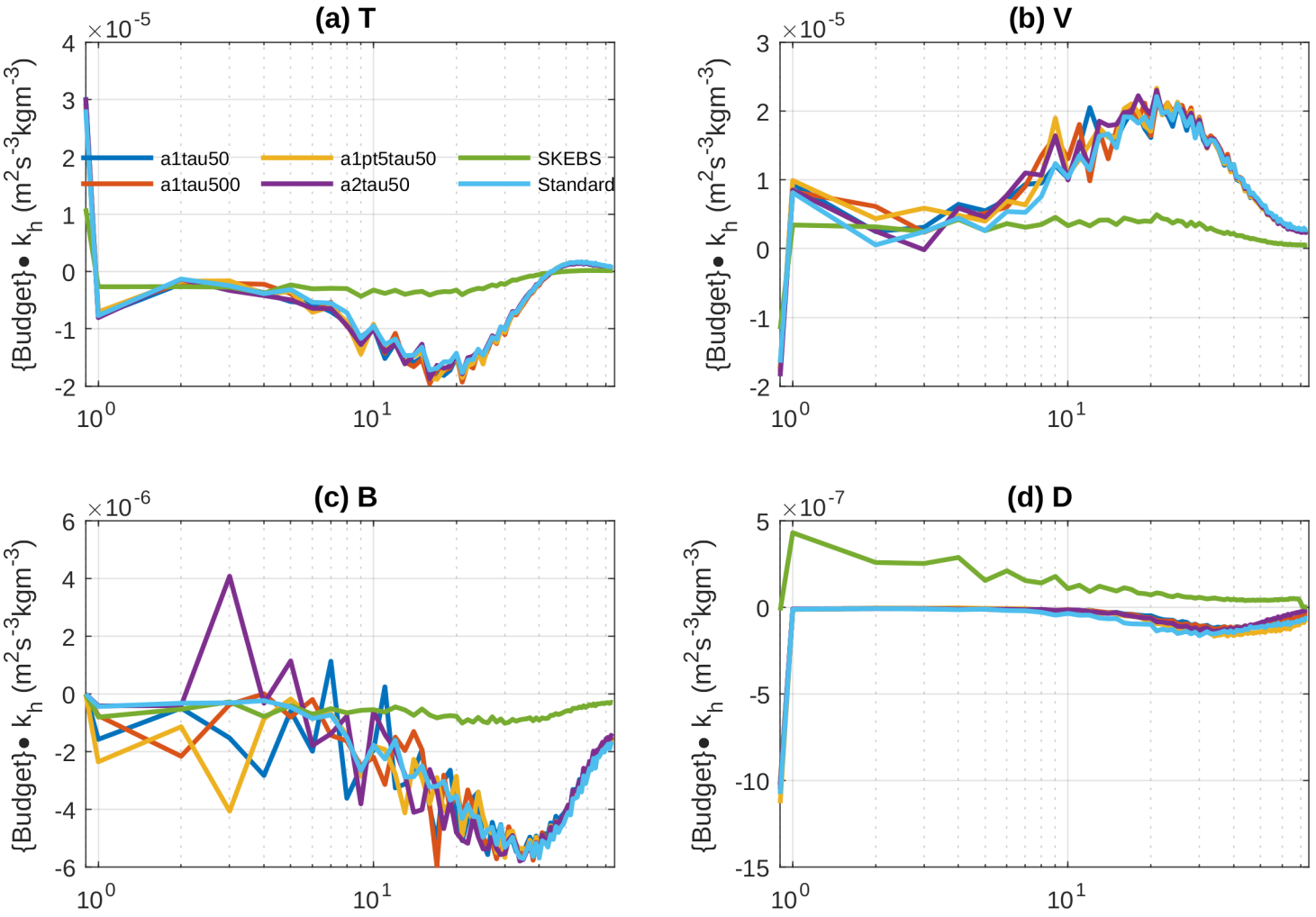


Figure 4.19: As in Fig. 4.17, but in the lower stratosphere.

the rotational (Fig. 4.16b) and divergent (Fig. 4.16c) components of the kinetic energy. The rotational kinetic energy is more energetic than the standard simulation at almost all scales except the dissipative scales, because the SKEBS scheme is designed to inject energy that has a $-5/3$ spectrum into the rotational components of the system. Given the fact that the SKEBS scheme is designed to inject energy into the rotational components, it is somewhat surprising to find that the divergent kinetic energy has also become more energetic with the use of the SKEBS scheme.

In the upper troposphere, since there are no significant differences in the horizontal kinetic energy spectra between the stochastic backscatter TKE simulations and the standard simulation, all the terms in the spectral energy budget, namely the transfer term, the vertical flux term, the buoyancy term and the dissipation term, for the stochastic backscatter TKE simulations are almost identical to the standard simulation (Fig. 4.17). In the upper troposphere, there is an energy gain in the buoyancy term at all scales (Fig. 4.17c). Some of that energy is transferred to the small dissipative scales by the transfer term (Fig. 4.17a), and the rest is transferred away from the upper troposphere by the vertical flux (Fig. 4.17b). The dissipation removes energy from the system at small scales (Fig. 4.17d). This has been reported in Chapter 2 and other studies such as Sun et al. (2017). While the spectral energy budget for the SKEBS simulation is different from the standard simulation, the basic mechanisms behind the spectral energy budget for the SKEBS simulation are similar to the standard simulation. Although there is an energy gain from the buoyancy term in the SKEBS simulation, similar to the standard simulation, the gain by buoyancy in the SKEBS simulation is significantly weaker (Fig. 4.17c) than the standard simulation. Instead of losing energy by dissipation like the standard simulation, there is a gain in energy from the backscatter for the SKEBS simulation (Fig. 4.17d). Similar to the standard simulation, energy is transferred away from the upper troposphere by the vertical flux term. There is an energy loss at the large scales by the transfer term, and that energy is transferred to the smaller scales in the SKEBS simulation, which is consistent with the forward energy transfer found in the standard simulation in Chapter 2.

In the lower stratosphere, the horizontal kinetic energy spectra for all four of the stochastic backscatter TKE simulations are almost identical, and they are sightly more energetic than the standard simulation from k = 2-20 (Fig. 4.18a). Such a result indicates that the stochastic backscatter TKE scheme produces spectra that are more energetic in the large scales in the lower stratosphere. The horizontal kinetic energy spectra of the stochastic backscatter TKE simulations are also closer to the -5/3 spectrum (Fig. 4.18a) from $k = 2$ (size of 300 km) to $k = 20$ (size of 30 km) when compared to the standard simulation. The rotational kinetic energy is significantly weaker than the divergent kinetic energy for all simulations (Fig. 4.18b). The difference in the horizontal kinetic energy

spectra between the stochastic backscatter TKE simulations and the standard simulation mainly comes from the divergent kinetic energy (Fig. 4.18c). The horizontal kinetic energy spectrum for the SKEBS simulation in the lower stratosphere is significantly weaker than the standard simulation. Similar to the findings for the upper troposphere, the horizontal kinetic energy spectrum in the lower stratosphere for the SKEBS simulation resembles the -5/3 spectrum at all scales except the dissipative scales. Both the rotational and divergent kinetic energy spectra resemble the -5/3 spectrum at all scales except the dissipative scales.

In the lower stratosphere, the spectral energy budget for the stochastic backscatter TKE simulations and the standard simulation are similar in all four components, namely the transfer term, the vertical flux term, the buoyancy term and the dissipation term. The nonlinear energy transfer spectra (Fig. 4.19a) and the dissipation spectra (Fig. 4.19d) are almost identical for all the stochastic backscatter simulations and the standard simulations. The stochastic backscatter TKE simulations have enhanced vertical energy flux divergence (Fig. 4.19b), which may explain why the horizontal kinetic energy spectra and divergent kinetic energy spectra of the stochastic backscatter TKE simulations are more energetic than the standard simulation. Note that the buoyancy term is approximately 10 times weaker, and the dissipation is approximately 100 times weaker than the transfer term and the vertical flux term. For the stochastic backscatter TKE simulations and the standard simulation, the energy is mainly supplied by the vertical flux from scales smaller than $k = 4$, likely from the upper troposphere. Then, that energy is directly injected upscale to the mean flow. There is some negligible energy loss at the small scales from the buoyancy term and the dissipation term for the stochastic backscatter TKE simulations and the standard simulation.

Note that while the backscatter provided by the stochastic backscatter TKE scheme is not significant in the lower stratosphere, the difference in energy spectra between the stochastic backscatter TKE simulations and the standard simulation can be due to the vertical energy flux from the upper troposphere. We can see that the gain of energy from the vertical flux of the stochastic backscatter simulations (Fig. 4.19b) is stronger than the standard simulation from $k = 4$ to $k = 20$, which coincide with the fact that the divergent kinetic energy of the stochastic backscatter TKE simulations are more energetic in the same range of wavenumbers (Fig. 4.18c).

All four components of the spectral energy budget are flat for the SKEBS simulation in the lower stratosphere, meaning the energy gain or loss is almost the same at most scales. Similar to the mechanism for the standard simulation in the lower stratosphere, the energy is mainly provided by the vertical flux for the SKEBS simulation in the lower stratosphere. Then, energy is directly injected upscale to the mean flow. There is an insignificant loss of energy from the buoyancy term and a weak gain in energy by the dissipation term

(backscatter).

4.4 Conclusions

The proposed stochastic backscatter TKE scheme is studied and compared to the SKEBS scheme in WRF in this chapter. The stochastic backscatter TKE scheme modifies the standard TKE scheme by adding a backscatter-allowing stochastic forcing to the eddy viscosity. The addition of a stochastic backscatter element to the standard TKE scheme, including both the stochastic backscatter TKE simulations and the SKEBS simulation, does not trigger aggregation. In this study, a stronger stochastic forcing in the stochastic backscatter TKE scheme, which can be increased by increasing the value of a or the relaxation timescale τ, does not result in significant deviation from the standard simulation. The net subgrid energy transfer rate in the stochastic backscatter TKE simulations is dominated by the dissipation by a large margin in both the upper troposphere and the lower stratosphere. The magnitude of the backscatter is negligible when compared to the dissipation in the stochastic backscatter TKE simulations. In contrast to the stochastic backscatter TKE simulations, the backscatter in the SKEBS simulation is stronger than the dissipation, and the magnitude of the dissipation and backscatter are comparable in the SKEBS simulation.

The probability density function of the subgrid energy transfer rate of the SKEBS simulation is fairly symmetric. It also has a round top centred at zero. The probability density function of the subgrid energy transfer rate in the stochastic backscatter TKE simulations and subfilter energy transfer rate from the $dx = 1$ km simulation are sharply peaked at zero. The stochastic backscatter TKE scheme has improved the standard TKE subgrid turbulence scheme in the dissipative portion of the probability density function of the subgrid energy transfer rate per volume in the upper troposphere.

The kinetic energy spectra at large scales in the lower stratosphere are energized by the stochastic backscatter TKE scheme compared to the standard case. The horizontal kinetic energy spectra of all four of the stochastic backscatter TKE simulations are more energetic at scales less than $k = 20$ in the lower stratosphere. The change in the kinetic energy spectra for the stochastic backscatter TKE simulations when compared to the standard simulation is likely due to an increase in energy gain in vertical energy flux at scales larger than $k = 20$ in the lower stratosphere. No significant changes were found in the kinetic energy spectra and the spectral energy budget in the upper troposphere when comparing the stochastic backscatter TKE simulations to the standard simulation. The horizontal kinetic energy spectra of the SKEBS simulations resemble the -5/3 spectrum in both the

upper troposphere and lower stratosphere, as expected. The SKEBS scheme is designed to inject the -5/3 spectrum into the atmosphere. The horizontal kinetic energy in the SKEBS simulation is significantly more energized than in the other simulations.

In the upper troposphere, the spectral energy budget suggests that energy is mainly injected to the large scales by subfilter parameterization in SKEBS, and the buoyancy and vertical energy flux are weaker when compared to other simulations. In the lower stratosphere, all the terms in the spectral budget are weak when compared to other simulations. This is likely due to the fact that the "dissipation" is not able to supply energy in the lower stratosphere, and the vertical energy flux in the upper troposphere is weak for the SKEBS simulation. As a result, energy cannot be transferred from the upper troposphere to the lower stratosphere.

However, the stochastic backscatter TKE scheme does not accurately represent the backscatter in the subgrid energy transfer rate analysis and the probability density function of the subgrid energy transfer rate per volume when compared to the subfilter energy transfer rate in the high-resolution $dx = 1$ km simulation. In Chapter 3, we saw that the net subfilter energy transfer rate is the result of summing a large amount of dissipation and backscatter. While the stochastic backscatter TKE scheme can represent the dissipation well and even improve on the dissipation portion of the standard TKE scheme, it does not produce enough backscatter when compared to the subfilter energy transfer rate from the $dx = 1$ km simulation. Hence, the stochastic backscatter TKE scheme fails to properly represent the backscatter portion. To improve the backscatter portion of the stochastic backscatter TKE scheme, one can increase the a value of the scheme. An increase in the a value will give a wider probability density function, and hence, the ratio of backscatter to dissipation will increase. However, the increase in a value also means that it will be more likely to have a negative eddy viscosity locally, which may make the simulation unstable. Note that a larger relaxation timescale will also create a scenario that there will be grid points with negative eddy viscosity, which again may lead to an unstable simulation. With the simulation configuration in this chapter, the simulation will quickly break down when stronger stochastic forcing (larger a or τ) is used. Even if clipping is used, the stochastic backscatter TKE simulation is still unstable with larger a or τ. Clipping is a method that sets the strong negative eddy viscosity to zero to enhance the stability of the simulation (e.g. Marstorp et al., 2007). Further investigation on the stability of the stochastic backscatter TKE scheme with a stronger stochastic perturbation should be done in order to improve the usability of the scheme.

5

Conclusion and Future Work

5.1 Concluding Remarks

In this thesis, the kinetic energy spectra, subfilter energy transfer and subgrid parameterization analysis of convective-permitting radiative-convective equilibrium simulations are performed, and a new stochastic backscatter-allowing subgrid scale model is proposed. In Chapter 2, the effects of aggregation in RCE on kinetic energy spectra and spectral energy budgets were studied. Aggregation has energized the horizontal kinetic energy spectra at large scales in both the upper troposphere and lower stratosphere. The horizontal kinetic energy spectra in the non-aggregated simulation in both the upper troposphere and lower stratosphere are shallower than the -5/3 spectrum. The horizontal kinetic energy spectra in the aggregated simulation in both the upper troposphere and lower stratosphere are steeper and closer to the -5/3 spectrum than the spectra in the non-aggregated simulation. Aggregation does not have a strong effect on the overall shape of all the terms in the spectral budget. In the upper troposphere, energy is injected by buoyancy flux and balanced by the removal of energy from the vertical energy flux. The nonlinear energy transfer term transfers energy from large to small scales. Energy in the small scales is then removed by dissipation, which is consistent with the direct energy cascade hypothesis. Although there is a direct energy cascade in the upper troposphere, the role of the nonlinear transfer term is insignificant compared to the buoyancy flux and vertical flux. These findings suggest that a -5/3 spectrum is not necessarily due to direct energy cascade but may be due to a balance in vertical energy flux and buoyancy flux. In the lower stratosphere, energy is injected by the vertical energy flux and balanced by the nonlinear energy transfer term. The nonlinear energy transfer term transfers energy from almost all scales to the mean

flow, which suggests that there is an inverse energy transfer in the lower stratosphere. An Eliassen-Palm analysis suggests that interaction of the small-scale waves with the mean flow may be one of the causes of the inverse energy transfer found in the lower stratosphere, rather than a traditional inverse cascade as found in two-dimensional turbulence.

In Chapter 3, a subfilter energy transfer rate analysis in an idealized RCE simulation is performed by filtering a 1-km high-resolution simulation to $\Delta x = 4$ km. Three filters, the box filter, the Gaussian filter and the spectral cutoff filter, are used in the subfilter energy transfer rate analysis. The dissipation and backscatter are stronger when the convective system is more aggregated and reduce when an aggregated convective system disaggregates. Regardless of the filter used, the subfilter energy transfer rate is dissipative in the upper troposphere and backscattering in the lower stratosphere. The net subfilter transfer rate is the result of summing a large amount of dissipation and backscatter. The normalized histogram suggests that there are more dissipative points than backscattering points in the upper troposphere, and the opposite is true for the lower stratosphere. The vertical and vertical shear components of the subfilter energy transfer rate are important in the upper troposphere, and only the vertical shear components of the subfilter energy transfer rate are important in the lower stratosphere. Such a result can be explained by the fact that RCE is mainly driven by convection, which is vertical in direction. In other words, the dynamics of the flow has an effect on the subfilter energy transfer rate. The use of cutoff filter results in significantly stronger dissipation and backscatter. The subfilter energy transfer rates computed with the box and Gaussian filters are almost identical to one another. The nonlinear spectral energy flux is consistent with the net subfilter energy transfer rate. In the upper troposphere, where the subfilter energy transfer rate is dissipative, there is a direct energy cascade. In the lower stratosphere, where the subfilter energy transfer rate is backscattering, there is an inverse energy cascade. The subfilter energy transfer rate analysis suggests that a purely dissipative subgrid turbulence scheme is not capable of representing the backscatter, which is found to be significant and comparable with the dissipation.

In Chapter 4, the stochastic backscatter TKE scheme, a stochastic backscatter-allowing subgrid turbulence scheme based on the TKE scheme, is proposed and compared to SKEBS, the default stochastic backscatter scheme included in WRF. The stochastic backscatter TKE scheme has improved the purely dissipative TKE scheme in the distribution of local energy transfer when compared to the subfilter energy transfer rate of the high-resolution 1-km simulation. The net dissipation of the stochastic backscatter TKE simulations is similar to the net dissipation of the regular TKE simulation. While backscatter is provided in the stochastic backscatter TKE scheme, it is insignificant when compared to the dissipation. While the number of points that are dissipative or backscattering is fairly even in SKEBS,

it does not resemble the normalized histogram of the subfilter energy transfer rate of the high-resolution 1-km simulation. SKEBS injects energy in the large scales in the upper troposphere. While the horizontal energy spectrum of the SKEBS simulation resembles the -5/3 spectrum, one may question if the spectrum in the SKEBS simulation is actually real or if that is an artificial spectrum forced by SKEBS.

5.2 Future Work

While this thesis presents some interesting results for kinetic energy spectra and subfilter energy transfer rate analysis and proposes a backscatter-allowing stochastic subgrid scales model, there are still some challenges that need to be addressed in order to improve in the future. First, a larger domain will be beneficial for this work. A larger domain makes the comparison to other studies such as Peng et al. (2015b) and Menchaca and Durran (2019) easier at scales of order of 1000 km. It may also help to identify whether the inverse energy transfer found in Chapter 2 will also exist at scales larger than 600 km. Because of restrictions in computational resources, it is not feasible to perform long RCE simulations with larger domains and higher resolutions. To give an idea of the constraint we faced computationally, if we have a larger domain or higher resolution, we can look at the simulation time and the post-processing time needed for the high-resolution 1-km simulation in Chapter 3 as an example. The 14-day 1-km simulation took 1024 cores of the Graham cluster from Compute Canada, a state-of-the-art supercomputer, about 384 hours to complete. The post-processing involved both interpolation and filtering. The interpolation took approximately 7040 core-hours to complete. The filtering took approximately 9856 core-hours to complete. As we can see, the simulation time and the post-processing time were tremendous. All the RCE simulations are run with the RRTMG radiation scheme, which is expensive to run. Emulation of radiative schemes with machine learning (e.g. Meyer et al., 2022; Ukkonen, 2022) may be a possible solution to overcome the high-performance computing resources constraint. In fact, machine learning may offer alternate approaches to improve weather forecast and climate modelling in area such as observational data reconstructions and subgrid scale parameterizations (e.g. Yuval and O'Gorman, 2020; Bracco et al., 2025).

Second, the effect of rotation and large-scale forcing on kinetic energy spectra should be studied. It is shown in Chapter 2 that rotation has an effect on aggregation and kinetic energy spectra. Without large-scale forcing in this study, the motion is primarily in the vertical direction, which explains the fact that the subfilter energy transfer rate is mainly dominated by the vertical and vertical shear components. In a subfilter energy transfer

rate analysis of a squall line (Lai and Waite, 2020), it was found that the backscatter and dissipation were dominated by the streamwise and shear components, which align with the direction of the wind shear in that study. As a result, the addition of large-scale forcing can help us explore the effect of large-scale forcing on the subfilter energy transfer rate.

Third, the connection between backscatter and inverse energy cascade is still unclear in our study. Physically, both the subfilter energy transfer rate and the nonlinear spectral energy transfer describe the energy transfer at a particular scale. The subfilter energy transfer rate describes the energy transfer between filtered and subfilter scales, and the nonlinear energy transfer describes the net energy transfer rate at a scale. In isotropic turbulence, the connection between the subfilter energy transfer rate and the nonlinear spectral energy flux can be found (cf. eq. 2 of Cardesa et al., 2015). However, it is not shown mathematically that such a relation should exist in areas other than isotropic turbulence. As a result, future work can explore the mathematical connection between the subfilter energy transfer rate and the nonlinear spectral energy flux.

Lastly, the stochastic forcing used in the stochastic backscatter TKE simulations may not be strong enough to produce the nearly 50-50 split in backscatter and dissipation found in other a-priori analysis (e.g. Piomelli et al., 1991). The results from Chapter 4 suggest that the ratio of backscatter to dissipation of the subgrid energy transfer rate from the stochastic backscatter TKE scheme is not large enough to recreate the histogram of the subfilter energy transfer rate of the high-resolution simulation. As a result, stronger a and τ values are needed. However, the simulations with stronger a and τ values led to instability in the simulations. More investigation on additional techniques such as clipping or even more creative solutions on improving the stability of the stochastic backscatter TKE simulations are needed.

References

Augier, P. and Lindborg, E. (2013). A new formulation of the spectral energy budget of the atmosphere, with application to two high-resolution general circulation models. *Journal of the Atmospheric Sciences*, 70(7):2293–2308.

Bartello, P. (1995). Geostrophic adjustment and inverse cascades in rotating stratified turbulence. *Journal of the atmospheric sciences*, 52(24).

Becker, T., Stevens, B., and Hohenegger, C. (2017). Imprint of the convective parameterization and sea-surface temperature on large-scale convective self-aggregation. *Journal of Advances in Modeling Earth Systems*, 9(2):1488–1505.

Berner, J. (2013). Wrf implementation details and version history of a stochastic kinetic-energy backscatter scheme (skebs). *National Center for Atmospheric Research Tech. Note, Boulder, CO*, 20.

Berner, J., Ha, S.-Y., Hacker, J., Fournier, A., and Snyder, C. (2011). Model uncertainty in a mesoscale ensemble prediction system: Stochastic versus multiphysics representations. *Monthly Weather Review*, 139(6):1972–1995.

Berner, J., Shutts, G., Leutbecher, M., and Palmer, T. (2009). A spectral stochastic kinetic energy backscatter scheme and its impact on flow-dependent predictability in the ecmwf ensemble prediction system. *Journal of the Atmospheric Sciences*, 66(3):603–626.

Bracco, A., Brajard, J., Dijkstra, H. A., Hassanzadeh, P., Lessig, C., and Monteleoni, C. (2025). Machine learning for the physics of climate. *Nature Reviews Physics*, 7(1):6–20.

Bretherton, C. S., Blossey, P. N., and Khairoutdinov, M. (2005). An energy-balance analysis of deep convective self-aggregation above uniform sst. *Journal of the Atmospheric Sciences*, 62(12):4273–4292.

Bryan, G. H. and Morrison, H. (2012). Sensitivity of a simulated squall line to horizontal resolution and parameterization of microphysics. *Monthly Weather Review*, 140(1):202–225.

Bryan, G. H., Wyngaard, J. C., and Fritsch, J. M. (2003). Resolution requirements for the simulation of deep moist convection. *Monthly Weather Review*, 131(10):2394–2416.

Buizza, R., Milleer, M., and Palmer, T. N. (1999). Stochastic representation of model uncertainties in the ecmwf ensemble prediction system. *Quarterly Journal of the Royal Meteorological Society*, 125(560):2887–2908.

Buzzicotti, M., Linkmann, M., Aluie, H., Biferale, L., Brasseur, J., and Meneveau, C. (2018). Effect of filter type on the statistics of energy transfer between resolved and sub-filter scales from a-priori analysis of direct numerical simulations of isotropic turbulence. *Journal of Turbulence*, 19(2):167–197.

Callies, J., Bühler, O., and Ferrari, R. (2016). The dynamics of mesoscale winds in the upper troposphere and lower stratosphere. *Journal of the Atmospheric Sciences*, 73(12):4853–4872.

Callies, J., Ferrari, R., and Bühler, O. (2014). Transition from geostrophic turbulence to inertia–gravity waves in the atmospheric energy spectrum. *Proceedings of the National Academy of Sciences*, 111(48):17033–17038.

Cardesa, J. I., Vela-Martín, A., Dong, S., and Jiménez, J. (2015). The temporal evolution of the energy flux across scales in homogeneous turbulence. *Physics of Fluids*, 27(11).

Charney, J. G. (1971). Geostrophic turbulence. *Journal of the Atmospheric Sciences*, 28(6):1087–1095.

Cho, J. Y. and Lindborg, E. (2001). Horizontal velocity structure functions in the upper troposphere and lower stratosphere: 1. Observations. *Journal of Geophysical Research: Atmospheres*, 106(D10):10223–10232.

Cho, J. Y., Zhu, Y., Newell, R. E., Anderson, B. E., Barrick, J. D., Gregory, G. L., Sachse, G. W., Carroll, M. A., and Albercook, G. M. (1999). Horizontal wavenumber spectra of winds, temperature, and trace gases during the pacific exploratory missions: 1. Climatology. *Journal of Geophysical Research: Atmospheres*, 104(D5):5697–5716.

Colin, M., Sherwood, S., Geoffroy, O., Bony, S., and Fuchs, D. (2019). Identifying the sources of convective memory in cloud-resolving simulations. *Journal of the Atmospheric Sciences*, 76(3):947–962.

Dewan, E. M. (1979). Stratospheric wave spectra resembling turbulence. *Science*, 204(4395):832–835.

Domaradzki, J. A., Liu, W., and Brachet, M. E. (1993). An analysis of subgrid-scale interactions in numerically simulated isotropic turbulence. *Physics of Fluids A: Fluid Dynamics*, 5(7):1747–1759.

Durran, D. R. (2010). *Numerical Methods for Fluid Dynamics: With Applications to Geophysics*, volume 32. Springer Science & Business Media.

Gage, K. (1979). Evidence far ak- 5/3 law inertial range in mesoscale two-dimensional turbulence. *Journal of the Atmospheric Sciences*, 36(10):1950–1954.

Grabowski, W. W. and Smolarkiewicz, P. K. (2002). A multiscale anelastic model for meteorological research. *Monthly Weather Review*, 130(4):939–956.

Hamilton, K., Takahashi, Y. O., and Ohfuchi, W. (2008). Mesoscale spectrum of atmospheric motions investigated in a very fine resolution global general circulation model. *Journal of Geophysical Research: Atmospheres*, 113(D18).

Higham, D. J. (2001). An algorithmic introduction to numerical simulation of stochastic differential equations. *SIAM review*, 43(3):525–546.

Holloway, C. E., Wing, A. A., Bony, S., Muller, C., Masunaga, H., L'Ecuyer, T. S., Turner, D. D., and Zuidema, P. (2017). Observing convective aggregation. *Surveys in Geophysics*, 38(6):1199–1236.

Holloway, C. E. and Woolnough, S. J. (2016). The sensitivity of convective aggregation to diabatic processes in idealized radiative-convective equilibrium simulations. *Journal of Advances in Modeling Earth Systems*, 8(1):166–195.

Holton, J. and Hakim, G. (2012). *An Introduction to Dynamic Meteorology*, volume 88. Academic Press.

Iacono, M. J., Delamere, J. S., Mlawer, E. J., Shephard, M. W., Clough, S. A., and Collins, W. D. (2008). Radiative forcing by long-lived greenhouse gases: Calculations with the aer radiative transfer models. *Journal of Geophysical Research: Atmospheres*, 113(D13).

Jeevanjee, N. and Romps, D. M. (2013). Convective self-aggregation, cold pools, and domain size. *Geophysical Research Letters*, 40(5):994–998.

Jiménez, P. A., Dudhia, J., González-Rouco, J. F., Navarro, J., Montávez, J. P., and García-Bustamante, E. (2012). A revised scheme for the WRF surface layer formulation. *Monthly Weather Review*, 140(3):898–918.

Khani, S. and Porté-Agel, F. (2017). Evaluation of non-eddy viscosity subgrid-scale models in stratified turbulence using direct numerical simulations. *European Journal of Mechanics-B/Fluids*, 65:168–178.

Khani, S. and Waite, M. L. (2015). Large eddy simulations of stratified turbulence: the dynamic smagorinsky model. *Journal of Fluid Mechanics*, 773:327–344.

Khani, S. and Waite, M. L. (2016). Backscatter in stratified turbulence. *European Journal of Mechanics-B/Fluids*, 60:1–12.

Kirkil, G., Mirocha, J., Bou-Zeid, E., Chow, F. K., and Kosović, B. (2012). Implementation and evaluation of dynamic subfilter-scale stress models for large-eddy simulation using WRF. *Monthly Weather Review*, 140(1):266–284.

Kolmogorov, A. N. (1941). The local structure of turbulence in incompressible viscous fluid for very large Reynolds numbers. *Cr Acad. Sci. URSS*, 30:301–305.

Kundu, P. K. and Cohen, I. M. (2001). *Fluid Mechanics*. Academic Press, second edition.

Lai, K. T. and Waite, M. L. (2020). Resolution dependence and subfilter-scale motions in idealized squall-line simulations. *Monthly Weather Review*, 148(7):3059–3078.

Lai, K. T. and Waite, M. L. (2023). Kinetic energy spectra and spectral budget of radiative–convective equilibrium. *Journal of the Atmospheric Sciences*, 80(8):1953–1970.

Leith, C. (1990). Stochastic backscatter in a subgrid-scale model: Plane shear mixing layer. *Physics of Fluids A: Fluid Dynamics*, 2(3):297–299.

Lemons, D. S. (2002). An introduction to stochastic processes in physics.

Lesieur, M. and Metais, O. (1996). New trends in large-eddy simulations of turbulence. *Annual review of fluid mechanics*, 28(1):45–82.

Li, Q. and Lindborg, E. (2018). Weakly or strongly nonlinear mesoscale dynamics close to the tropopause? *Journal of the Atmospheric Sciences*, 75(4):1215–1229.

Lilly, D. K. (1967). K. The representation of small-scale turbulence in numerical simulation experiments. *Proc. IBM Sci. Comput. Symp. on Environm. Sci*, pages 195–210.

Lilly, D. K. (1983). Stratified turbulence and the mesoscale variability of the atmosphere. *Journal of the Atmospheric Sciences*, 40(3):749–761.

Lindborg, E. (2006). The energy cascade in a strongly stratified fluid. *Journal of Fluid Mechanics*, 550:207–242.

Malardel, S. and Wedi, N. P. (2016). How does subgrid-scale parametrization influence nonlinear spectral energy fluxes in global NWP models? *Journal of Geophysical Research: Atmospheres*, 121(10):5395–5410.

Marstorp, L., Brethouwer, G., and Johansson, A. V. (2007). A stochastic subgrid model with application to turbulent flow and scalar mixing. *Physics of fluids*, 19(3).

Mason, P. J. and Thomson, D. J. (1992). Stochastic backscatter in large-eddy simulations of boundary layers. *Journal of Fluid Mechanics*, 242:51–78.

Menchaca, M. Q. and Durran, D. R. (2019). The influence of gravity waves on the slope of the kinetic energy spectrum in simulations of idealized midlatitude cyclones. *Journal of the Atmospheric Sciences*, 76(7):2103–2122.

Meneveau, C. and Katz, J. (2000). Scale-invariance and turbulence models for large-eddy simulation. *Annual Review of Fluid Mechanics*, 32(1):1–32.

Meyer, D., Hogan, R. J., Dueben, P. D., and Mason, S. L. (2022). Machine learning emulation of 3d cloud radiative effects. *Journal of Advances in Modeling Earth Systems*, 14(3):e2021MS002550.

Moeng, C.-H., Sullivan, P., Khairoutdinov, M., and Randall, D. (2010). A mixed scheme for subgrid-scale fluxes in cloud-resolving models. *Journal of the Atmospheric Sciences*, 67(11):3692–3705.

Moser, R. D., Haering, S. W., and Yalla, G. R. (2021). Statistical properties of subgrid-scale turbulence models. *Annual Review of Fluid Mechanics*, 53:255–286.

Muller, C. and Bony, S. (2015). What favors convective aggregation and why? *Geophysical Research Letters*, 42(13):5626–5634.

Muller, C. J. and Held, I. M. (2012). Detailed investigation of the self-aggregation of convection in cloud-resolving simulations. *Journal of the Atmospheric Sciences*, 69(8):2551–2565.

Nastrom, G. and Gage, K. S. (1985). A climatology of atmospheric wavenumber spectra of wind and temperature observed by commercial aircraft. *Journal of the Atmospheric Sciences*, 42(9):950–960.

Neelin, J. D. and Held, I. M. (1987). Modeling tropical convergence based on the moist static energy budget. *Monthly Weather Review*, 115(1):3–12.

Nolan, D. S., Rappin, E. D., and Emanuel, K. A. (2007). Tropical cyclogenesis sensitivity to environmental parameters in radiative–convective equilibrium. *Quarterly Journal of the Royal Meteorological Society*, 133(629):2085–2107.

Palmer, T. N., Buizza, R., Doblas-Reyes, F., Jung, T., Leutbecher, M., Shutts, G. J., Steinheimer, M., and Weisheimer, A. (2009). Stochastic parametrization and model uncertainty.

Peng, J., Zhang, L., and Guan, J. (2015a). Applications of a moist nonhydrostatic formulation of the spectral energy budget to baroclinic waves. part I: The lower-stratospheric energy spectra. *Journal of the Atmospheric Sciences*, 72(5):2090–2108.

Peng, J., Zhang, L., and Guan, J. (2015b). Applications of a moist nonhydrostatic formulation of the spectral energy budget to baroclinic waves. part II: The upper-tropospheric energy spectra. *Journal of the Atmospheric Sciences*, 72(10):3923–3939.

Peng, J., Zhang, L., Luo, Y., and Zhang, Y. (2014). Mesoscale energy spectra of the Mei-Yu front system. part I: Kinetic energy spectra. *Journal of the Atmospheric Sciences*, 71(1):37–55.

Piomelli, U. (2014). Large eddy simulations in 2030 and beyond. *Philosophical Transactions of the Royal Society A: Mathematical, Physical and Engineering Sciences*, 372(2022):20130320.

Piomelli, U., Cabot, W. H., Moin, P., and Lee, S. (1991). Subgrid-scale backscatter in turbulent and transitional flows. *Physics of Fluids A: Fluid Dynamics*, 3(7):1766–1771.

Pope, S. B. (2000). *Turbulent Flows*. Cambridge University Press.

Reed, K. A. and Medeiros, B. (2016). A reduced complexity framework to bridge the gap between agcms and cloud-resolving models. *Geophysical Research Letters*, 43(2):860–866.

Richardson, L. F. (1922). *Weather prediction by numerical process*. University Press.

Robe, F. R. and Emanuel, K. A. (2001). The effect of vertical wind shear on radiative–convective equilibrium states. *Journal of the Atmospheric Sciences*, 58(11):1427–1445.

Rogers, R. and Yau, M. K. (1996). *A Short Course in Cloud Physics*. Elsevier.

Rotunno, R. and Emanuel, K. A. (1987). An air–sea interaction theory for tropical cyclones. part II: Evolutionary study using a nonhydrostatic axisymmetric numerical model. *Journal of the Atmospheric Sciences*, 44(3):542–561.

Satoh, M. and Matsuda, Y. (2009). Statistics on high-cloud areas and their sensitivities to cloud microphysics using single-cloud experiments. *Journal of the Atmospheric Sciences*, 66(9):2659–2677.

Scott, M. (2024). Applied stochastic processes in science and engineering. *Course Notes for Amath 777 Stochastic Processes of University of Waterloo*.

Shutts, G. (2005). A kinetic energy backscatter algorithm for use in ensemble prediction systems. *Quarterly Journal of the Royal Meteorological Society: A journal of the atmospheric sciences, applied meteorology and physical oceanography*, 131(612):3079–3102.

Skamarock, W. C. (2004). Evaluating mesoscale NWP models using kinetic energy spectra. *Monthly Weather Review*, 132(12):3019–3032.

Skamarock, W. C., Klemp, J. B., Dudhia, J., Gill, D. O., Barker, D. M., Wang, W., and Powers, J. G. (2008). A description of the advanced research WRF version 3. NCAR Technical Note-475+ STR.

Skamarock, W. C., Park, S.-H., Klemp, J. B., and Snyder, C. (2014). Atmospheric kinetic energy spectra from global high-resolution nonhydrostatic simulations. *Journal of the Atmospheric Sciences*, 71(11):4369–4381.

Smagorinsky, J. (1963). General circulation experiments with the primitive equations: I. The basic experiment. *Monthly Weather Review*, 91(3):99–164.

Strauss, C., Ricard, D., and Lac, C. (2022). Dynamics of the cloud–environment interface and turbulence effects in an les of a growing cumulus congestus. *Journal of the Atmospheric Sciences*, 79(3):593–619.

Strauss, C., Ricard, D., Lac, C., and Verrelle, A. (2019). Evaluation of turbulence parametrizations in convective clouds and their environment based on a large-eddy simulation. *Quarterly Journal of the Royal Meteorological Society*, 145(724):3195–3217.

Sun, Y. Q., Rotunno, R., and Zhang, F. (2017). Contributions of moist convection and internal gravity waves to building the atmospheric -5/3 kinetic energy spectra. *Journal of the Atmospheric Sciences*, 74(1):185–201.

Tennekes, H. and Lumley, J. L. (1972). *A first course in turbulence*. MIT press.

Thiry, O. and Winckelmans, G. (2016). A mixed multiscale model better accounting for the cross term of the subgrid-scale stress and for backscatter. *Physics of Fluids*, 28(2).

Thompson, G., Field, P. R., Rasmussen, R. M., and Hall, W. D. (2008). Explicit forecasts of winter precipitation using an improved bulk microphysics scheme. Part II: Implementation of a new snow parameterization. *Monthly Weather Review*, 136(12):5095–5115.

Tobin, I., Bony, S., Holloway, C. E., Grandpeix, J.-Y., Seze, G., Coppin, D., Woolnough, S. J., and Roca, R. (2013). Does convective aggregation need to be represented in cumulus parameterizations? *Journal of Advances in Modeling Earth Systems*, 5(4):692–703.

Tobin, I., Bony, S., and Roca, R. (2012). Observational evidence for relationships between the degree of aggregation of deep convection, water vapor, surface fluxes, and radiation. *Journal of Climate*, 25(20):6885–6904.

Tompkins, A. M. and Semie, A. G. (2017). Organization of tropical convection in low vertical wind shears: Role of updraft entrainment. *Journal of Advances in Modeling Earth Systems*, 9(2):1046–1068.

Tulloch, R. and Smith, K. S. (2009). Quasigeostrophic turbulence with explicit surface dynamics: Application to the atmospheric energy spectrum. *Journal of the Atmospheric Sciences*, 66(2):450–467.

Tung, K. K. and Orlando, W. W. (2003). The k^{-3} and $k^{-5/3}$ energy spectrum of atmospheric turbulence: Quasigeostrophic two-level model simulation. *Journal of the Atmospheric Sciences*, 60(6):824–835.

Ukkonen, P. (2022). Exploring pathways to more accurate machine learning emulation of atmospheric radiative transfer. *Journal of Advances in Modeling Earth Systems*, 14(4):e2021MS002875.

Vallis, G. (2006). *Atmospheric and Oceanic Fluid Dynamics: Fundamentals and Large-Scale Circulation*. Cambridge University Press.

VanZandt, T. (1982). A universal spectrum of buoyancy waves in the atmosphere. *Geophysical Research Letters*, 9(5):575–578.

Vela-Martín, A. (2022). Subgrid-scale models of isotropic turbulence need not produce energy backscatter. *Journal of Fluid Mechanics*, 937:A14.

Verrelle, A., Ricard, D., and Lac, C. (2015). Sensitivity of high-resolution idealized simulations of thunderstorms to horizontal resolution and turbulence parametrization. *Quarterly Journal of the Royal Meteorological Society*, 141(687):433–448.

Verrelle, A., Ricard, D., and Lac, C. (2017). Evaluation and improvement of turbulence parameterization inside deep convective clouds at kilometer-scale resolution. *Monthly Weather Review*, 145(10):3947–3967.

Waite, M. L. (2016). Dependence of model energy spectra on vertical resolution. *Monthly Weather Review*, 144(4):1407–1421.

Waite, M. L. and Snyder, C. (2009). The mesoscale kinetic energy spectrum of a baroclinic life cycle. *Journal of the Atmospheric Sciences*, 66(4):883–901.

Waite, M. L. and Snyder, C. (2013). Mesoscale energy spectra of moist baroclinic waves. *Journal of the Atmospheric Sciences*, 70(4):1242–1256.

Wing, A. A. and Cronin, T. W. (2016). Self-aggregation of convection in long channel geometry. *Quarterly Journal of the Royal Meteorological Society*, 142(694):1–15.

Wing, A. A., Emanuel, K., Holloway, C. E., and Muller, C. (2017). Convective self-aggregation in numerical simulations: A review. *Surveys in Geophysics*, 38(6):1173–1197.

Wing, A. A. and Emanuel, K. A. (2014). Physical mechanisms controlling self-aggregation of convection in idealized numerical modeling simulations. *Journal of Advances in Modeling Earth Systems*, 6(1):59–74.

Wing, A. A., Reed, K. A., Satoh, M., Stevens, B., Bony, S., and Ohno, T. (2018). Radiative-convective equilibrium model intercomparison project. *Geoscientific Model Development*, 11:793–813.

Wyngaard, J. (2010). *Turbulence in the Atmosphere*. Cambridge University Press.

Yuval, J. and O'Gorman, P. A. (2020). Stable machine-learning parameterization of subgrid processes for climate modeling at a range of resolutions. *Nature communications*, 11(1):3295.